The Role of Boundaries and Other Microstructural Features on Emergent Mechanical and Mechanically-Coupled Phenomena at the Nanoscale

Thesis by

Rebecca Anne Gallivan

In Partial Fulfillment of the Requirements for the
Degree of
Doctorate of Philosophy

Caltech

CALIFORNIA INSTITUTE OF TECHNOLOGY
Pasadena, California

2023
Defended June 30, 2022

To my family,
particularly my parents and grandparents
whose examples of love, strength, and dedication, have made this journey possible.

ACKNOWLEDGEMENTS

This work would not be possible without the generous support of the Department of Energy and the Amazon AI4Science Fellowship. This work has also been enabled through collaborations with Dr. Zachary H. Aitken, and Dr. Yong-Wei Zhang and the support of Dr. Chi Ma, Dr. Mingjie Xu, and the staff of the Kavli Nanoscience Institute at Caltech. Additionally, I would also like to extend special thanks to my committee members: Professor Katherine T Faber, Professor Brent Fultz, and Professor Joseph Falson.

My doctoral work is founded in the support and encouragement of my advisor, Professor Julia R. Greer. Julia, you have shown me the wonderful world of nanomechanics and allowed me to fully cultivate a profound appreciation for the importance of length scale. I deeply appreciate the freedom, enthusiasm, and support you have given to my many teaching endeavors. Thank you for helping me grow as a scientist and academic. Your belief in me has helped to make me the best researcher I can be.

I want to acknowledge the important mentorship of Dr. Haolu (Jane) Zhang, Dr. Daryl Yee, Dr. Ryan Ng, Dr. Claire Saunders, and Dr. Benjamin Herren in shaping me as a researcher. It is both through your example and advice that I have built confidence in my path forward.

I would like to give special recognition to my fellow colleagues in the Greer Group, particularly those in my cohort — Dr. Max Saccone, and the soon-to-be Drs. Amylynn Chan, Widianto Moestopo, and Fernando Villafuerte. Your wonderful discussions in and outside the lab are a cornerstone of my time at Caltech.

An good scientist is not formed in the isolation of the academic world but from the community which surrounds them. For the friendship of so many both within and outside the scientific space, you encourage me to continue pursuing the interesting questions and dig down into the deep parts of the unknown. To my many high school students and my wonderful undergraduate researchers, thank you for helping me grow as a mentor and teacher. Your interest in materials has allowed for the exploration of fun topics and given me unique insights.

Finally I would like to acknowledge my family to whom my thesis is dedicated. To my grandparents, your examples of strength, humor, faith, and love have shown me how to meet every challenge head on. To my aunts, uncles, cousins, and extended family, your enthusiasm and excitement centers me on the joy of my work. To my tortoises who have been my constant companions for twenty-three years, you are my little rocks and the best listeners. To my siblings, you are my unfailing friends. I learn so much for you both and will

always look to you as examples of perseverance, joy, and fun facts. To my partner, Bijan, you have made this journey through graduate school a more wonderful experience than I could have ever anticipated. To my parents, whose unfailing support has always been my foundation, you remain the greatest teachers I have ever known. Thank you for cultivating my curiosity and nurturing my passions.

ABSTRACT

As nanotechnology continues to advance, the need for smaller, structurally complex materials has grown. However, these microscopic (10^6) and nanoscopic (10^9) structures often display unexpected changes in mechanical properties as compared to their macroscopic counterparts. Nanomechanical studies investigating size-effects in stiffness, strength, recoverability, ductility, and fracture, reveal an intimate interplay between the breakdown in continuum behavior and the energetic landscape of microstructural mechanisms. Additive manufacturing opens new opportunities to explore this microstructure-mechanics relationship as it enables the micro- and nano-scale production of novel materials and microstructures. While existing studies on structural and functional materials highlight the unique size-scale behavior, a large gap remains in our understanding of the complex relationship between microstructure and material performance. This work investigates the interactions and mechanisms that give rise to emergent nanoscale phenomena. With microstructural characterizations, we demonstrate the role of boundaries and interfaces on mechanical and mechanically-coupled behavior in (1) dense nanowire arrays, (2) nano-architected nanocrystalline zinc oxide, and (3) highly-twinned additively manufactured metallic systems. This work provides critical insights into the mechanisms underlying the observed emergent phenomena and further opens our fundamental intuition for microstructure-mechanics relationships in materials at the nanoscale.

PUBLISHED CONTENT AND CONTRIBUTIONS

[1] Rebecca A. Gallivan and Julia R. Greer. Failure mechanisms in vertically aligned dense nanowire arrays. *Nano Letters*, 21(18):7542–7547, 2021. URL `https://doi.org/10.1021/acs.nanolett.1c01944`.

Contributions: R.A.G participated in the conception of the experiments and model. R.A.G. synthesized samples, performed experiments, analyzed data, formulated application of the model, and lead writing the manuscript. *Chapter 2 has been adapted from this work.*

[2] Rebecca A. Gallivan, Zachary H. Aitken, Antoine Chamoun-Farah, Yong-Wei Zhang, and Julia R. Greer. Emergent mechanical and electromechanical behaviors in additively manufacture nanocrystalline zinc oxide. *Manuscript in preparation*

Contributions: R.A.G. participated in the conception of the experiments. R.A.G. synthesized samples, performed experiments, analyzed data, and formulated analytic the model and its application. R.A.G. was a primary author for the manuscript. *Chapters 3 and 4 have been adapted from this work.*

[3] Min-Woo Kim, Max L. Lifson, Rebecca A. Gallivan, Julia R. Greer, and Bong-Joong Kim. Recoverable electrical breakdown strength and dielectric constant in ultralow-k nanolattice capacitors. *Nano Letters*, 19(8):5689–5696, 2019. URL `https://doi.org/10.1021/acs.nanolett.9b02282`.

Contributions: R.A.G contributed to the FEA simulations and interpretation of the breakdown behavior in these materials. R.A.G. also participated in writing of the manuscript. *This work has not been adapted for this thesis.*

[4] Max Saccone, Rebecca A. Gallivan, Kai Narita, Daryl W. Yee, and Julia R. Greer. Microscale fabrication of 3d multicomponent metals via hydrogel infusion. 2022. URL `https://doi.org/10.21203/rs.3.rs-1108933/v1`. *Manuscript submitted for publication.*

Contributions: R.A.G. performed the nanoindentation, EBSD experiments, analyzed data, discussed the findings, and edited the manuscript. *Chapters 5 and 6 include adaptation of this work and build further upon its findings.*

TABLE OF CONTENTS

LIST OF ILLUSTRATIONS

LIST OF TABLES

Chapter 1

INTRODUCTION

One of the foundational perspectives in the study of materials is that atomic-level processes have profound effects on the macroscopic (or observable) behavior. From explaining fundamental relationships to identifying key engineering considerations, the nano-scale world provides unique insight into the mechanisms which influence and occasionally dominate material performance. With careful thought, we can leverage these tiny tools to answer the questions and puzzles uncovered during the exploration of materials (new and old) and their phenomena.

A vast body of work has laid the framework for this atomistic perspective and provides both mechanistic and energetic models which elucidate how microstructure begets performance[1]. However, the picture is far from complete. This thesis aims to contribute its own piece to the puzzle within the field of nanomechanics, a discipline where size matters because of its marked impact on material behavior. The following work characterizes the relationship between boundaries[2], length-scale, and mechanical or mechanically coupled behaviors in materials. It examines the importance of the interface in structures made through traditional nanofabrication techniques and leverages advancements in additive manufacturing at micro- and nano-length scales to explore new but not yet fully understood functional materials including zinc oxide (ZnO), copper (Cu), nickel (Ni) and cupronickel alloys. Through this fundamental investigation of microstructure and length-scale, we seek to provide insight into the mechanistic understanding of emergent nanomechanical phenomena and lay the foundation for future design and engineering of these materials on the nanoscale.

The remainder of the introduction will provide specific context and background for the techniques, theory, and concepts relevant for contextualizing the research contained within the body of this work.

---

[1] Performance here is defined as the observed or anticipated behavior of a material in its post-processed form or as a component. Properties will refer to the fundamental, theoretical, and/or thermodynamic response of only the material. Performance can have a stochastic element stemming from variation within or between produced materials. Properties are typically universal for a specific material.

[2] We will generally consider various types of boundaries with a focus on free surfaces, twin boundaries, and grain boundaries including coincident site lattice (CSL) boundaries.

1.1 Micro- and Nano-Scale Fabrication — Traditional 2D Techniques

Lithography

Lithography is a technique by which a specific pattern is printed or written into material. For small-scale fabrication, this is typically achieved by changing the solubility of a photoresin or photoresist through photolithography (sometimes referred to as optical lithography). It can be done with a specific wavelength of light[3], or an electron beam (known as e-beam lithography). Depending on the formulation of the resist it will either increase solubility (positive-tone) or decrease solubility (negative-tone) with respect to the developer solution when exposed. After exposure and development the remaining photoresist will be either a copy of the mask (positive-tone) or an inverse image (negative-tone).

Photolithography uses physical masks to block out light in specific patterns. The technique is fast and effective for large areas, and resolution is limited by the wavelength of the light source. State-of-the-art instrumentation can produce features down to 40 nm using-ultra deep UV sources [**?**]. Conversely, e-beam lithography rasters an electron beam in the desired pattern to expose the photoresist. This allows resolutions below 10 nm but can be quite time intensive and require significant optimization of write parameters [90]. For this reason, the technique is best suited for patterning requiring high-resolution or precise feature alignment.

Lithography is primarily coupled with etching and deposition processes whereby the resist now acts as the mask to expose (or shield) areas of the substrate. These techniques are a critical tool for controlling material placement and removal in nanofabrication and are widely used in creating new nanotechnologies [42, 43, 132].

Deposition

Deposition can be carried out through a variety of methods depending on the desired thickness, material, and level of conformity to the substrate. Though not exhaustive, we will outline the more commonly used techniques and those most relevant to the experiments and literature discussed in this thesis.

Atomic Layer Deposition (ALD) conformally coats the surface of a structure by depositing one atomic layer at a time. Of the deposition techniques discussed in this section, it has the highest resolution for film thickness and can form extremely smooth surfaces [116]. Though more limited that other methods in the range of available materials, ALD has been widely

---

[3] This is often a blue or lower-energy UV light, though some chemistries require green or deep UV sources.

adopted in nanofabrication designs and even used to make hollow nanolattice structures [141, 175, 221].

E-beam physical vapor deposition is a technique which uses a high-energy electron beam to vaporize materials which are precipitated from the gaseous phase onto a substrate. The technique is a line-of-site deposition, meaning it can only coat surfaces perpendicular to the throwing direction and cannot coat shadowed areas. E-beam deposition can produce films of a wide array of metals and oxides with thicknesses between several nanometers and microns [78]. Used in a variety of applications for chip-based devices and coatings [22, 78, 107, 182], the technique provides a robust and relatively fast method for coating structures.

Electrodeposition is a method of electrolysis which deposits material from a solution onto a conductive substrate. Through control of the temperature, pH, current density, and electrical potential, various nanostructured surface morphologies can be formed [166, 203, 223]. In conjunction with masking techniques, electrodeposition has also been used to form nanopillars and more complex structures [97, 201].

Etching

As a chemical process, etching provides an effective method for large-scale, parallelized removal of material that typically leaves an atomically smooth surface with minimal residue or microstructural transformation. Wet-etchants refer to solution-based reactions that strips the material from the solid interface into the solution. Depending on the material and solution interactions, an etch can be isotropic (i.e., equal rate of removal from all directions) or anisotropic (i.e preferential removal of atoms from a particular crystallographic plane) [77].

Conversely, dry etching utilizes plasmas to strip material from an exposed surface. These techniques, known as Reactive Ion Etching (RIE), are far more directional than wet etching and eliminate the need for handling dangerous chemical solutions [88, 120, 185]. RIE also allows for greater control and precision during the etching process. However, the process recipes often require far more optimization as specific chamber conditions can greatly impact the surface interactions.

Focused Ion Beam Milling

Another powerful method for nanoscale removal of material is through a technique known as focused ion beam (FIB) milling. Using principles similar to that of scanning electron microscopy, a beam of ions is focused and rastered in a particular pattern to mill away the desired material. FIB systems are used in a variety of ways including to expose cross-sections and areas of material [56], prepare specimens for TEM analysis [63, 95, 138], fabricate samples for nanomechanical testing [16, 189], and depositing metals such as platinum and tungsten [162].

There are several ion sources readily used in FIB milling with gallium as the most common. However, gallium is problematic during the preparation of certain materials as it can alloy with the substrate and subsequently influence local microstructure [138, 228]. Other sources such as xenon, argon, neon, and helium reduce interactions between the beam and material making them more attractive for damage-sensitive samples [8, 23, 112]. Additionally cryo-FIB can reduce damage to samples by cooling down the system. This technique is most commonly employed with biological and light element samples [140, 216].

FIB-milling is a technique heavily used in the field of nanomechanics and microstructural characterization and is instrumental to the work presented in this thesis (and other doctoral work not outlined here). This method for material removal also underpins much of the foundational work on mechanical size effects and is a critical tool in probing the microstructure-mechanics relationship of specific microstructural features. Further discussion of these fields can be found in Section 1.4 and 1.5.

1.2 Micro- and Nano-Scale Additive Manufacturing

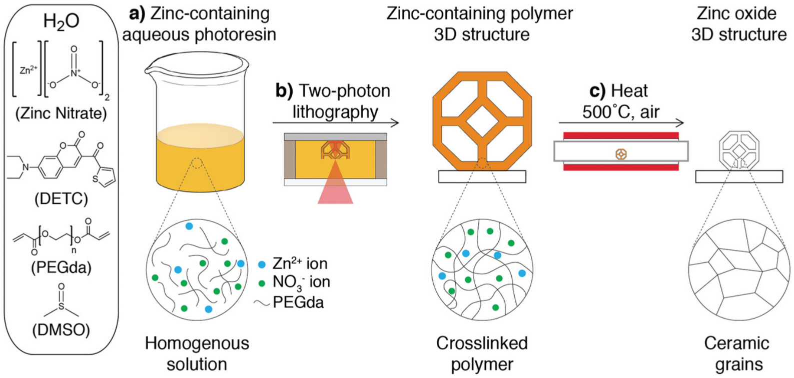

Figure 1.1: **Schematic of Photopolymer Complex Synthesis Method for Zinc Oxide.** Using a resin containing zinc ions, the structure is printed (b) with two-photon lithography to form a solid zinc-ion containing polymer. Subsequently (c) the structure is heated in air to remove the organic material and leave behind a zinc oxide 3D structures. (Image reproduced with permission from Ref. [209].)

At the macroscale, additive manufacturing (AM) shows great promise as a new materials-processing technique. In additional to enabling otherwise unmachineable parts, materials printed through AM can produce unusual microstructures such as extremely high dislocation densities, columnar or dendritic grain shapes, and gradients of cyrstallographic phase [68]. As is further discussed in Section 1.3, microstructural features govern mechanical behavior; thus AM processing may hold promising new avenues for engineering mechanical properties and material function. These novel microstructures also open opportunities for advancing fundamental investigation of atomic-level processes and further fill in our energetic understanding of deformation mechanisms.

For the micro- and nano-scale, additive manufacturing has great potential to advance small-scale devices. Additive processing methods provide an extraordinary opportunity for nano-architecting materials; however, at (and below) the microscale, material selection is limited [82]. This is due, in part, to the challenge of controlling materials and chemistries at the nanoscale with high spatial confinement. However, many techniques have been developed to open up this materials space. These techniques are typically based in interactions facilitated by an energetic beam (laser, electron, or ion beam) [31, 110, 159, 180, 184, 190, 217], surface tension [62, 87, 152], or extrusion [7, 81, 177]. Appendix A provides more information on many of the reported small-scale AM techniques.

The additive manufacturing used in this work is a novel method for printing metals and oxides known as Hydrogel Infusion (HI). This technique is a based in photolithography but applies a series of treatments to the printed hydrogel component in order to produce the desired material. We utilize two variants of the HI technique: the photopolymer complex synthesis or PCS approach (Figure 1.1) where metal ions are contained with the resin [209, 210] and the swell-in approach (Figure 1.2) where metal salts infuse the hydrogel after printing [170, 211]. Then, the metal ions contained in the hydrogel are converted to an oxide during calcining. If desired (and thermodynamically possible) the oxide can be reduced to its parent metal or metallic alloy. One benefit of this technique is the range of materials produced and high-resolution of the final components.

Chapters 3 and 4 characterize the microstructure and mechanically related behaviors of ZnO printed through PCS using two-photon lithography[4]. The materials are between 200 nm and 5 μm in feature size. Chapters 5 and 6 characterize the microstructure and mechanical properties which arise from Cu, Ni, and cupronickel alloys printed through the swell-in

---

[4] Two-photon lithography uses special photoinitators that require a two photon event to induce polymerization. This allows for very small voxels (or volume pixels) when printing as only the focal point of the laser is likely to be energetic enough to generate a two-photon event.

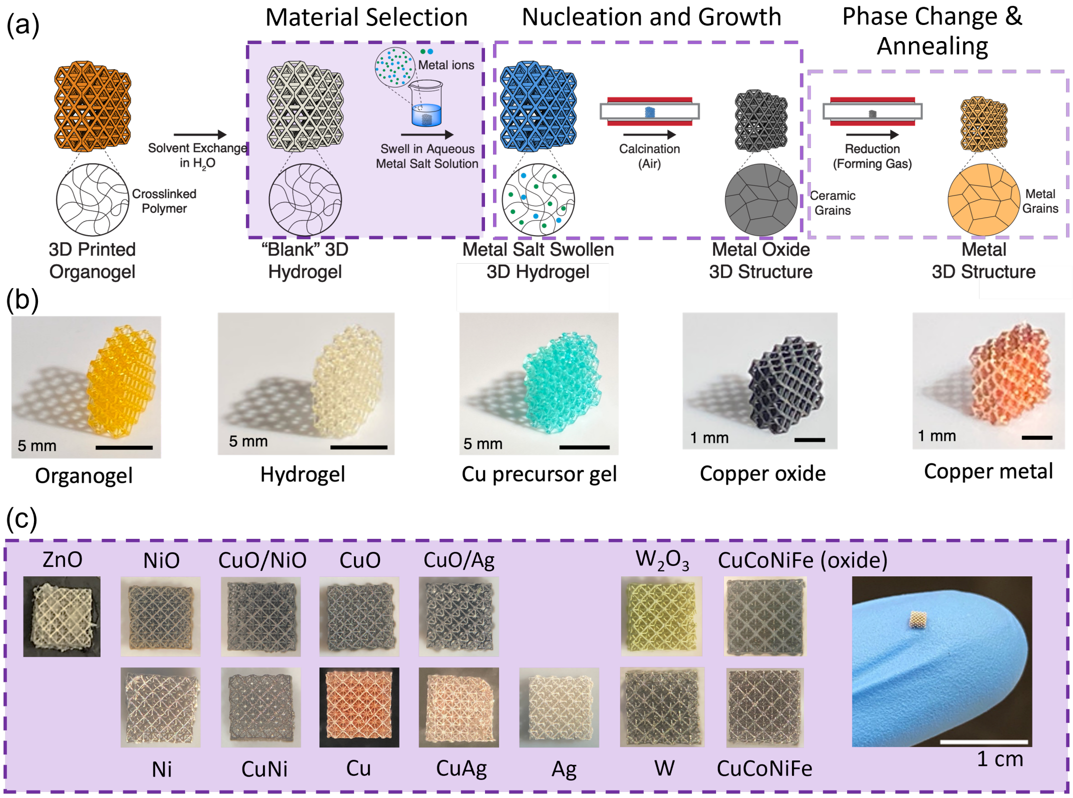

Figure 1.2: **The Swell-in Hydrogel Infusion Process for Additive Manufacturing.** (a) Schematic representation of the methods for turning a polymeric based gel into an oxide and subsequent metal. It highlights the steps associated with first material selection (swell-in), then nucleation and growth of the material (calcining), and finally potential phase changes in addition to high degrees of diffusion (annealing). (b) Physical samples for Cu at the corresponding stages schematically outlined in (a). (c) A demonstration of the wide material selection derived from swelling in various metal salt precursors. All lattices are approximately 2 mm x 2 mm x 1 mm

approach with a traditional photolithography 3D printing technique. These metals are microscale in feature size.

1.3 Select Microstructural Features and Their Role in Mechanical Behavior

Dislocations

Dislocations are a one-dimensional defect within a crystal structure that can be thought of as an extra half-plane of atoms (Figure 1.3). While the schematic representations presented in this section depict dislocations as simple structures, it is important to remember that dislocations form complex structures and superstructures that move between different planes and throughout the three-dimensional space of the crystal. They are a primary mechanism for plasticity (particularly in metals) and the study of these defects constitutes an entire

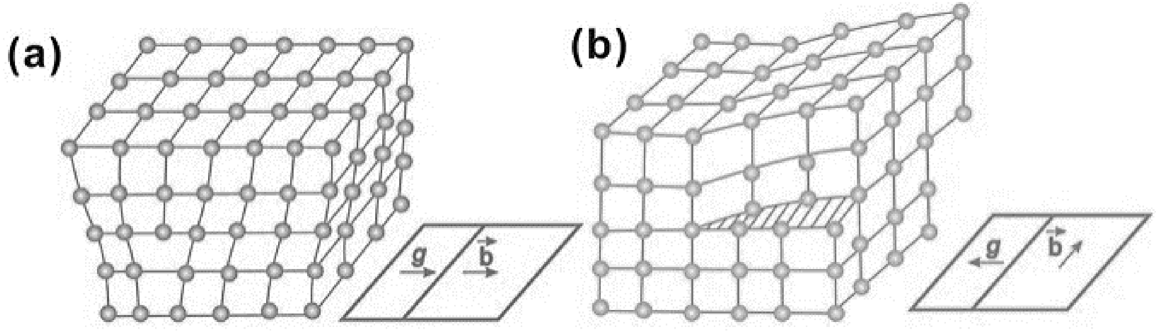

Figure 1.3: **Dislocations in a Crystal.** Schematic representation of (a) edge and (b) screw character dislocations. Both dislocation types have small schematics indicating the relative orientation of the Burger's vector as compared to the dislocation line and the resulting glide as a function of applied stress. The image was taken as an excerpt from Fig. 1 in Ref. [118] and color adjusted. This material is made available under a public Creative Commons License.

subfield of material research[5]. Several foundational books exist on dislocations, their structure, and their relationship to macroscopic behavior [29, 83, 89]. Moving forward, we will assume reader familiarity with dislocations as a concept.

When it comes to plasticity, dislocations are one of the most dominant mechanisms. They are often first introduced as defects which are "statically" stored in the lattice and irreversibly help dissipating applied stresses. They participate in this dissipation through formation and motion through the lattice. These "static" dislocations are typically created from sources (Frank-Reed, dislocation loops, grain boundaries, free surfaces etc.) and once formed can undergo a different processes such as glide, climb, cross-slip, annihilation, etc. As dislocations become locked or pinned due to interactions with other dislocations, defects, or microstructural features, the material undergoes hardening where more stress is needed to continue deforming the material. The forces and interactions necessary for dislocation motion are generally described with consideration for the Peierls barrier strength (i.e., lattice friction) [157] for onset of yield and by the Peach-Kohler equation [156] for post-yield slip. However, there is significantly more dislocation anatomy, physics, and complexity necessary to fully capture and describe the atomic-level processes which enable plastic behavior[6]. This is particularly true when dissecting the material-specific relationships or looking at crystals that are ionic, alloyed, or non-cubic[7]. As the work discussed in this thesis does not

---

[5] Foundations of the field were set in 1934 by Orowan [153], Taylor [186], and Polanyi [160]. Refinement and expansion has added considerations for complex materials like high-entropy alloys [57, 131, 133, 139].

[6] One can read a lovely poem by Dr. Sharvan Kumar that incorporates much of pioneering work on dislocations published in Appendix B [108].

[7] Even simply looking at non-FCC structures adds greater complexity.

directly address the specific energetics and calculations around dislocation interactions, this section will focus on the intuition, key characteristics, and phenomenological understanding necessary for interpreting plasticity behavior.

Traditionally processed materials typically have dislocation densities of ~10^8 for metals and ~10^3 for ceramic materials, but this number is highly dependant on processing and deformation. For example, it can jump to >10^{12} for metals which have been highly deformed during processing [149]. One major contributor is geometrically necessary dislocations (GNDs). These dislocations are physically indistinguishable from "static" dislocations but play an important collect role to accommodate curvature of the lattice or localized non-uniform plastic deformation (Figure 1.4 provides some schematic examples). They are responsible for residual strains within the crystal and enable semi-coherent interfaces. GNDs can also be injected into a material during deformations like indentation [64]. For additively manufactured metals, GNDs are often present in high quantities as kinetic effects, due to rapid heating and cooling, leave strains within the material [106, 126].

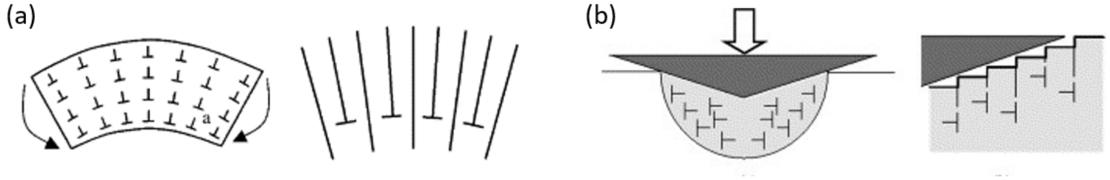

Figure 1.4: **Schematic Representation of Geometrically Necessary Dislocations.** (a) Graphic representation of how a bend in the material can necessitate GNDs and (b) highlights how GNDs can accommodate the deformation formed during nanoindentation. Image adapted from Ref. [64]

Work in the field of material growth and manufacturing has enabled processing of extremely high-quality films and bulk crystals which minimize the presence of both GND and static dislocation structures [9, 196]. This low dislocation density is also seen in many nanoscale materials where energetic competitions with surfaces reduce the likelihood of dislocation presence within the volume. Mechanically, low dislocation density has been suggested as a possible reason for the observed strengthening in some nanomaterials [2].

Grains and Grain Boundaries

Grains are crystallites which collectively make up a material, and grain boundaries are the interfaces between crystallites of different orientations. The size, shape, boundary type, and other morphological features of a grain are closely linked with a material's processing, properties, and performance. Due to this central relationship to so many aspects of a

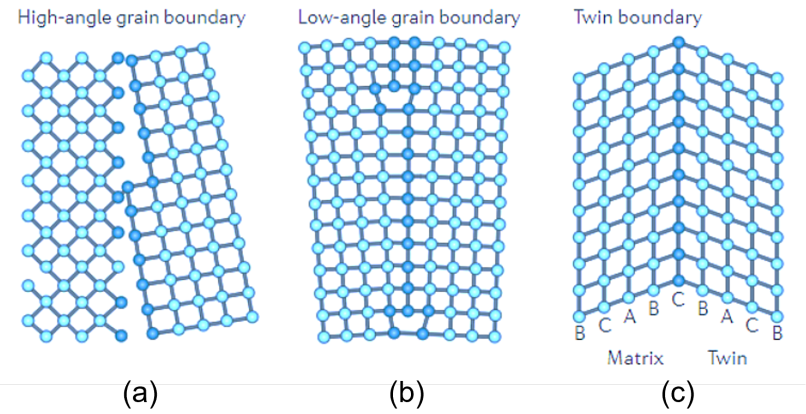

Figure 1.5: **Schematic of Grain Boundaries.** (a) High-angle, (b) low-angle, and (c) twin boundaries highlight boundaries with varying level of misfit between the two grains. Adapted from Ref. [128]

material, grain structure is one of the key metrics and features used to classify and dissect the processing-microstructure and microstructure-property relationships.

Grain boundaries can broadly be categorized into three main classes: low-angle, high-angle, and coincident site lattice (CSL). Low-angle boundaries (Figure 1.5b) refer to the boundary between two grains with a misorietnation angle which is generally less than 10°. These boundaries are formed primarily through dislocations which accommodate the relatively small misorientation of the two lattices. High-angle boundaries (Figure 1.5a) refer to boundaries between two grains with large degrees of misorientation between the lattices. As seen in the schematic representation (Figure 1.5), high-angle grain boundaries generally have a distinct discontinuity at the interface. High-angle boundaries can contain additional free volume, amorphous structuring, and substantial width [26, 30, 181]. These types of high-angle boundaries are known to be strong barriers to dislocation motion, stress concentration points, special diffusion pathways, and areas of segregation in alloys [59, 91, 105, 115, 178]. However, due to the periodic nature of crystals, at various angles of misorientation there are boundaries which exhibit relatively low degrees of misfit between the grains. These special boundaries are known as CSL boundaries (Figure 1.6).

CSL boundaries are grain boundaries which form a mirrored repeating structure along the length of the boundary. The name comes from the coincidence of the two lattices when overlayed at the misorientation angle of the boundary. CSL boundaries are typically labeled a Σ that is followed by a number which is the reciprocal ratio of coincident atomic sites to the atomic sites of any of the parent lattice. As these boundaries form with a low degree of misfit between the grains, CSL boundaries are typically lower energy grain boundaries regardless of misorientation angle. A great deal of simulation, theory, and some *in-situ* experimental work has looked at the unique role of these low-energy boundaries on mechanical properties [104, 173, 218]. While the specific energetic landscape for these CSL boundaries is different for each material, there is a consistent global trend that CSL boundaries have greater toughening effects and mobility than other types of grain boundaries. CSL boundary networks have also been shown to reduce corrosion [86].

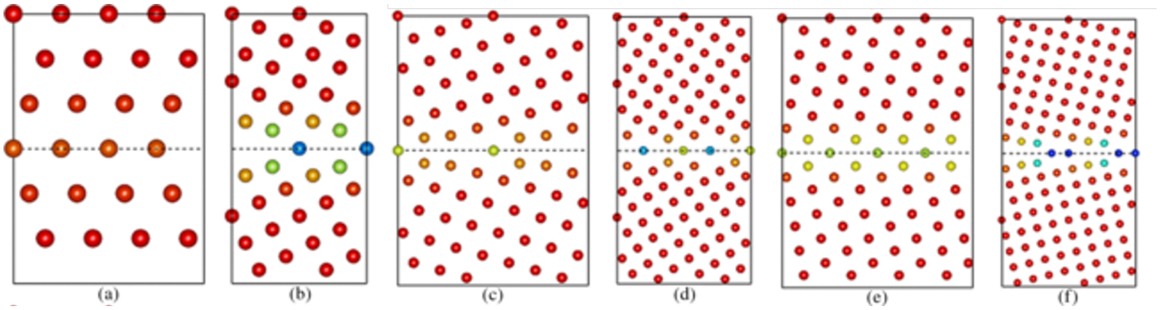

Figure 1.6: **Schematic of Various CSL Boundaries.** Coloration helps guide the eye to the patterns in the boundaries for (a) $\Sigma3$, (b) $\Sigma5$, (c) $\Sigma9$, (d) $\Sigma13a$, (e) $\Sigma11$, and (f) $\Sigma17a$ CSL boundaries. Adapted from Ref. [34]

Twin boundaries (shown in Figure 1.5c) are a form of type of CSL boundary known as $\Sigma3$ boundaries. They are generally considered their own special class of microstructural feature due to their unique lack of atomic misfit along the boundary and special relationship to stacking fault energy (SFE). Twin boundaries also exhibit a special type of plastic response stemming from an atomic-level processes known as twinning and detwinning mechanisms. This type of boundary formation and motion is distinct from many of the other CSL and grain boundary plasticity mechanisms. Grain boundaries typically move either through elevated temperatures enabling diffusive processes or through mechanisms of grain boundary slip, slide, and rotation when grain size is extremely small (<30 nm) [2, 32]. Though certain boundaries like $\Sigma7$ are well studied in simulations, and *in-situ* TEM experiments have demonstrated these mechanisms for grain plasticity, many open questions remain with regards to grain boundary deformation and stress-relaxation.

All these boundaries impede dislocation motion as shifts in the crystal orientation disallow the continuation of glide without added stress. However, the dislocation character (i.e., edge and screw) and the angle at which they approach the barrier can lead to different interactions or strength of the resistance to motion. In twin boundaries, screw dislocations do not experience very much resistance as cross-slip allows an easy transition to the twinned region.

1.4 Nanomechanical Characterization and Analysis Techniques

Nano-indentation

Indentation as a measurement of a material's resistance to plastic deformation was first demonstrated as a macro-scale technique by Brinell in 1900. The method was further developed and refined over the next 50+ years particularly with the introduction of new tip geometries, including the famous pyramidal-shaped tip by Vickers in 1925. Measurements were also pushed towards smaller indentation volumes and give rise to micro-indentation, which allows testing of smaller features and enables more localized studies of mechanical properties. In the 1970s, innovations in manufacturing of smaller tip sizes, high-sensitivity load sensors, and ultra-fine displacement controllers, allowed for the manufacturing of nano-indentation instruments pushing mechanical characterization to a new microscopic level [27, 187]. Figure 1.7 shows a schematic for a standard nanoindentor like the instrumentation used in this thesis. The technique has continued to evolve over the past 50 years with advancements in measurement methods, such as the Oliver and Pharr method for calculating elastic properties [150], thin film indentation [19, 171], high-temperature testing [198], etc. Nano-indentation has also opened new studies into size-based effects and hardening mechanisms at the micro- and nano-scale. As we investigate more materials manufactured with micro-scale features, nano-indentation becomes a crucial characterization tool for mechanical properties and performance. The following sections will outline key concepts, features, and analyses associated with the nano-indentation technique.

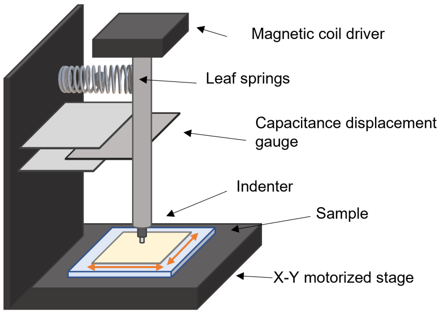

Figure 1.7: **Schematic of *ex-situ* Nanoindentor.** The instrument parts (grey) are labeled and the stage motion is indicated by orange arrows. The sample is cream colored. Image courtesy of Seola Lee.

Calculating Hardness and Elastic Modulus

Hardness can be calculated through the following relationship:

$$H = \frac{P_i}{A_i} \tag{1.1}$$

with H as the hardness, A_i as the area of contact between the tip and the material at a specific load, P_i. Traditionally this is calculated as the prescribed peak load over the contact area of the indent mark[8]. However, modern nano-indentors provide load and displacement values (which can be converted into the contact area) throughout the test enabling near-continuous hardness measurements with depth. Since the tip is of a known geometry, the contact area, A_i, is simply a function of the depth. This relationship between A_i and displacement, h, is determined through the calibration of that specific tip on a known standard (typically fused silica). It is important to note that no tip is perfectly sharp. Thus for each tip, there is a threshold depth before which we may not fully trust the measured hardness values. This threshold can be determined during the area function calibration step.

The elastic modulus can be measured using the method proposed by Oliver and Pharr in 1992 [150] which calculates the effective modulus, E_r, as a function of the measured stiffness, S, and the contact area, A.

$$E_r = \frac{\sqrt{\pi} S}{2\sqrt{A}} \tag{1.2}$$

This formulation holds any indentor tip geometry which is as a body of revolution described by a smooth function. The effective modulus accounts for the effects of non-rigidity in the indentor and can be defined as:

$$\frac{1}{E_r} = \frac{1-\nu^2}{E} + \frac{1-\nu_{tip}^2}{E_{tip}} \tag{1.3}$$

where E and ν are the elastic modulus and Poisson's ratio for the specimen while E_{tip} and ν_{tip} are the elastic modulus and Poisson's ratio for the indentor tip. For materials which are significantly less stiff than the tip, the reduced modulus can be taken as effectively equivalent to the material stiffness.

To calculate the elastic modulus of the material itself we combine Eq. 1.2 and 1.3 to form:

$$\frac{1}{E} = \frac{1}{1-\nu^2}\left(\frac{2\sqrt{A}}{\sqrt{\pi} S} - \frac{1-\nu_{tip}^2}{E_{tip}}\right) \tag{1.4}$$

The stiffness term can either come from the unloading slope at the maximum depth of the indent or a stiffness measurement collected from the instrument. Some modern nanoindentors are able to provide a continuous stiffness measurements (CSM) by applying a small (~1-3 nm) oscillating displacement to the tip.

Additional Technique Considerations

While nano-indentation provides many important benefits, it is important to consider some of the limitations and caveats of the technique.

---

[8] Some indention tests report the hardness through their own unit-less test-specific hardness scale. These scales can be converted to SI units for comparison.

1. Samples need to be prepared so that the surface is smooth as local variation in the testing surface can impact the actual contact hardness and thus change hardness and elastic modulus measurements.

2. In order to ensure that tests are truly probing the material of interest, geometric constraints need to be considered; (1) The distance from the indent to an interface should be ~10x the size of the indent in order to ensure no boundary effects; (2) Indents should be spaced ~3x the width of the indentation as this is generally the size of the plastic zone formed under the indentation. Many experimental studies and simulations highlight the impact of boundaries on measured hardness for nano-indentation [96, 99, 146]. Therefore one must carefully design experiments to eliminate boundary interactions or thoughtfully evaluate the role of interfaces in the study.

3. Thermal drift can contribute significantly to measured values due to the small displacement typical of nano-indentation. Instruments have incorporated physical features to reduce thermal drift and software-based calculations which can identify, help stabilize, and correct for drift in displacement measurements. However, this is still a serious consideration when preforming very sensitive or shallow indentations.

4. Nano-indentation is inherently statistical in its sampling of the material as microstructural features such as grain boundaries, pores, secondary phases, interfaces, etc. are often larger than the indentation. As these features can impact the local hardness of a material, the variation in measured hardness for nano-indentation is typically larger than micro-indentation techniques. This feature necessitates statistically significant sample sizes when describing the material (as opposed to investigating a specific feature).

While additional limitations exist for this technique, the four listed above and the others outlined throughout this section, highlight the primary considerations taken into account for the nano-indentation testing performed in Chapter 6 of this thesis.

Micro- and Nano-mechanical Tests: Compression and Tension

Mechanical tensile and compression tests are key characterization techniques for a variety of mechanical properties including, elastic modulus, yield stress, failure stress, fatigue, and toughness. Tensile tests pull on a specimen at either a constant loading or displacement rate. The load and displacement of the sample is measured throughout the test to understand the materials response to the mechanical stimuli. Compression tests similarly measure the load and displacement response of a material but under uniform compressive forces. Compression tests typically take cylindrical samples.

In 2005, Uchick and Dimiduck applied this macroscopic concept to micro-sized pillars created by FIB milling[9] [189]. Using a nano-indentor with a flatpunch tip whose radius is larger than the FIB-ed pillar, a compressive stresses is applied to the micropillar in the same way as a macroscale compression test. This compression methodology holds for any material with a smooth top surface and is smaller than the indentation tip, opening the doors for clean and simple analysis of mechanical properties for micron- and nanometer-sized samples.

Leveraging some of the other features already existing in the nanoindentor, micro- and nano-compression grew to include methods for evaluating stiffness in the pillars [69], cyclic/fatigue/failure testing [119, 154, 231], dynamic mechanical analysis (DMA) [52, 142], and even investigate complex structures such as nano-architected lattices [101, 141].

All nanomechanical testing outlined thus far can all be preformed *ex-situ*, meaning the physical material response to stimuli is not observed during the experiment. Conversely, *in-situ* nanomechanical testing allows imaging of the specimen before, during, and after testing. This is typically done by placing a nanomechanical testing apparatus within an SEM chamber. Thus, the specific features and mechanical signatures observed in the load-displacement data can be correlated to events and physical phenomena displayed by the material. *In-situ* testing also allows for better alignment and control, which is particularly important for nano-scale structures, and videos of testing can be used to correct for drift in displacement readings.

Micro- and nano-scale tensile experiments are made possible through *in-situ* testing. Typically they are performed with either a push-to-pull system (Figure 1.8a) or through specific "grip" tips that can be used with a nanoindenter (Figure 1.8b). Both methods require precise alignment of the sample for each specimen which is not feasible in commercially available *ex-situ* indentors. While tensile tests allow for very clear measurement of failure and plastic behavior in materials, sample preparation for micro and nano tensile experiments are significantly more labor-intensive than pillar fabrication and are not always feasible. Chapters 2, 3, and 4 provide more specific discussions about the choice to use nanocompression experiments rather than tensile experiments when studying nanowire bundles and nano-architected ZnO respectively. Appendix C provides more insights to the considerations, data treatment, and analysis of microcompression test.

---

[9] The FIB technique is discussed earlier in Section 1.1.

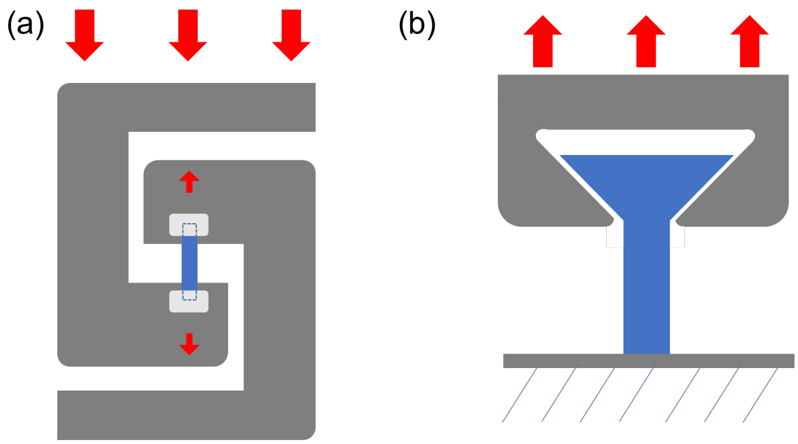

Figure 1.8: **Schematic Microtensile Testing.** The red arrows indicate the direction of the applied force. (a) The push-to-pull configuration relies on compressive stress to move the entire c-shaped part, thus pulling on the specimen (blue) that has been welded by some deposited material (light grey). (b) The grip configuration emulates a macroscale tensile test with the sample (blue) well connected to the substrate.

Nanoscale Fracture Experiments

Another area of active investigation is the fracture properties of materials at the nanoscale. Various experimental methods have been developed to probe fracture toughness and investigate failure behavior in materials at the smallest lengthscales. Notably, macro- and micro-indentation has been used as a method for forming and driving cracks as a way to calculate failure properties and probe interfacial toughness [45, 191]. Some work has looked to using nanoindentation in a similar way to investigate highly localized or small features [80].

Small-scale tensile experiments have also provided a platform for studying the size-effects of notches or flaws with comparable length-scale to the microstructure. These types of tensile nanomechanical experiments can also be performed to generate more traditional crack-opening geometries [71, 137]. Such experiments are of particular interest for nano-architected or nanolattice-like structures where there may be interplay between discrete lattice elements, the constituent material, and the "continuous" global behavior of the structure.

Alternatively, work by Tertuliano demonstrates vailidity of a nano-scale 3-point bend tests [188]. While this method can also interface with printed structures, some of its great strength lies in being able to probe specific features or hierarchical materials that have been lifted-out (i.e., removed as a small specimen). Unfortunately none of these experimental methods are compatible with the nanowire bundle specimens investigated in Chapater 2 or the specific nano-scale printing technique explored in Chapters 3 and 4. Instead, this work focuses on characterizing the performance and behavior of these materials at failure (both local and catastrophic). It builds mechanistic and phenomenological relationships that can provide predictive analysis important for future application and design.

Atomistic Simulations

Another set of tools for investigating atomistic mechanisms and fundamental crystal properties are simulations. These atomic-focused techniques use fundamental continuum physics or first-principles methods to calculated material behavior. Below we outline a handful of common simulations which focus on different types of calculations and size regimes within the microstructure of the material. All of these methods are limited by computational expense; but, when paired with experimental work can provide a deeper insight and more rounded explanation of the observed phenomena.

Density Functional Theory (DFT) calculations use quantum mechanical principles to model the elastic, electronic, structural, and dielectric properties of a many-body atom array [176]. By solving for bond interactions to estimate, with reasonable accuracy, these fundamental properties of crystals, DFT can provide a theoretical basis for elastic stiffness tensor values [67, 205], surface energies [127, 226], stable crystal phases or structures [24, 39], and other fundamental attributes [76].

Monte-Carlo simulations are effective in describing systems which form or evolve as a random sampling of states from a distribution [98]. They are built from algorithms which mimic stochastic processes with one famous example being a random walk. Within the context of materials, this is particularly powerful for modeling diffusion [51, 227], various types of relaxation [72, 102], and any behavior dominated by activation energy barriers.

Dislocation Dynamics (DD) simulations model dislocation interactions through a continuum elasticity description of dislocations [113, 219]. The technique can provide insight to how dislocations impact the stress-strain behavior of a material and visualize the types of dislocation structures which form. In these simulations, dislocations are typically confined to gliding within their slip plane and struggle to account for large-scale distortions to the lattice [48]. Though none of these techniques are directly calculated for this work, they provide context for referenced literature and highlight some of the approaches to modeling materials from the atomic-level.

Molecular Dynamics (MD) simulations use Newton's equations of motion to link the forces and acceleration of each atom through prescribed interatomic potentials. From here the trajectories for each atom can be calculated, and we can construct a picture of atomic-level motion in person to applied mechanical stimuli and as a function of temperature. These simulations are often computationally limited to nanosized volumes (~60 x 60 x 60 nm) and strain rates ≥ 10^5 s^{-1}, which are orders of magnitude above the quasi-static limit of 10^{-3}. Thus the stress values are often over-estimated and provide a more qualitative or rough estimate than precise predictions. Nevertheless, this technique has been applied to various fields due to its powerful insight to the atomic mechanisms and structures correlated with mechanical response [5, 14, 41, 71, 143, 197]. The simulations discussed in this thesis are MD simulations.

1.5 Size Effects

Famously shown in the Hall-Petch relationship [74, 158], the hardness of material can change as a function of grain size particularly at the micro and nano-scales. This scaling of material property with lengthscale is one example of a size effect. More broadly, size effects can be categorized as either intrinsic (i.e., microstructurally driven) or extrinsic (i.e., dependant on the sample dimensions). The Hall-Petch relationship exemplifies an intrinsic effect where the forces necessary to transmit dislocations depend on the distance a given dislocation is away from a grain boundary and its ability to pile up at those boundaries. In contrast, the strengthening of singlecrystal materials for structure/sample sizes approximately the order of a micron and below demonstrates an extrinsic size [2]. Some size-based scaling is governed by an interplay between both intrinsic and extrinsic size effects as demonstrated with the "smaller-is-weaker" effect demonstrated in nanocrystalline platinum nanopillars with only a few grains across the feature [70]. These small-scale, boundary-containing materials are often linked to emergent or unique mechanical responses due to opportunity for coaction between size effects.

Intrinsic Effects

Intrinsic size effects can primarily be described by the breakdown in the continuum-like experience of atomic processes and shifting dominance in mechanism. Another example in addition to the Hall-Petch relationship is nanotwinned materials which demonstrate a fantastic mix of increased strength while maintaining a high degree of ductility [129, 229]. This behavior arises from the intrinsic size effects related to the close spacing of twin boundaries. In the correct orientation, these boundaries act as barriers to plasticity motion but do not allow for large concentration of stress or lattice incompatibilities which drive the typically brittle behavior of nanocrystalline materials [121, 200].

Another kind of intrinsic size effect is exemplified through the inverse Hall-Petch effect. Unlike the classic Hall-Petch, the inverse Hall-Petch explains a softening behavior with decreased size. This phenomenon is primarily observed in materials with grain size below

~30 nm, though the transition from hardening to softening can occur earlier [2]. This has been shown experimentally and through simulations to be a shift to grain boundary slip, slide, and rotation as the stresses needed to form, propagate, and transmit dislocations becomes higher than the stress needed to activate grain boundary relaxation [32]. Ongoing work is still probing how differences in grain boundary orientation and energy[10] can influence the transition from Hall-Petch to inverse Hall-Petch regimes [10, 146].

Extrinsic Effects

Studies in nanomechanics have linked extrinsic size effects with increased access to the free surfaces, the decreased presence of certain microstructural features like dislocation sources, and shifts in the balances of forces at the atomic lengthscale. Various work has shown increased stiffness and piezoelectric response in nanomaterials [4, 5, 220]. Simulation and theory work hypothesizes this effect comes from the enhanced fraction of surface atoms whose bonds contribute differently to elastic behavior.

Most metals show increased yield strength with decreased size below the order of a micron. Though the specific mechanisms for size effect in FCC, BCC, and non-cubic structures vary due to difference in plasticity mechanisms, all are rooted in changes to the ability for nucleation and propagation of dislocations [2].

Extrinsic size effects also manifest in failure behaviors like the brittle-to-ductile transition in ceramics arises from suppression of fracture leading to high stored stress within the material. This enables dislocation mediated ductility which is not otherwise accessible in a brittle material [231]. Metallic glasses undergo a similar brittle-to-ductile transition that stems from suppression of shear band nucleation and transfer of stress relaxation to local atomic reconfiguration [109, 111].

In a more complex mixture of intrinsic and extrinsic size effects, Gu *et al.* [71] demonstrate how nanocrystalline nanoscale materials can become flaw intolerant as stress may concentrate and reach the critical failure stress at microstructural features like triple junctions rather than a flaw.

At its core, size effects are a manifestation of the breakdown in continuum-like assumptions as materials shrink to the microscale and beyond. Through the interaction between various types of boundaries and atomistic mechanisms, observed properties shift to what is unex-

---

[10] Grain boundary energy can be influenced by boundary misorientation angle, segregation of species at the boundary in alloys, grain boundary complexions, and grain boundary width. These energetics are usually investigated through simulation, theory calculations, and TEM related analysis.

pected in our macroscopic mindsets but energetically straight forward from the smallest point of view.

Chapter 2

FAILURE OF HIGHLY ALIGNED BRITTLE NANOWIRE BUNDLES

This chapter has been adapted from:

Rebecca A. Gallivan and Julia R. Greer. Failure mechanisms in vertically aligned dense nanowire arrays. Nano Letters, 21(18):7542–7547, 2021. doi: 10.1021/acs.nanolett.1c01944

From applications as bulk-like forests in composites and coatings to integration into micro- and nano-scale sensors, vertically aligned nanowires have becomes critical components in novel devices and materials. Zinc oxide (ZnO) is a common material in many micro- and nano-electromechanical system (MEMS/NEMS) designs due to its easy, inexpensive fabrication and strong piezoelectric response. Its large intrinsic electromechanical coupling of 12.4 pm/V occurs along the c-axis of the crystal and makes ZnO an ideal material for actuation and force sensing [38]. ZnO is also commonly used in other nanowire applications such as electrical components and protective coatings [204, 212]. It is critical to understand the response of nanowires to mechanical stimuli, as a collective unit, to ensure reliability in technological applications.

The mechanical behavior of individual ZnO nanowires, in particular elastic modulus, bending modulus, and failure strength, have been explored extensively [54, 204, 212]. For example, molecular dynamics (MD) simulations and *in-situ* transmission electron microscopy (TEM) experiments by Agrawal *et al.* [3] demonstrated a 14% increase in the elastic modulus of [0001]-oriented ZnO nanowires when their diameter was reduced below 80 nm [3]. Work by Xu *et al.* [202] corroborates these results and identifies surface stiffening in nanowires under 80 nm as the main contribution to this elastic size effect [202]. Xu *et al.* [202] also reports an increasing failure strain with decreasing nanowire diameter and failure strain of up to 6% for 20 nm diameter nanowires [202].

The properties of ZnO nanowires in composites, forests, etc. have also been reported and highlight the bulk-like continuum behavior that arises in coatings and other structural reinforcements [123, 134, 208, 214]. Young *et al.* [214] demonstrate the presence of Euler buckling in aligned ZnO nanowire forests, while Yang *et al.* [208] show the impact of packing density on measured load-depth response during indentation [208, 214]. Adding ZnO nanowire forests as a reinforcing element in composites has been shown to improve the interfacial shear strength by 113% by Lin *et al.* [123], while Malakooti *et al.* [134] uses it for both increasing tensile strength by 18.4% and introducing an energy-harvesting capability [123, 134].

A dearth of studies exists that captures the mechanical response and failure of micro-sized samples that contain a finite number of densely packed ZnO nanowires. At this structural length scale, both the discrete and collective mechanical response of the nanowires may contribute to their overall mechanical signature that arises from the interplay among individual nanowire behavior and interfacial contributions. This work highlights the substantial role of interfacial mechanisms governing failure behavior of microsized nanowire structures. For devices where these meso-scale components have become increasing prevalent, such as tactile sensors [44, 145], novel memrisistors [163], and self-cleaning coatings [215], it is critical to characterize and explore the fundamental role of interfaces in structural failure for future generations of devices.

2.1 Fabrication of ZnO Nanowire Bundles

Template Fabrication

Zinc oxide nanowires are hydrothermally grown into various µm-diameter cylindrical bundles using a mask template method shown in Figure 2.1a. The substrate is prepared by depositing first a 10 nm platinum adhesion layer and then a 100 nm gold layer via e-beam evaporation (Lesker Labline) onto a silicon substrate. This enables good electrical contact for the nanowire growth process. Next, a poly(methyl methacrylate) resist (950 PMMA A9) is spin-coated onto the substrate giving a 1 µm-thick coating across the substrate. The resist is then patterned into an array of holes via e-beam lithography (Raith EBPG 5000+) using a 30 nA beam. Holes are patterned as 2, 4, 20, and 40 µm diameter circles in 20 x 20 arrays with 150 µm spacing between the center of the holes. This holey PMMA coating acts as a template which allows nanowire growth only in the exposed regions.

All nanowire bundles used in these experiments are grown for 6 hours to create structures sufficiently tall for good mechanical testing. Section 2.2 provides more details regarding nanowire dimensions and morphology. After nanowire growth was halted, the PMMA mask was etched away by submersion in acetone. The substrates were washed with isopropyl alcohol to remove debris and air-dried in a fume hood. A representative bundle after the template removal is shown in Figure 2.1b. A representative SEM image of a cleaved 20 µm diameter bundle show highly aligned and dense nanowires throughout the structure (Figure 2.1c).

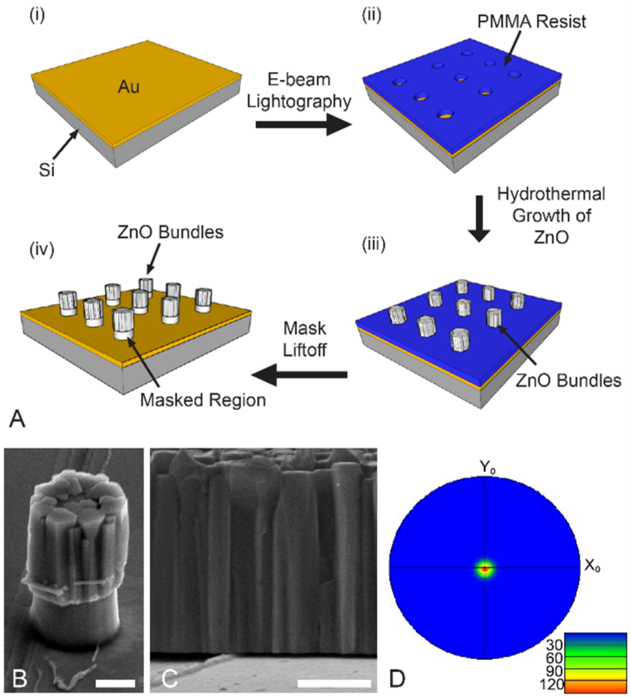

Figure 2.1: **Hydrothermally Grown ZnO Nanowire Bundles.** (a) Depicts the fabrication schematic where (i) the initial Si substrate is coated Au before (ii) e-beam lithography patterns PMMA resist. The substrate is then used for hydrothermal growth to produce (iii) nanowire bundles in the holes. (iv) Removal of the PMMA resist leaves free-standing bundle structures. SEM image of (b) an individual representative nanowire bundle and (C) a cleaved bundle show highly aligned and dense nanowire structures. (d) An EBSD pole map from the top surface of a bundle shows high alignment of the nanowires along <0001> direction. All scale bars are 1µm.

Nanowire Growth

Nanowires were formed using an electrolysis-aided hydrothermal technique in which aqueous zinc ions (Zn^-) and hydroxide (OH^-) form precipitated zinc oxide via a layer by layer growth following the scheme below [17]:

$$Zn^{2+} + OH^- + \text{vacancysite} \longrightarrow Zn(OH)^+{}_{ads}$$

$$Zn(OH)^+{}_{ads} + OH^- \longrightarrow ZnO + H_2O \tag{2.1}$$

Note that the subscript *ads* refers to the adsorption of the species onto the substrate or vacancy site rather than an being present in the aqueous environment. This work employed a growth solution consists of a 1:1 volume solution of 25 mM of zinc nitrate hexahydrate ($Zn(NO_3)_2{\cdot}6H_2O$) and 25 mM of hexamethylenetetramine (HMTA; $C_6H_2N_4$). HMTA was chosen as a growth aid as it binds to the non-polar $<10\bar{1}0>$ faces of the growing ZnO crystals effectively inhibiting side-wall growth and promoting high-aspect-ratio nanowires [114, 213]. The growth solution was also heated to 90 °C to increase the reaction rate.

The substrates were loaded as the cathode of an electrolysis cell prior to being submerged in the growth solution. This electrolysis reaction helped to increase local concentration of OH^- which also pushed the reaction toward the desired product and increased the rate of nanowire growth. Appendix D.1 provides schematics and further details of the electrolysis process used in these experiments.

2.2 Nanowire Bundle Characterization

Scanning Electron Microscopy

SEM images show a dense growth of nanowires in the bundle structure. The bundles are characterized by a smooth base region which corresponds to the template mask constraining nanowire growth in the radial direction and a flat-faced region above the mask. These hexagonal cross-sections of the nanowires are typical of single crystal ZnO [17]. Investigation of a cleaved µm-diameter bundle highlights the aligned, dense nanowires throughout the structure and the preservation of flat faceted interfaces between nanowires.

Using ImageJ, nanowires are shown to have an average diameter of 301 +/- 31 nm and and average height of 4.00 +/- 0.15 µm independent of bundle size. Alignment of nanowires normal to the surface was also measured in several images. All observed misalignment was less 5° (see Figure D.2 in the appendix for tilt distribution).

In the initial stages of nanowire growth, the bundle experiences boundary constraints of the template, which results in the smooth base region, and once above the mask, the nanowires starts to form flat facets (Figure 2.1b). SEM images show that the morphology of the nanowires on the interior of a cleaved bundle is preserved throughout the height of the bundle, and that the nanowires remain dense and aligned throughout the whole structure (Figure 2.1).

Electron Backscatter Diffraction

Bundles with 20 µm diameter bundles were used for probing nanowire orientation via electron backscatter diffraction (EBSD)[1]. The substrates were loaded into an Oxford EBSD system in a ZEISS1550VP scanning electron microscope, and bundle orientations were imaged from the top surface. Figure 2.1 shows the EBSD pole map for {0001}orientation. This map confirms that the <0001> direction of these ZnO nanowires is highly aligned with the direction normal to the substrate.

---

[1] More information on the technique can be found in Appendix M.

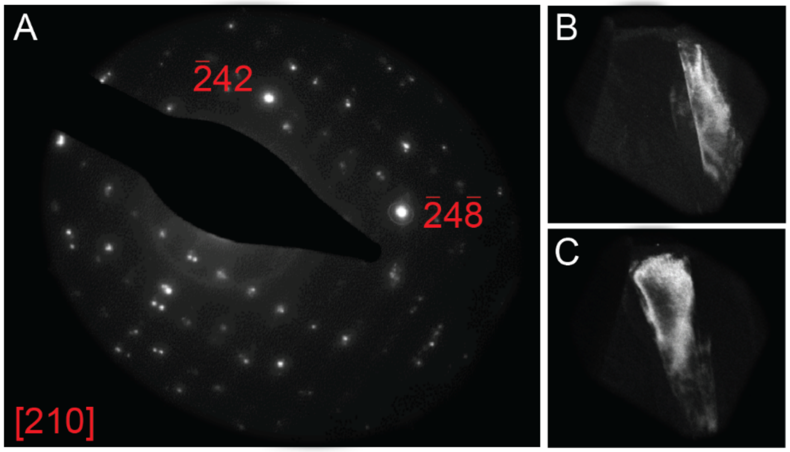

Figure 2.2: **TEM Images of a Nanowire Bundle.** (a) The diffraction pattern corresponding to the vertical cross-section of a representative 2 µm bundle down the [210] zone axis. (b-c) Dark field images corresponding to the diffraction spots $[2\bar{4}2]$ (b) and $[\bar{2}4\bar{8}]$ (c) highlighted in A which show individual single crystal nanowires present in the bundle structure.

Transmission Electron Microscopy

To further investigate the microstructure of the nanowires, TEM samples were imaged in an FEI Tecnai TF-30ST. Appendix D.3 outlines the specific liftout method used to prepare 2 µm diameter bundles for imaging. Using a 300 kV beam, we obtained diffraction patterns of ZnO (Figure 2.2a) and dark field images (Figure 2.2b-c) of the bundles taken with a 20 µm objective aperture. The diffraction pattern reveals a set of overlapping single crystal diffraction patterns which share a zone axis of [210]. The slight offset of the diffraction points results from rotation about the <0001> of the individual nanowires as their orientation in the r-θ plane is not constrained during nucleation. Dark field analysis in Figure 2.2b-c provides further confirmation that the bundles are composed of single crystal nanowires along their entire length.

2.3 Nanomechanical Testing of Nanowire Bundles

Experimental Set-up

Uniaxial compression experiments on 49 bundles were performed *in situ* with a Quanta SEM (ThermoFisher Scientific) equipped with an InSEM nanomechanical module (Nanomechanics, Inc.) using a 5 µm stainless steel flat punch tip [66]. Compression was chosen for the following experiments as it is the anticipated type of loading mode during use of such structures in nanotechnology applications. Additionally, the processing disallowed the addition of grip area for nano-tensile experimentation and adhesion to the substrate is likely weaker than the tensile strength of the structure.

Samples were loaded to ultimate failure under displacement control at a quasi-static strain rate of 10^{-3} s^{-1}. Ultimate failure was determined as the point of structural collapse with no ability to bear an applied load. Mechanical results are reported as engineering stress versus strain, calculated as:

$$\frac{F_i}{A_0} = E\frac{d_i}{l_0} \tag{2.2}$$

where F_i is the instantaneous measured force, A_0 is the initial contact area, E is the Elastic Modulus, d_i is the instantaneous measured displacement starting from initial contact, and l_0 is the initial height of the bundle. This can otherwise be written as:

$$\sigma = E\varepsilon \tag{2.3}$$

where σ is the engineering stress and ε is the engineering strain. Appendix C outlines additional information on Sneddon corrections, data treatments, and limitations around stiffness measurements in this experimental method.

Failure Behavior and Analysis

Experimental results on the compression of 29 bundles with 2 µm diameters (approximately 10-30 nanowires) and 20 bundles with 4 µm diameters (approximately 70-130 nanowires) indicate that the initial failure occurred through vertical splitting along the nanowire interfaces before the structure undergoes ultimate failure. Figure 2.3 illuminates this behavior through a series of frames from a typical *in-situ* micro-compression experiment. The stress-strain data in Figure 2.3 reveals that the bundles are first loaded elastically (Region I) until experiencing one or more “burst” events in Region II, which correspond to localized splitting along the interface between nanowires. These bursts are characterized by a rapid displacement excursion at a virtually unchanging load at a stress between 0.3 GPa and 1.3 GPa for all bundle diameters. Nanowire bundles undergo ultimate failure (Region III) at a stress between 0.83 GPa and 2.20 GPa for 2 µm diameter bundles and within 0.90 GPa and 2.20 GPa for 4 µm diameter bundles.

To describe the failure behavior of these micro-bundles, we first characterize the mechanism that drives the localized burst events and propose a predictive model which links localized failure to structural collapse. The burst events in Region II correspond to a dynamic splitting along the nanowire interfaces, driven by the released elastic energy that overcomes the cohesive interaction force during separation. A lower post-burst loading slope indicates a loss of stiffness and a reduction in load-bearing capabilities of the bundle, consistent with localized failure. While initial instability could be generated via buckling or other mechanisms, the observed energy dissipation and localized failure is always carried out via interfacial splitting. Figure 2.3 presents a schematic of a Mode I-loaded double cantilever

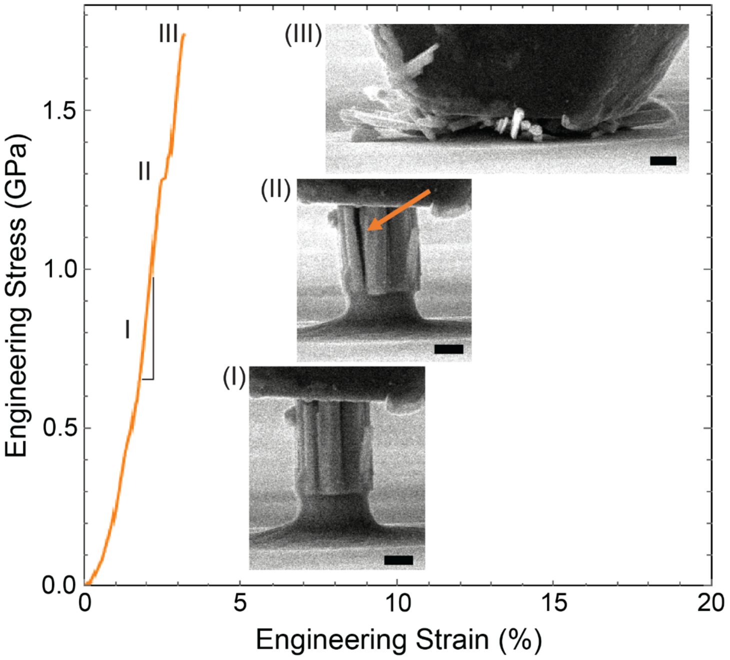

Figure 2.3: ***In-situ* compression of a ZnO nanowire bundle to failure.** The snapshots highlight the mechanical response of a representative 2 μm diameter (~15 nanowires). Engineering stress vs. strain with SEM images that correspond to pertinent regions of (I) initial loading, (II) incipient splitting, and (III) ultimate catastrophic failure. All scale bars are 1 μm.

beam test (DCB) model where the slightly misaligned nanowires are pushed apart under axially applied load, and the crack propagates against the interfacial adhesion. The SEM images of such splitting, shown in Figure 2.3, provide support for the applicability of this model to study the interfacial splitting phenomena in the ZnO bundles. Using this framework, the applied opening load, P, is related to the interfacial fracture toughness, K_{IC}, through the largest stable flaw size at the interface, a:

$$a = \frac{K_{IC}^2 b^2 h^2}{12P^2} - \frac{h^2}{3} \tag{2.4}$$

where h is the interface thickness and b is the thickness of the individual wires [199]. Only those nanowires that are either slightly misaligned with respect to the substrate or contain defects can exhibit this cantilever behavior. The tilt angle, θ, produces the necessary opening force:

$$P = F sin(\theta) \tag{2.5}$$

with F being the applied axial load on the bundle.

Using this model, we can estimate what type of interaction dominates the nanowire interfaces under the assumption that the nanowire tilt is below ~5° (Figure 2.4) and the internal flaws do not exceed 300 nm (~5-8% of the nanowire length). If no pre-existing flaw is sufficiently large to activate crack propagation, the bundle would be expected to fail intrinsically at a stress close to the theoretical shear strength of ZnO, ~5 GPa [60, 117]. It is reasonable to assume that the cohesive interaction forces at the nanowire surfaces lie between the lower bound of weak van der Waals forces and the upper one of a high-energy grain boundary. Previous experimental results identify the interfacial toughness of a ZnO-ZnO grain boundary to be 2.5 MPa$\sqrt{m}$ [13, 144, 168]. Density-functional theory (DFT) calculations identify the surface energy associated with a van der Waals interaction along $\{10\bar{1}0\}$ planes of ZnO to be 1.39 Jm^{-2} [164]. Using the following relationship between fracture toughness of a brittle material, K$_{IC}$ and surface energy, γ:

$$K_{IC} = \sqrt{2\gamma E} \tag{2.6}$$

where E is the elastic modulus of ZnO in the $\langle 10\bar{1}0 \rangle$ direction, defines the lower bound for interfacial toughness to be 0.58 MPa$\sqrt{m}$. Figure 2.4 overlays these computed bounds onto the experimentally obtained stresses of the initial burst events for all compressed samples. This comparison demonstrates that only the lower bound captures experimental data, with even the largest tilt at the upper bound being 4.3 times higher than the experimental results. The data indicates that the initially delaminated inter-wire regions or flaws with dimensions of 70-300 nm can initiate splitting and support the phenomenological explanation of the burst behavior.

Experimental artifacts, like minor variations in the nanowire heights and a slight misalignment between the nanoindenter tip and the top surface of the bundle, can create local concentrations of stress, which will initiate splitting at lower globally applied forces. We probe only the first burst event in the data, which is initiated by the largest initially present defect. The initiation of local failure increases the applied stress supported by the remaining wires and renders the measurement of smaller flaws impractical.

All micro-compression experiments on the 2 μm diameter bundles (10-30 nanowires) and the 4 μm diameter bundles (70-130 nanowires) show a similar distribution of ultimate failure stresses with a mean of 0.64 +/- 0.31 GPa and 0.58 +/- 0.27 GPa respectively. The range of failure stress is also identical with values of 0.3-1.3 GPa (Figure 2.5). This independence of failure stress on bundle size suggests an identical failure mechanism in all bundles and a characteristic length scale of failure of at least an order of magnitude below the micron scale.

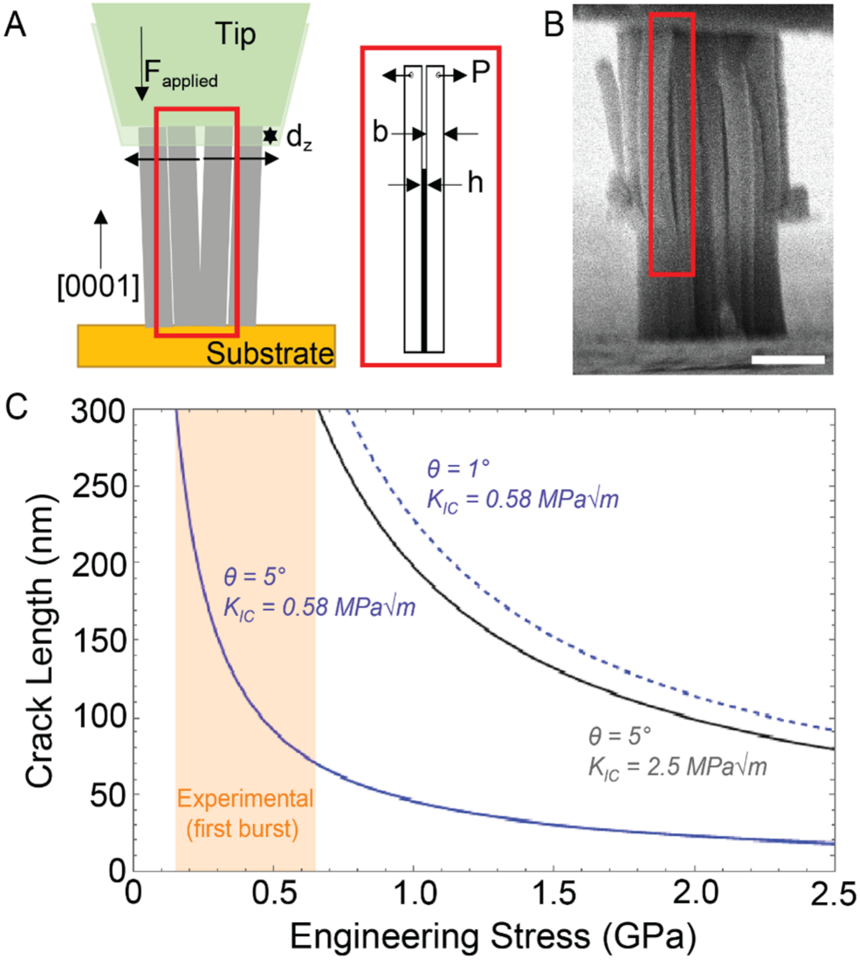

Figure 2.4: **Contribution of Flaws at the Interface to Structural Failure.** (a) Schematic illustrating the bundle-splitting mechanism along nanowire interfaces using an analog Mode I double cantilever beam (DCB) test where P is the bending force, b represents individual thickness of wires, and h is the interfacial thickness or interaction distance. (b) SEM image of nanowire interfacial splitting during loading that supports mechanism illustrated in (a). Scale bar is 1µm. (c) Plot of the maximum stable flaw size denoted as a based on Mode I DCB using 1° and 5° bounds for the tilt angle, θ, and a fracture toughness of the interface, K_{IC}, which is bounded by 0.58 MPa$\sqrt{m}$ from van der Waals interaction and 2.5 MPa$\sqrt{m}$ from a grain boundary-like interface. The orange band represents the range of experimental failure stresses defined by of the first burst.

2.4 Modeling and Predicting Failure

To predict the range of failure stress in the bundles, we propose a probabilistic model that is based on the dynamic interplay of several nanowires losing their ability to support the applied force, transferring it onto the remaining nanowires, and increasing the local true stresses experienced by the remaining wires in the bundle. The true stress, σ_T, on the bundles is defined as:

$$\sigma_T = \frac{F_i}{A_i} \tag{2.7}$$

where F_i is the instantaneous applied load, and A_i is the instantaneous contact area. The bundle undergoes ultimate failure, σ_{ult}, when the remaining wires reach the critical failure stress of the material, $\sigma_{T,c}$.

$$\sigma_{ult} = (1 - f)\sigma_{T,c} \tag{2.8}$$

Here, f denotes the fraction of failed nanowires, and $\sigma_{T,c}$ lies between the Euler buckling stress of 2 GPa (Appendix E.2) and 5 GPa, the theoretical strength. Following the framework of Ngan *et al.* [164], we represent the fraction of failed nanowires in a bundle at a given engineering stress, σ, using a Weibull-based distribution of failure assuming iso-strain conditions:

$$f(\sigma) = 1 - Exp\left[\frac{-\nu N}{\dot{\sigma}} \int_0^{\sigma} exp\left[-\left(\frac{\sigma_c}{\sigma'}\right)^m\right] d\sigma'\right] \tag{2.9}$$

Eq. 2.9 describes the fraction of failed wires in the bundle, $f(\sigma)$, based on the total number of wires in the bundle, N, the Weibull modulus of the failure mechanism, m, the critical failure stress, σ_c, the failure attempt frequency, ν, and the rate of stress application, $\dot{\sigma}$. Thus, $-\nu/\dot{\sigma}$ represents the rate of failure attempts as stress is applied. Our experiments demonstrate equivalence in the range and the distribution of failure stresses at burst initiation for 2 and 4 µm diameter bundles (Figure 2.5), which implies that m and $-\nu/\dot{\sigma}$ are invariant of N.

To capture the range of stresses associated with structural failure, the upper bound of σ_c corresponds to the theoretical strength of single crystalline ZnO, 5 GPa, (shown as a dotted line in Figure 2.5a) and the lower bound of σ_c represents the largest pre-buckling burst stress, 2 GPa (shown as a solid line in Figure 2.5a). The intersection of Eq. 2.8 (grey lines) and Eq. 2.9 (red lines) indicates the critical fraction of nanowire failure necessary for structural failure given a total number of wires, N. We bound the range of ultimate failure stress given this model of accumulated localized failure using 130 nanowires for the lower bound (i.e., euler buckling) and 10 nanowires for the upper bound calculation (i.e theoretical shear strength)[2]. These values of N are typical in 2 and 4 µm bundles. Optimizing the spread in failure stresses to match the experimental data results in a Weibull modulus of

---

[2] This means that for the solid red line plotted in Figure 2.5a the σ_c used is 2 GPa and N is 130. For the dotted red line in Figure 2.5a, the σ_c is 5 GPa and N is 10.

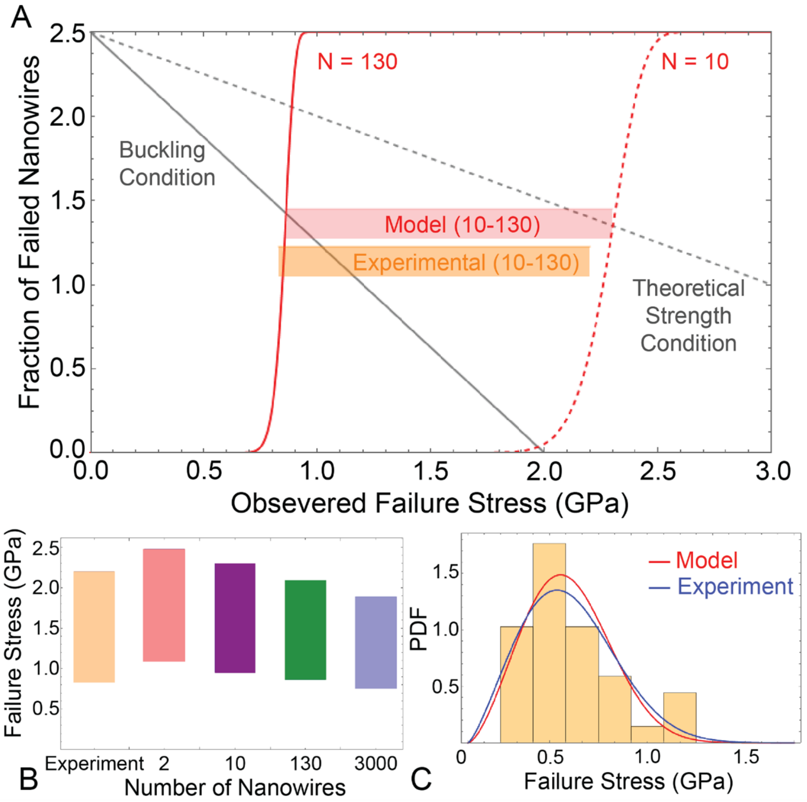

Figure 2.5: **Statistical Model for Describing Failure.** (a) The expected fraction of failed nanowires (denoted by the shaded region) given Weibull Modulus of 2.55 and $-\nu/\dot{\sigma}$ of 1000. The lower bound is set as 2 GPa (solid line) and the 5 GPa theoretic failure stress serves as the upper bound (dashed line). Comparison of model and experimental results for (b) expected failure values for range of bundle sizes and (c) optimized Weibull distribution from model with experimental data for failure stress.

2.55 and a $-\nu N/\dot{\sigma}$ term of 1000 GPa^{-1}. Figure 2.5b shows the range of failure values calculated from the model match well to the range of experimental values. The model predicts a slight decrease in the range of possible failure stresses and a small reduction in the predicted failure stress with increasing number of nanowires. However, these values are mostly overlapping for 2 to 3000 nanowires and sit within the observed range of the experiment. Thus, no strong number dependence is observed or predicted for the stress at failure, further supporting the validity of this predictive approach. Figure 2.5c conveys close agreement between the probability distribution of experimental failure stresses versus those calculated using the Weibull modulus of the splitting mechanism.

Analysis of failure in the bundles requires understanding the relationship between localized failure and critical failure stress. The statistical model for failure stress links the local failure mechanism to the global structural failure through the Weibull modulus. This parameter qualitatively reflects the distribution of local weak regions across the bundles, with Weibull moduli close to 1 indicating a high variance in flaw distribution between samples. The calculated Weibull modulus of 2.55 for the micro-sized bundles in this work is significantly below that of individual nanowires, m = 5.95 [167], which implies a higher variation in defect size and/or other interfacial flaws from bundle to bundle as compared to the material itself. Though the observed distribution of initial burst events may skew to lower values than the true distribution of activated failure mechanisms, the optimized modulus (2.55) and the fit modulus (2.3) are in good agreement and support the utilization of this statistical method.

We pull further insight from the stress distribution of initial burst events to investigate the interplay between the interfacial defects. For the same nanowire growth density, the number of interfaces increases with bundle diameter, which suggests the presence of more weak points across larger bundles and their lower failure stresses. However, the low observed Weibull modulus indicates that the failure mechanism is likely at least an order of magnitude below the structure size. This difference in length scale can lead to a masking of this anticipated size-based effect on failure. The experimental data support this insight from the Weibull modulus as the 4 µm bundles and the 2 µm bundles have identical failure stresses and distributions.

We further understand this size independence of the failure stress to indicate that the variance in flaw size does not solely drive the burst failure distribution. We observed that the variation in tilt angle strongly affects the resulting failure stress of a burst. Two bundles with the same distribution of flaws but 1° difference in tilt angle of the nanowires could result in up to a 0.43 GPa difference in failure stress, almost half the observed range. Alternatively, a failure stress of 0.7 GPa could be produced by a crack that is 163 nm and has a tilt of 4° or by a defect that is 217 nm long with a 3° tilt (calculations in Appendix E.1). Though other factors may contribute to the observed distribution of stress at failure initiation, the combination of flaw and tilt angle distribution among the bundles are both prevalently observed and likely the primary contributions to failure.

2.5 Summary and Conclusions

We demonstrate that failure in densely grown hydrothermal ZnO nanowire micro-bundles occurs locally, by splitting along the weakly interacting nanowire interfaces, at stresses in the range of 0.3-1.3 GPa. The ultimate bundle failure ranges from 0.83-2.1 GPa, with no observable dependence on number of nanowires in the bundle. This phenomenon likely arises due to an interplay between the distribution of defects between bundles and tilting angles. As nanowires split along the relatively weaker interfaces, the true stress on the remaining wires increases and subsequently enables additional failure events. After accrual of sufficient local failure, the remaining material can no longer support the applied load, and catastrophic structural failure occurs. We model global failure using a statistical approach, which calculates the expected extent of failure at a given stress and compares it to the critical material failure conditions.

This work highlights the importance of interfacial considerations at the nanoscale. In a macroscopic setting, accumulation of local failure would be dominated by the failure of individual wires rather than failure at the interface. However at the nanoscale, the interface in nanowire structures is dominant. These experiments demonstrate the importance of considering interfacial interactions even when bonding is not present. Further experimentation may look at the role of processing, additives that preferentially decorate the surfaces, or directed chemical alteration of interfacial energies.

This work also provides analysis of failure in dense ZnO nanowire micro-bundles and demonstrates the efficacy of the proposed probabilistic model in evaluating and predicting failure behavior of aligned arrays. This failure analysis could be extended to any structure where accumulation of independent localized failure events leads to a catastropic global failure. While one would need to account for any added complexities of stress states, such a treatment could be extended to even brittle nanolattices where localized failure in individual nodes or beams accumulates, leading to global reduction in load-bearing capabilities.

Chapter 3

INSIGHTS TO ELECTROMECHANICAL BEHAVIOR IN NANOCRYSTALLINE NANOSCALE PIEZOELECTRIC MATERIALS

This chapter has been adapted from:

Rebecca A. Gallivan, Zachary H. Aitken, Antoine Chamoun-Farah, Yong-Wei Zhang, and Julia R. Greer. Emergent mechanical and electromechanical behaviors in additively manufacture nanocrystalline zinc oxide. *Manuscript in preparation.*

R.A.G. and J.R.G. conceived of the experiments. R.A.G. synthesized samples, performed experiments, analyzed data, and formulated analytic the model and its application. A.C.-F., Z.A.H., and Y.-W.Z. generated and analyzed the isolated grain boundary simulations. Z.A.H and Y.-W.Z. generated and analyzed the polycrystalline simulations. All authors discussed the findings. R.A.G. and Z.A.H. wrote the manuscript. All authors edited and have given approval to the final version of the manuscript.

ZnO is a material of particular interest in the world of micro- and nano-scale devices due to its strong, intrinsic piezoelectric effect[1] which occurs along the c-axis. The response is primarily an elastic, reversible, distortion of the lattice and thus the effect is intrinsic to the crystallographic orientation of the crystal. single crystal ZnO has a measured piezoelectric response (d_{33}) of 12.4 pm/V [92] whereby a mechanical (or electrical) stimulus applied along the c-axis of the crystal creates a spontaneous electrical (or mechanical) response along the c-axis. This property makes ZnO a promising material for applications in sensors, energy harvesting, actuation, micro- and nano-electromechanical system (MEMS/NEMS) designs, and many other applications [25, 85, 151, 224].

However, at the nanoscale, ongoing investigations surround some observed size effects in ZnO's piezoelectric behavior. Various experiments have shown values ranging from 4.41 pm/V in nanorods under 500 nm to 12,000 pm/V in 230 nm diameter nanowires [55]. Agrawal and Espinoza demonstrate through first-principles calculation that ZnO nanowires

---

[1] The piezoelectric effect describes an electromechanical coupling phenomena found in some materials. Intrinsic piezoelectric materials display this electromechanical coupling only along specific crystallographic axes due to the fixed dipole structures within the lattice. These materials cannot be "poled" to align the electromechanical coupling of grains. More information about piezoelectricity can be found in Appendix F.

greater than 1.5 nm in diameter do not exhibit large size effects in piezoelectric response [50].

Thin films have also shown a variety of piezoelectric responses which primarily stem from texturing (i.e., grains are aligned into a common direction) [65, 206]. Since ZnO is highly directional in its piezoelectric response, various techniques which control the degree of alignment or preferential crystallographic texturing enable tuning and localization of electromechanical behavior [55, 65, 79, 135, 165, 206]. However, in the absence of grain alignment or in bulk conditions, polycrystalline ZnO is generally considered to have no piezoelectric response as the random orientation of each grain results in a net zero change in electric field.

This assumption is challenged by the work of Yee *et al.* that demonstrates an emergent electromechanical phenomenon in nano-architected nanocrystalline ZnO (nc-ZnO) [209]. While one may initially hypothesize that texturing, (i.e., grain alignment) due to the presence of a substrates or other factors could result in an observed electromechanical response, the following study shows that this piezoelectric behavior to be a size rather than texturing effect. Even with billions of grains present in the structure, there is remains ~1% of the single crystal response, which clearly highlights a slow approach to continuum-like behavior. The following chapter outlines an analytic model that relates the grain number to anticipated electromechanical behavior through experimental work and microstructural analysis. The developed collective electromechanical model matches the experimentally observed distribution and provides a basis for analyzing other intrinsic piezoelectric materials.

3.1 Fabrication of Nano-Architected ZnO via Photopolymer Complex Synthesis

Using PCS [209] (see Figure 1.1 for a schematic overview of the process and Appendix G.1 for detail of the formulation used in these experiments) nc-ZnO pillar structures are printed using two-photon lithography (Nanoscribe) on a silicon substrate. Structures are developed for 5 minutes in water to remove uncrosslinked polymer and then heated in a tube furnace (MTI, Vulcan OTF-1200X) under a prescribed heating profile. All heating is done at a 0.5 °C per minute ramp rate to a peak temperature. The sample is then held at that peak temperature for some amount of time before cooling at 1 °C per minute to room temperature. Samples are loaded by placing the silicon substrates in alumina boats inside a quartz tube (MTI, 60 cm length, 55 mm inner diameter). Heating occurs under atmospheric conditions. This calcining process both removes the water and organic material and nucleates the resulting ZnO material.

Three different peak heating temperatures were tested to understand the best conditions for

Temperature		
500 °C	700 °C	900 °
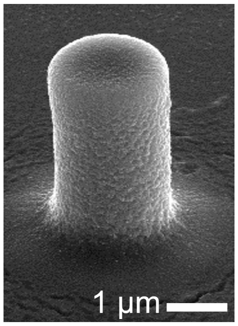	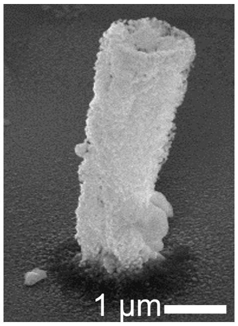	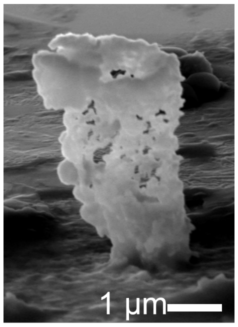

Table 3.1: **Representative Pillars for Various Peak Burn Times.** SEM images for pillars processed at 500 °C, 700 °C, and 900 °C which shown increasing porosity and lacy-like structures with increased temperature.

forming solid pillars with high fidelity to the original printed shape. Table 3.1 depicts the results of these heating profiles. Under 500 °C, the organic material does not burn away, leaving hydrogel matrices still intact so lower temperatures were not explored. Though cursory studies showed there may be some evidence for nucleation of particles within the matrix, questions surrounding the nucleation and growth phase of these materials are an area for continued investigation. At and above 500 °C, the pillars are fully converted to ZnO. Traditional processing of ZnO undergoes thermal treatment at 800-1000 °C [169].

For samples heated to 700 °C and 900 °C, the pillars are increasingly porous and eventually lacy structure as compared to those heated to 500 °C. Structures produced at 500 °C are the densest structures with the highest fidelity to the original cylindrical shape regardless of peak hold time. For speed of sample preparation, all samples used in this study are produced under the 500 °C peak temperature with no hold time at that peak temperature. The final structures range from 300 nm to 5 µm in diameter and followed a 2:1-3:1 aspect ratio of height to diameter to eliminate buckling of the structure while providing sufficient distance from the tip and substrate boundaries. Figure 3.1c highlights a representative pillar used in testing.

3.2 Microstructural Characterization of ncZnO

In order to contextualize the microstructural contributions to mechanical properties in the additively manufacture materials, TEM samples were prepared from representative pillars (Figure 3.1c) using a liftout method and imaged in an FEI Tecnai TF-30ST. (See Appendix G.2 for sample preparation details). Using a 300 kV beam, we obtained diffraction patterns

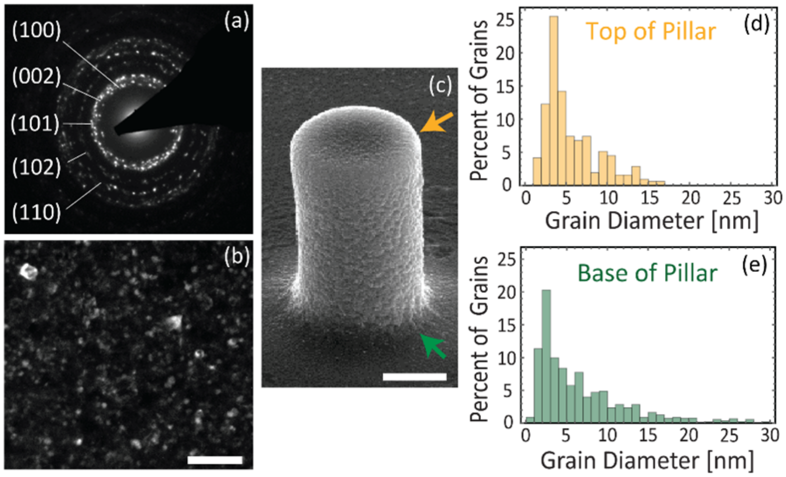

Figure 3.1: **Microstructure of Additively Manufactured Zinc Oxide Pillars.** (a) The TEM diffraction rings from a region at the bottom of the pillar which indicate a lack of texturing or preferred grain orientation and (b) a dark field image showing highlighted grains for grain size analysis. Scale bar is 100 nm. (c) An SEM image of a printed ZnO pillar approximately 2 µm in diameter with the resulting histograms of the grain distributions for the (d) top and (e) bottom regions of the structures showing similar and good agreement of the grain size distribution. Scale bar is 1 µm for image (c).

of ZnO to confirm the phase and identify any texturing (Figure 3.1a). Figure 3.1a shows clear diffraction rings which indicate a random orientation of the grains. The spacing of the rings also confirms the ZnO crystal to have a Wurzite crystal structure ($P6_3mc$) as expected[2]. We looked at a series of locations throughout the length of the structure under dark field conditions using a 20 µm aperture. These images as shown in Figure 3.1b highlight the nanocrystallinity of the microstructure and allow for grain size analysis. Specific methods of grain size analysis from dark field TEM images can be found in Appendix G.3.

Figure 3.1d-e provides histograms of the lognormal distribution of grains in the structure. The top region (Figure 3.1d) has an average grain size of 6.6 nm and a median grain size of 4.6 nm. The bottom region (Figure 3.1e) has a similar distribution of grain sizes with an average of 7.3 nm and median of 4.9 nm. Furthermore this analysis indicates a homogeneous distribution of nanocrystallites with no specific regions of larger or smaller grains. We will use the average grain size of 7.2 nm in estimating the number of grains present as this is the average when looking across the entire structure.

---

[2] ZnO is only known to form two other phases, rock salt ($Fm\bar{3}m$) and zinc blende ($F\bar{4}3m$). Rock salt phases form under pressures higher than ~9 GPa [47]. Zinc blende is a metastable phase which is primarily seen and stabilized during epitaxial growth of ZnO films [37].

3.3 *In-situ* Electromechanical Experiments

Experimental Set-up

In-situ electromechanical experiments are performed using a custom set-up in a Quanta SEM (ThermoFisher Scientific) with an attached InSEM Nanomechanical Module (Nanomechanics, Inc.). Samples are compressed with a 5 µm stainless steel flat punch tip coated in gold. Compression was chosen as it provided clear electrical contact and was compatible with the electronic components of the custom set-up. Additionally, challenges with surface adhesion between the printed ZnO and Si substrate as well as concentration of weakening points at the grip section for the half-dogbone tensile shape made tensile testing infeasible for these experiments. Wiring is attached to the tip and sample via copper clips as shown in the Figure 3.2a-b. Voltage measurements are taken using a Biologic Potentiostat with a low current probe attachment using an open-circuit configuration. (The electrical circuit and configuration is also described in [122].)

The voltage measured, V_{meas}, during pillar compression is the sum of the z components of the generated potential for each grain, $(v_z)_i$, as shown schematically in Figure 3.2c:

$$V_{meas} = \Sigma_{(i=1)}^{N} (v_z)_i \tag{3.1}$$

where N is the total number of grains in the structure. Pillars are compressed with the configuration shown in Figure 3.2d and the voltage change is correlated to displacement for 11 different pillars. A net change in voltage can be observed as a drop in the measured open circuit voltage which is proportional to the displacement of the structure (Figure 3.2e).

Experiments are done in the absence of the imaging electron beam to capture solely the material's electrical response. All samples are observed to be in good contact before electrical measurements in order to eliminate any electrical or mechanical effects from the tip contacting the structure. Samples are compressed to 2-3% strain through a prescribed displacement to avoid failure within the material. Before and after images (as shown in Figure 3.2d) confirm that samples remain in good contact and tests are valid.

Due to the electrical circuit present in this system, changes in voltage due to the sample are only reported as a drop in voltage equal to the absolute value of the change. Thus, all reported values of electromechanical behavior represent the absolute value of voltage and do not reflect the directional response of the material. Each compression is preceded by measuring the resistance of the silicon substrate and impedance of the circuit. This step ensures that all electrical connections are intact and provides confidence in the comparability of measurements.

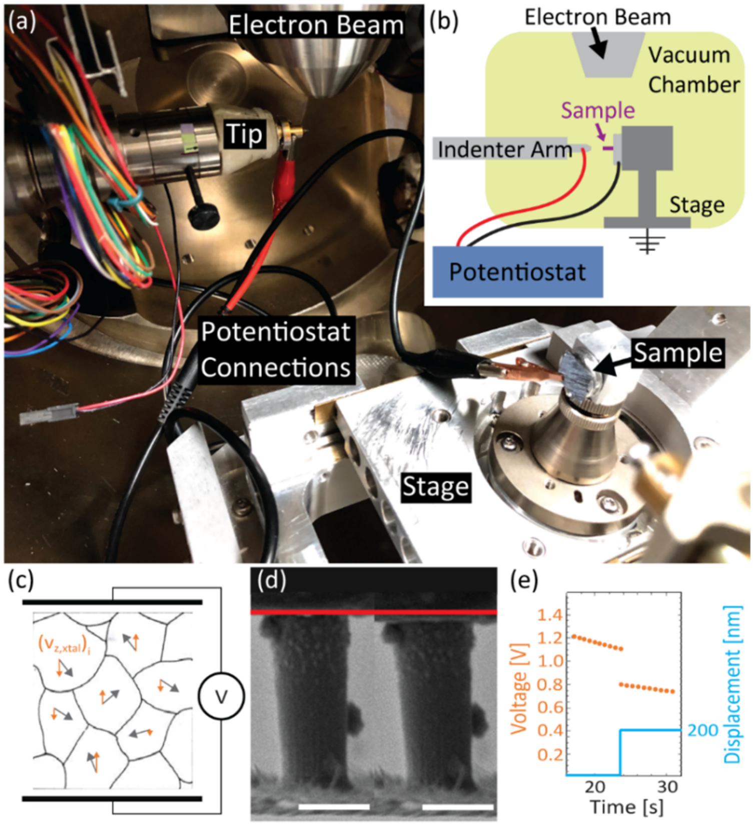

Figure 3.2: **Electromechanical Testing of Nano-architected Materials.** (a) An image inside of an open SEM chamber showing the custom set-up for *in-situ* electromechanical testing with labelled components. (b) Diagram inset provides overview of apparatus and connection to external potentiostat for electrical measurements. (c) Schematic representation of the printed zinc oxide's microstructure and the proposed relationship to the measured voltage of the structure. Grey arrows show the orientation of c-axis in the grains and orange arrows show the resulting component of electrical potential measured during compression of a pillar. (d) Representative before and after images of a pillar undergoing compression with blue line to guide the eye. Scale bar are 2 µm. (e) The resulting change in measured voltage of a representative nc-ZnO pillar under an applied displacement of 200 nm.

Results

The electromechanical behavior of the structure is reported as an approximation of the h_{33} piezoelectric coefficient[3] as we are looking at a change in electric field with respect to strain. This is achieved through dividing the absolute change in voltage by the absolute change in displacement. The 10 structures with 2-3 µm diameters (~100-350 million grains) showed a range of -0.022 mV/nm to -14.08 mV/nm. The structure with a diameter of 8 µm (~3 billion grains) had an electromechanical response of -0.04 mV/nm.

3.4 Analytic Modeling of the Emergent Electromechanical Response in Nanocrystalline Piezoelectric Materials

Without the presence of texturing, the observed electromechanical response appears contrary to standard assumptions that polycrystalline ZnO has no piezoelectric behavior. In describing this emergent phenomenon, we propose a collective electromechanical behavior model that introduces a dependance on number of grains present and accommodates the randomness of grain orientation. While specifically supported with evidence from ZnO structures, this model can be applied to any intrinsic piezoelectric material where the distribution of grain orientations and direction of both electrical and mechanical measurement is known. This model assumes no or limited generation of dislocations and preservation of bonds in the material, which is reasonable in nanocrystalline metal oxides and other intrinsic piezoelectric materials.

For our system, electrical and mechanical measurements are taken along the z-axis (Figure 3.2). We assume a uniform random distribution of orientation for the ZnO grains in the structure. During compression, grains first deform elastically and generate a piezoelectric response. The magnitude of each grain's elastic contribution will depend on the orientation of the c-axis with respect to the loading direction. Since the resulting electrical potential is produced along the c-axis, the measured voltage is described by Eq. 3.1. Since our structures undergo uniaxial compression, N will equal all grains in the structure.

As the grains are equally likely to be oriented in any direction, v_z for each grain will take on the uniform distribution $U(-h_{33}, h_{33})$ with a mean of 0.0 mV/nm and standard deviation of $h_{33}/\sqrt{3}$ where h_{33} is 1100 mV/nm [92]. For our system, h_{33} is calculated by divided v_z by the absolute displacement.

Each pillar can be constructed as random sampling of N randomly orientated grains. Thus, the pillars form a normal distribution of microstructures which results in a normal distribution of measured electromechanical response. The standard deviation of the measured

---

[3] See Appendix F and particularly Table F.1 for more details on piezoelectric coefficients.

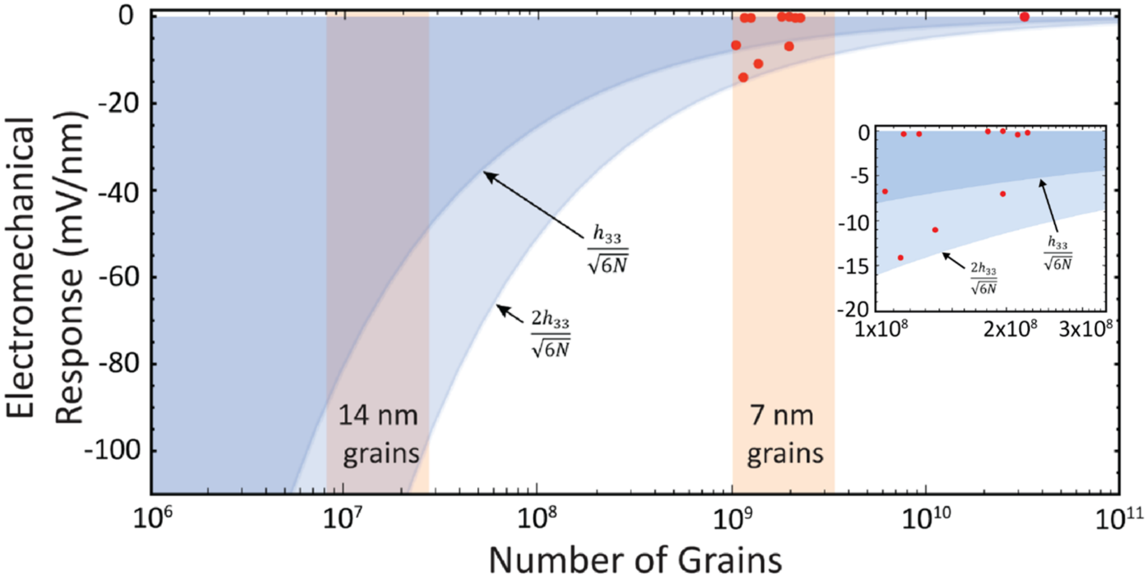

Figure 3.3: **Electromechanical Response of Nanocrystalline ZnO as a Function of Grain Number.** Red points correspond to observed sample response for pillars given the estimated grain number of each structure. The blue shaded region indicates the expected electromechanical response of structure based on the collective electromechanical behavior model for one standard deviation $\left(h_{33}/\sqrt{6N}\right)$ and two standard deviations $\left(2h_{33}/\sqrt{6N}\right)$, with N as the number of grains and h33 as the piezoelectric coefficient. The vertical bands indicated the estimated grain numbers for a 2-3 μm diameter pillar with a 1:2 aspect ratio given 7 or 14 nm grains. Insert graph highlights experimental data taken from 2-3 μm diameter pillars with ~7 nm grains.

response, σ_{meas}, is described as:

$$\sigma_{meas} = \frac{\sigma_{sample}}{\sqrt{2N}} \tag{3.2}$$

with σ_{sample} as the standard deviation of $U\left(-h_{33}, h_{33}\right)$. This can also be written as

$$\sigma_{meas} = \frac{h_{33}}{\sqrt{6N}} \tag{3.3}$$

with the derivation found in Appendix H. Note that the measured electromechanical response is not necessarily the maximal electromechanical response that the pillar could give for a particular set of grain orientations.

Using this analysis, Figure 3.3 highlights the expected range of electromechanical response in blue for 68% (one σ_{meas}) and 95% (two σ_{meas}) of samples (Equation 3.3). 70% of the experimentally tested samples fall within the first standard deviation, and 100% fall within two standard deviations of the anticipated range of values. Despite the effectively continuum microstructure seen in these nc-ZnO pillars, the highly anisotropic response of individual grains contributes significantly to the global behavior. Leveraging this model, we develop a stronger understanding of the sensitivity of nano-scale electromechanical behavior to grain number and highlight the relationship between observed behavior and fundamental parameters. The strong dependence on N is clearly illustrated as increasing grain size by a factor of 2, keeping all else the same, will increase the response of a pillar by a factor of ~10 (Figure 3.3). Additionally, at less than 10 million grains, the expected range of 95% of pillars rises to at least +/- 50.6 mV/nm.

3.5 Molecular Dynamics Simulations of Electromechanically-Coupled Behavior

Molecular dynamics (MD) provides insight to atomistic-level behavior and mechanical mechanisms in materials. To better investigate the underlying role of microstructure, and specifically grain boundaries (GBs) on electromechanical properties, this work utilizes MD simulations to investigate atomic-scale deformation in a ZnO nanocrystalline material. Previous MD studies on the electro-mechanical behavior of ZnO have chiefly focused on nanowire geometries for the intended use of energy generation [5, 14, 41, 143, 197]. This geometry provides a simple stress state but has limited application to samples fabricated via printing which often displays a nanocrystalline microstructure. Additionally these previously reported investigations do not provide insight to the role of GBs and grain boundary plasticity on electromechanical behavior. As far as the author is aware, this work provides the first reported study which applies MD techniques to explore the piezoelectric or mechanical response of ZnO with a nanocrystalline microstructure.

Two sets of simulations were performed, the first on a nanocrystalline microstructure. Considering the importance of intergranular deformation in nanocrystalline ceramics, the second set of simulations focused on isolated grain boundaries.

The nanocrystalline sample was cubic in geometry with 30 nm sides. The sample contained 40 randomly oriented grains that were initialized using Voronoi construction and each face of the simulation box employed periodic boundary conditions. Prior to compression, the nanocrystalline sample was thermally equilibrated at 300 K for 20 ps under zero stress. Compression was applied along a single direction at a strain rate of $2\text{x}10^{8}$ s^{-1} while maintaining zero stress boundary conditions in the orthogonal directions.

We considered two types of isolated grains boundaries with different orientations of the c-axis. The first was a symmetric tilt boundary where the c-axis is perpendicular to the applied shear. The second was a twin boundary where the c-axis is nearly parallel to the direction of applied shear. In the terminology of the coincident site lattice (CSL) scheme, these are type Σ7 [148] and Σ3 [207] orientation relationships. For the Σ7 boundary, the sample dimension perpendicular to the GB was 29.5 nm, the in-plane dimension aligned with the direction of applied shear was 8.5 nm, and the final orthogonal dimension was 2 nm. For the Σ3 boundary, the sample dimension perpendicular to the GB was 29.0 nm, the in-plane dimension aligned with the direction of applied shear was 8.4 nm, and the final orthogonal dimension was 2.2 nm. Shear was applied across the GB plane by moving two rigid end slabs of the sample relative to each other at constant velocity and in the direction of the c-axis. The direction perpendicular to the GB maintained a free surface boundary condition while the two orthogonal directions maintained periodic boundary conditions. The thickness of the rigid slabs used to apply shear was twice the inter-atomic potential cutoff distance of 8.5 Å. The samples were thermally relaxed at 300 K under zero stress for 20 ps before applying shear. Shear was applied at a strain rate of $1x10^8$ s^{-1} and the integration time step was 1 fs.

All simulations were performed using LAMMPS [1] and atomic visualization was done using OVITO [183]. Both simulations employed a Buckingham potential using parameters from Nyberg [147]. Coulombic interactions were calculated using the damped shifted force model [58] using a cutoff of 15 Å.

Nanocrystalline ZnO

For the simulated nanocrystalline sample, Figure 3.4 shows the calculated stress-strain data (black) and corresponding measured voltage (green). The inserted cross-sectional maps of the sample highlight the local changes in polarization along the compression axis (x-direction) with red and blue indicating a positive and negative change respectively. Within the elastic regime (e.g. 3% strain) we see that grains experience various magnitudes of change in polarization. These changes continue to increase even past yielding, defined by the 0.2% offset. Microstructure snapshots at 11% and 15% strain highlight this behavior.

The polycrystalline simulation highlights this unique capability of the nanocrystalline piezoelectric where the elastic deformation of nanoscale grains competes with relaxation of stress at the grain boundaries. As the polycrystalline material is pushed beyond the yielding point (~3% strain), GB motion relieves elastic stress in the structure and reduces some local polarization while other grains become activated or continue to undergo changes in polarization density. This GB plasticity is dominated by a stick-slip behavior as later shown in the isolated grain boundary simulation (Figure 3.5). This simulation supports the idea of a collective electromechanical behavior model where each grain provides some relative contribution which results in an observed net response. It is evident that some grains

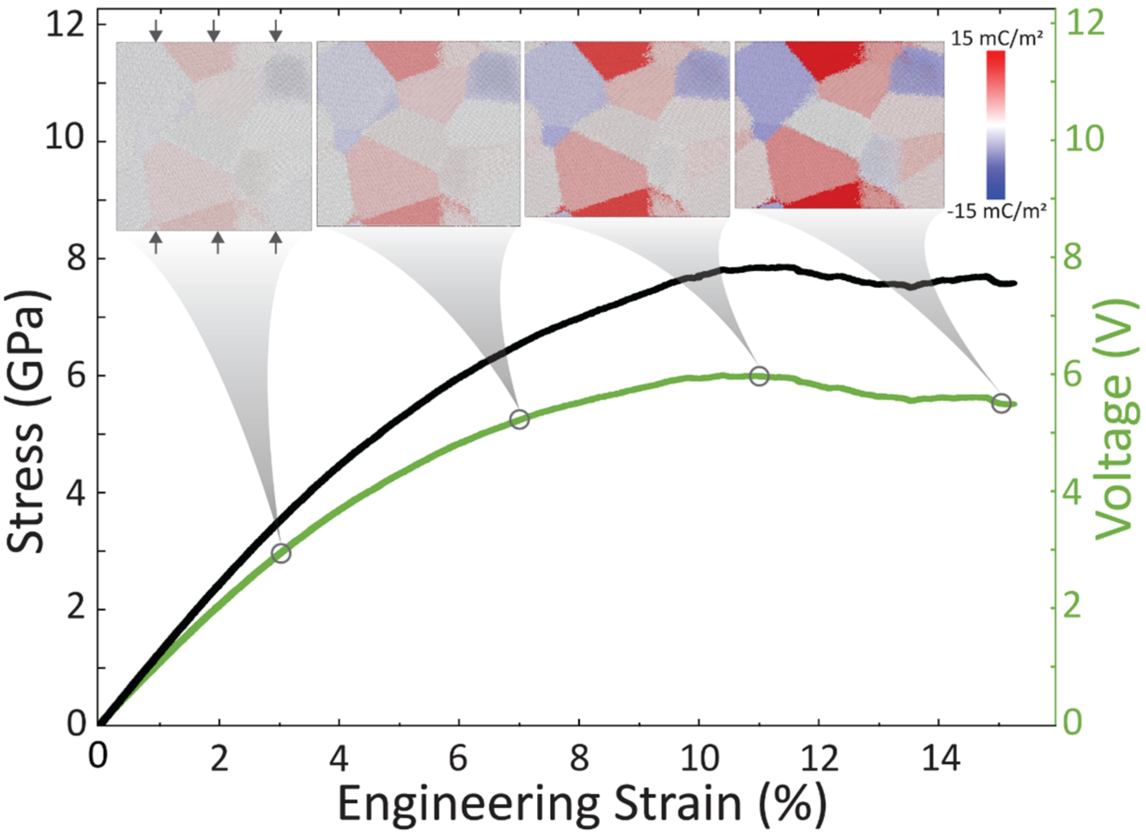

Figure 3.4: **Molecular Dynamic of Polycrystalline Zinc Oxide Electrical and Mechanical Behavior.** The mechanical (black) and electrical (green) response of a specimen with 40 grains and an average grain size of 5 nm. Snapshot images of the local polarization of grains in the structure at 3%, 7%, 11%, and 15% strain. Grey arrows indicate the direction of the applied compression.

contribute more strongly due to orientation relative to the loading direction. It should be noted that even after yielding in the material some grains are able to continue increasing their change in polarization carrying the elastic deformation. By ~10%, the material is fully dominated by GB motion and any subsequently applied stress is readily dissipated. The polycrystalline sample's mechanical signature demonstrates an averaging effect as no one local motion dominates the global response. With as few as 40 grains, the dramatic impact of a single boundary is hidden, and the mechanical response shows a collective behavior. This stands in contrast to the ~30 billion grains of similar character necessary to create a continuum-like behavior in the electromechanical response.

As shown in Figure 3.4, the interplay of local redistribution and relaxation of stress results in a voltage change that matches the stress-strain curve signature and maintains the relationship between voltage and displacement despite entering a plasticity-dominated regime of the material. This result indicates that the electromechanically coupled behavior may extend well beyond the traditional strain limitations of a single crystal ceramic and offers insight to utilizing nanocrystalline piezoelectric materials in applications beyond cyclic linear-elastic deformation.

Isolated Grain Boundary Contributions

Figure 3.5 shows the calculated stress-strain data and corresponding measured voltage for a simulated bi-crystal such that the GB is oriented with the c-axis is in-plane with the applied shear ($\Sigma3$ boundary) and perpendicular to the applied shear ($\Sigma7$ boundary). From the depicted atomic motion during deformation (Figure 3.5), the dramatic drop in stress at a near constant strain corresponds to GB slip and is characteristic of stick-slip motion. An initial GB reconfiguration occurs around 3% strain (5% strain for $\Sigma7$) and the onset of GB slip motion occurs at around 7% strain (9% strain for $\Sigma7$). Subsequent GB slip is a stochastic process. For the $\Sigma7$ boundary there is no change in voltage as the c-axis is not deformed during shear. With the $\Sigma3$ boundary, where the c-axis is in the plane of shear, changes in electric potential, and thus measured voltage, follow the mechanical behavior precisely with perfect recovery of the electromechanical behavior after GB slip events. This demonstrates the application and recover of elastic straining to the c-axis during each stick-slip event.

Looking more closely at the individual boundary contribution (Figure 3.5), the bi-crystal simulations show GB motion results in a discrete relaxation and subsequent elastic loading of the material characteristic of GB slip. The atomic snapshots taken through deformation show the stress relaxation events, i.e., GB slip, are purely a reconfiguration of existing atomic structure which takes place at the boundary. After deformation, the crystal preserves its elastic capacity and number of bond number. Thus, GB motion as shown in our MD simulation does not alter the fundamental mechanism for electromechanical coupling, and the material can recover its piezoelectric response even after a plasticity event.

This simulation also highlights the anisotropic mechanical response due to c-axis orientation. Due to the anisotropy of the wurtzite phase, grains whose orientation allows for activation of the c-axis may also deform at lower strains than those whose c-axis lie out of plane. It is critical to recognize this mechanical difference of individual piezo-active grains and grain boundaries when identifying the usable stress/strain bounds of the collective electromechanical behavior model. The model does not include post-yield relaxation of the material, and future extensions into high strain deformation of nanocrystalline materials would need to account for the specific yielding of orientated boundary orientations in addition to grain orientations. This anisotropy can also extend to framing and investigating

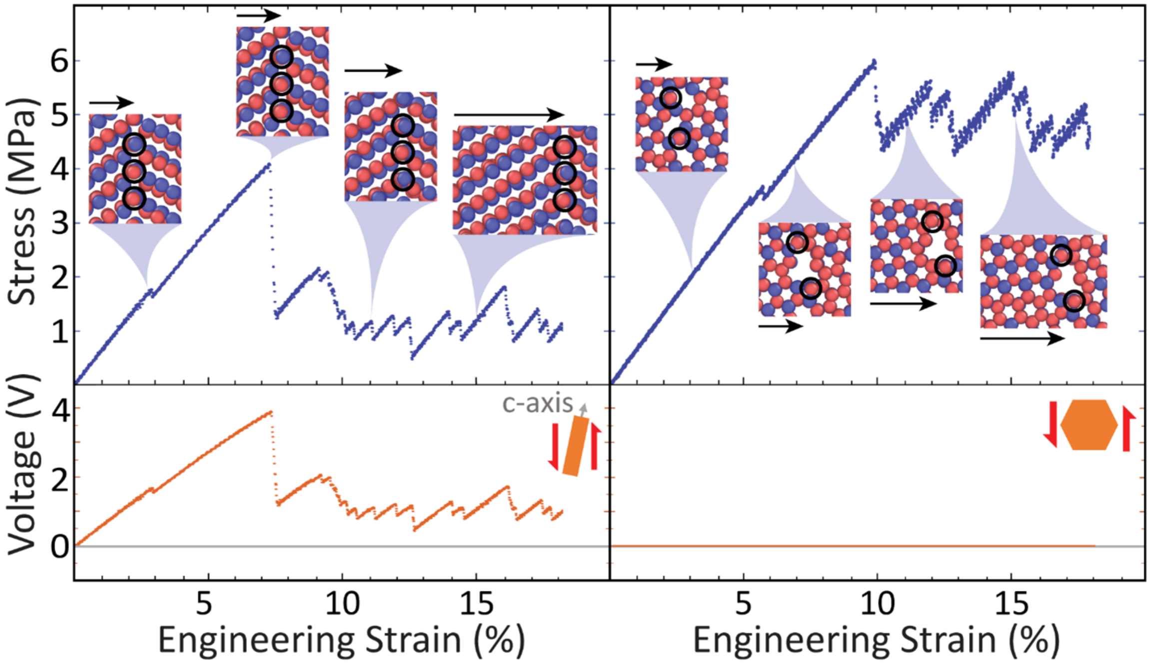

Figure 3.5: **Molecular Dynamics Simulations of Isolated Grain Boundaries.** Mechanical (blue) and electric (orange) data for shearing an isolated Σ3 boundary (left) where the c-axis lies in the plane of shear and Σ7 boundary (right) where the c-axis lies perpendicular to the plane of shear as indicated by the schematic inset. Snapshots show the progression of atomic re-arrangement at 3%, 7%, 11%, and 15% strain to highlight the atomic structure before initial reconfiguration, after the primary slip event, and throughout subsequent boundary motion. Black arrows indicate the distance of the boundary from a fixed point to highlight the boundary motion. Individual atoms along the boundary are circled and tacked to guide visualization of the atomic motion. Different coloration of the atoms in the snapshots indicate zinc (blue atoms) and oxygen (red atoms).

microstructural engineering opportunities for nanocrystalline piezoelectrics. By promoting particular types of grain boundaries or GB orientations, one could enhance or quench these discrete contributions to finite electromechanical behavior in micro-scale piezoelectric materials.

3.6 Summary and Conclusions

For nano-architected nc-ZnO, the electromechanical behavior does not stem from texturing or specific microstructural engineering but rather the absolute grain number in the structure. With our collective electromechanical behavior model, we demonstrate that millions of grains are necessary for a continuum-like behavior in randomly oriented, intrinsic piezoelectrics. This model lays the foundation to probe the shift between the continuous and discrete assumptions by setting statistical bounds of the magnitude of response and develops a method for approaching and predicting behavior of crystallographically-determined properties in polycrstyalline materials.

This study also incorporates MD simulations which shed light on the evolution of piezoelectric behavior and piezoelectric mechanisms not captured experimentally. Our work highlights the role of GB slip in the electromechanical response of nc-ZnO. This type of plasticity does not alter the polarization direction within the cyrstallite or lead to the accumulation of dislocations which can induce, greatly influence, or alter the grain's piezoelectric character. As individual grains can preserve their piezoelectric properties, the global structural response becomes a competition of localized stress accumulation and relaxation rather than frustration and immobilization of the crystal as observed in single crystal piezoelectric materials.

When evaluating emergent phenomena, it is critical to understand the relevant length scales and competing mechanisms which may be at play. This work demonstrates the need for specific analysis when determining continuum-like assumptions and illuminates key microstructural contributions to the observed piezoelectric response. From our fundamental investigation of nano-architected ZnO, we open new insights to critical microstructural engineering for integrating additively manufactured nanocrystalline piezoelectric into future generations of nanotechnology.

Chapter 4

MECHANICAL FAILURE MECHANISMS OF ADDITIVELY MANUFACTURED NANOCRYSTALLINE ZNO

This chapter has been adapted from:

Rebecca A. Gallivan, Zachary H. Aitken, Antoine Chamoun-Farah, Yong-Wei Zhang, and Julia R. Greer. Emergent mechanical and electromechanical behaviors in additively manufacture nanocrystalline zinc oxide. *Manuscript in preparation.*

R.A.G. and J.R.G. conceived of the experiments. R.A.G. synthesized samples, performed experiments, analyzed data, and formulated analytic the model and its application. A.C.-F., Z.A.H., and Y.-W.Z. generated and analyzed the isolated grain boundary simulations. Z.A.H and Y.-W.Z. generated and analyzed the polycrystalline simulations. All authors discussed the findings. R.A.G. and Z.A.H. wrote the manuscript. All authors edited and have given approval to the final version of the manuscript.

Recent development in micro- and nano-scale additive manufacturing (AM) technology has opened the material space for complex small-scale structures and demonstrated high potential for applications in nanotechnology. These AM techniques hold great promise not only in diversifying nanoscale material selection but also in harnessing mechanical size-effects such as increased yield stress [70, 75, 100, 109], brittle-to-ductile transitions [50, 231] and recoverability [93, 141]. These emergent phenomena are well documented in literature across various materials produced through deposition and focused-ion beam (FIB) milling; yet, a deficit remains in characterization of these AM materials. Investigations of nano-scale AM materials are of particular importance for compositions and microstructures not readily manufactured or explored via traditional methods of FIB-milling and electrodeposition. As technology moves towards incorporating small-scale AM into devices, it is critical to fully understand both the engineering and fundamental properties of the materials developed through these novel techniques.

One such class of materials is nano-architected metal oxides which offer an important expansion to the current array of metallic and polymeric materials for increased design capability in nanoscale devices. A recent development by Ye *et al.* [209] enables sub-micron additive manufacturing of nc-ZnO [209]. ZnO is of great interest as a structural and functional material for both its desirable manufacturing qualities (i.e., relatively abundant, cheap, biocompatible, highly stable, and easily produced) [25, 85, 151, 224] and intrinsic piezoelectricity (i.e., crystallographicly dictated electromechanical response)[1] [92]. Thus, investigating the mechanical properties at the sub-micron level is key for designing next-generation technology in sensing, micro- and nano-electromechanical (MEMS/NEMS) systems, energy harvesting, and actuating, among other applications.

Previous nanomechanical studies on ZnO has focused on nanowires [4, 6, 46, 92, 124, 179, 194, 230] with emphasis on the role of surfaces. Size effects in stiffness are observed under 100 nm which is primarily attributed to surface elasticity effects [46, 124, 179, 194] while size-based increase in fracture strength is still an ongoing investigation [92]. Polycrystalline microstructures have primarily been explored through thin films studies [36, 40, 65, 172, 206] which demonstrate classic brittle ceramic behavior and texturing. The addition of dopants can also impact the mechanical behavior through local compressive stresses [172] and a recent study by Chen *et al.* [36] provides evidence that the relatively large observed fracture strains for nanowires under tension are enabled through dislocations[2].

A deeper fundamental insight to deformation behavior in nc-ZnO is particularly intriguing for its broader implications about nanocrystalline metal oxides and ceramics. The following mechanical investigation demonstrates how these deformation mechanisms and specific microstructural features can explain the emergent failure size effect: transitioning from classic brittle behavior to a shearing event and at the smallest sizes non-catastrophic deformation. We also provide unique experimental evidence of cooperative shear band behavior in micron-sized metal oxide structures. This work highlights the unique role of nanocrystalline deformation mechanisms in electromechanically coupled behavior through MD simulations and opens new fundamental insight to these materials at the nanoscale.

All samples discussed in this chapter use the same PCS process and recipe outlined in Section 3.1 and Appendix G.1. The microstructural characterization of homogeneous, randomly oriented nano-crystalline grains on the order of 6-7 nm provided in Section 3.2 holds for these experiments as well.

---

[1] More detailed information and discussion on piezoelectricity in ZnO can be found in the introduction to Chapters 2 and 3.

[2] Further discussion of nanowire mechanical and electromechanical behavior can be found in the introduction to Chapter 2.

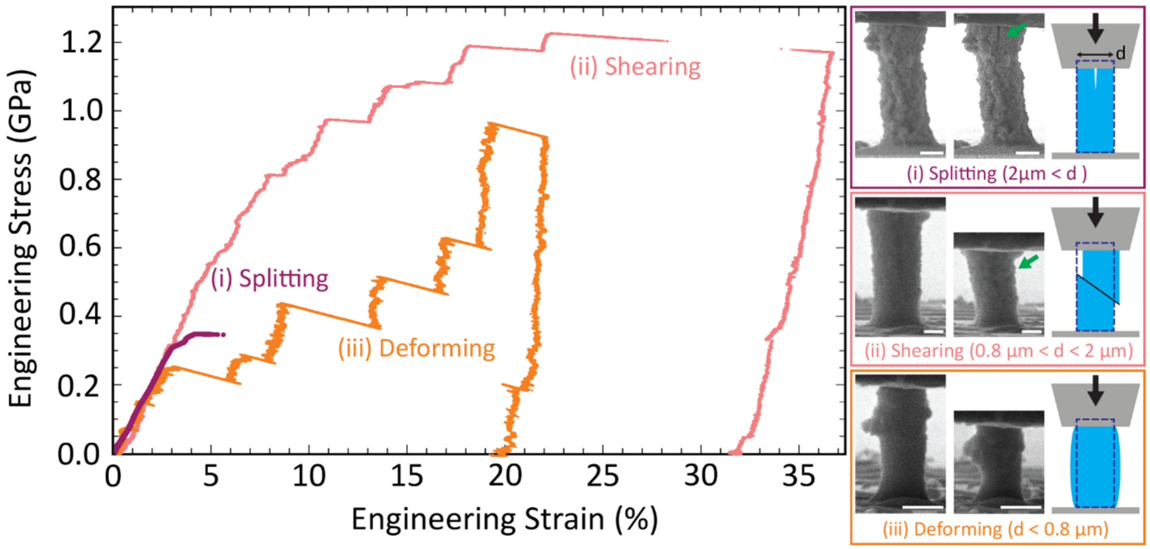

Figure 4.1: **Failure Behavior of Nanocrystalline ZnO pillars at Various Sizes.** Representative stress-strain curves for a pillar, which is greater than 2 m diameter (i; dark purple), between 0.8 – 2 m diameter (ii; orange), and less than 0.8 m diameter (iii; pink). In-situ SEM images show before and after failure initiation for each size regime and demonstrate the corresponding observed failure behavior: (i) splitting, (ii) shearing, and (iii) deforming. Graphic representation of each deformation behavior highlights differences observed in each failure regime.

4.1 Structure Size Effects on Failure Behavior

In-situ Nanomechanical Compressions

A series of experiments compressed 25 pillars to failure in a Quanta SEM (ThermoFisher Scientific) with an attached InSEM Nanomechanical Module (Nanomechanics, Inc.), enabling *in-situ* observation of the resulting mechanical behavior. Samples were compressed using a 5 µm diamond flat punch tip at a quasi-static compression rate of 10^{-3} s^{-1}. Samples with an aspect ratio between 2:1 and 3:1 were selected for compression over a range of diameters from 300 nm to 4 µm. As in Chapter 3, a compressive loading mode was chosen due to substrate adhesion and fabrication challenges associated with half-dogbone specimens typically needed for the nanotensile grip configuration.

Observed Failure Regimes

Figure 4.1 highlights the stress strain response of pillars smaller than 800 nm, between 800 nm and 2 µm, and greater than 2 µm in diameter, with a right-hand panel showing SEM and schematic representations of the corresponding observed failure behavior. For pillars larger than 2 µm in diameter, represented by line (i), the failure occurs as a catastrophic splitting event with the initiation of a crack. This behavior is consistent with the expected

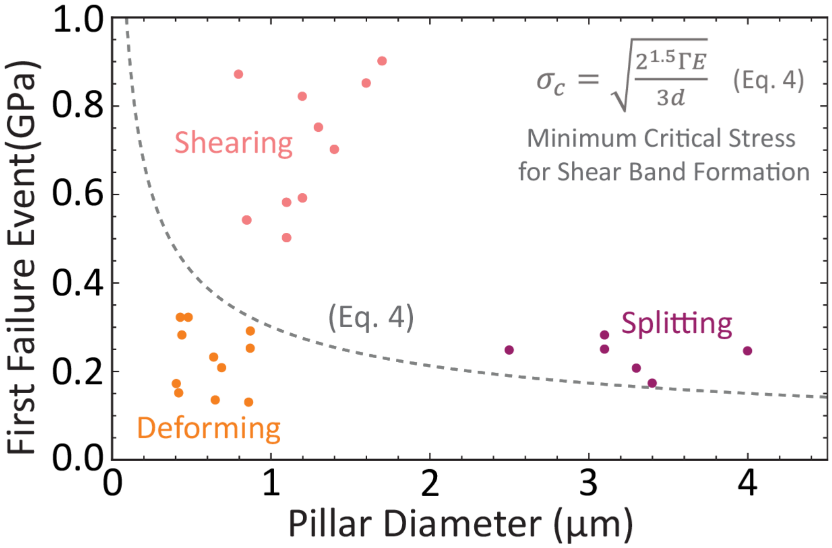

Figure 4.2: **Onset of Failure and Failure Regimes as a Function of Pillar Size.** Points are labeled with the observed failure behavior of deforming (orange), shearing (pink), and splitting (dark purple). Dotted line shows the minimum critical stress necessary for shear band formation calculated using Eq. 4.1. Failure stresses below the line are not expected to be shear band mediated.

classic elastic-brittle loading behavior found in macro-scale ZnO. In the middle size regime of 800 nm to 2 µm, represented by line (ii), pillars undergo a shearing event where a single shear surface is formed across the entirety of the pillar as seen in the *in-situ* SEM images in Figure 4.1. In pillars below 800 nm, represented by line (iii), the failure is characterized by non-catastrophic deformation of the pillar. Within the splitting regime, failure results in loss of structural integrity and there is no further loading of the pillar. For the smaller size regimes, the pillar can continue to load after the onset of failure which results in an increase in stress and subsequent burst events after the onset of failure. Burst events are characterized by sudden excursions in the strain which exceed 6 nm which is a set based on the reasonable sensitivity of our instrumentation. Downward slopes in the burst event, as seen in the smallest pillar size, are an experimental artifact, which is discussed in the literature [195].

Volkert *et al.* [192] and Jang *et al.* [94] derive the following energy balance for the critical stress necessary, σ_c, to form shear bands within the structures:

$$\sigma_c = \sqrt{\frac{2^{1.5}\Gamma E}{3d}} \tag{4.1}$$

where E is the elastic modulus of ZnO, Γ is the shear band energy per unit area, and d is the diameter of the pillar assuming a 3:1 aspect ratio as is generally observed in our structures.

(Derivation in Appendix I.) This stems from a proposed mechanism of shear band formation where the stored elastic energy must equal the energy necessary to form the plane of shear banding. The dotted line Figure 4.2 indicates the critical failure stress when applied to a nc-ZnO material system. For failure which occurs above this curve, shear-band nucleation is a possible mechanism for deformation. Below the curve, there is not sufficient stored elastic energy to nucleate a shear band in the material.

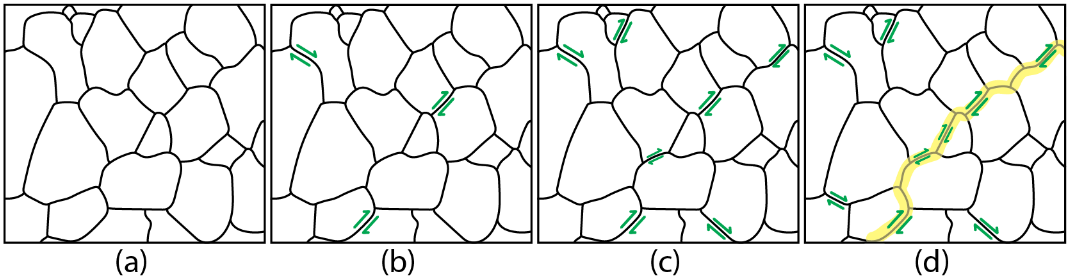

Figure 4.3: **Schematic Representation of Cooperative Shear Band Formation.** (a) The unperturbed initial grains in a nanocrystalline material. (b) Some grain boundaries are activated under an applied stress. Green arrows initiate shear along those boundaries. (c) As more stress is applied, more boundaries become active particularly until (d) a pathway forms for deformation or crack propagation forms (highlighted region) and the material collectively shears.

The size effect on failure behavior in nano-architected nc-ZnO can be described by a transition from classic brittle behavior to microstructurally driven mechanisms, particularly GB mediated deformation. The classic elastic-brittle splitting behavior seen in the largest pillars can be explained through a weakest-link model where defects in the structure act as stress concentration sites and nucleate cracks which can then be propagated through the material. As the observed failure stress is determined by the distribution of the flaw sizes within the material, we expect little variation in the observed failure stress for samples with similar flaw distribution across structure size. This behavior agrees with the observed microstructure and behavior in the pillars above 2 µm in diameter.

As pillar size is pushed to smaller extremes, the size of classic flaw sites such as pores and cracks within the structure are suppressed, and stress at the onset of failure increases. Reduced structure size also emphasizes the observed variation in failure stress as the stochastic distribution of flaws increases with decreased volume. For pillars 0.8–2.0 µm in diameter, reduction of stress-concentrating flaws may enable the dominance of a microstructural mechanism for failure. Cooperative shear band formation has previously been postulated to mediate deformation in nanocrystalline materials, though never experimentally demonstrated previously in metal oxide or micro-scale ceramic materials.

The cooperative shear band theory proposes that with applied mechanical stimulus, some grain boundaries which are aligned or have relatively lower resistance to motion will become active. Figure 4.3 provides a schematic representation of the process. As the mechanical stimulus is increased, more grain boundaries will engage in plasticity until a network of active grain boundaries is formed through the material. Thus a cooperatively formed shear band emerges as this collection of active grain boundaries enables a global deformation of the material [21, 84, 174]. The fracture surface observed after shear-off is produced by the propagation of nano-cracks which form at the points of high stress. In Figure 4.4, the clean fracture surface observed in pillars after shear-mediated failure matches the rough inter-granular fracture patterns seen in nanocrystalline metals[3].

The smallest pillars (< 800 nm diameter) display the third regime of mechanical properties, which marks a change away from singular failure points to what is characterized as a "deforming" behavior (Fig 4.1). Illustrated in Figure 4.2, the stress at initiation of failure is below the critical stress required for shear band formation. Thus the material is unable to fully initiate a cooperative shear bands and no shearing surface is observed.

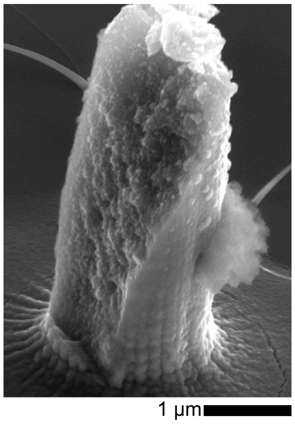

Figure 4.4: **Fracture Surface of ncZnO Pillar.** The SEM image shows the fracture surface formed at 45° to the base of the ncZnO pillar. The rough surface indicates an intergranual fracture path.

4.2 Molecular Dynamics Insights to Deformation Mechanisms

To further explain the underlying mechanisms of deformation in nc-ZnO, this section adds to the earlier discussion of MD simulations on mulit-grained nc-ZnO and isolated ZnO grain boundaries in Section 3.5. Figure 4.5 highlights the strain localization and distribution

---

[3] Generally nanocrystalline metals become brittle due to the dominance of GB plasticity of dislocation mediated plasticity and suppression of classic dislocation slip within the grains.

revealed through the MD simulations described and discussed in Section 3.5 (Figure 3.4 and 3.5). When comparing the weight-averaged von Mises strain to the applied compressive strain (Figure 4.5a), the weight average matches the strain average in grain boundaries until ~5% strain. After 5% applied strain, the weight average strain is larger than the applied compressive strain in grain boundaries. Within grains the weight average strain always remains below the applied compressive strain.

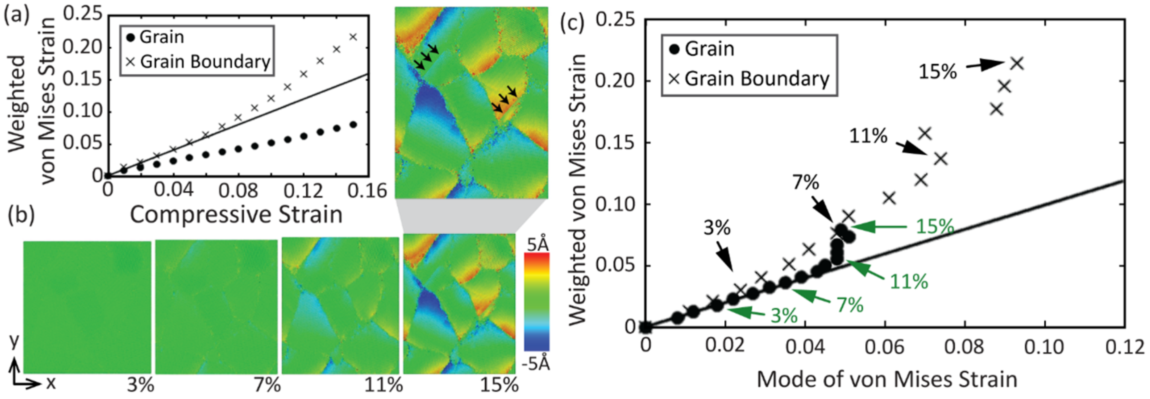

Figure 4.5: **Molecular Dynamics Analysis of Strain Localization in Grains and Grain Boundaries.** (a) Weighted von Mises strain as a function of the applied compressive strain for atoms in the grains and along the grain boundaries. (b) Strain colored snapshots of the simulated microstructure of nanocrystalline ZnO at 3%, 7%, 11%, and 15% applied compressive strain in the x direction. Enlarged view of 15% strain highlights the presence of dislocations with black arrows following the dislocation line. (c) Weighted von Mises strain as a function of the mode (i.e., peak) of von Mises strain. Points corresponding to the snapshots in (b) are labeled accordingly for atoms in grains (green text) and grain boundaries (black text) respectively.

Figure 4.5b shows the localization of strain in the simulated nc-ZnO at various points of the compression. At 3% strain distortion occurs along some grain boundaries and as strain increases, more displacement occurs along a larger fraction of the grain boundaries. At 15% strain, distortion of the lattice occurs within the grains themselves. An enlarged image of the microstructure at 15% strain reveals the presence of dislocations highlighted by black arrows.

Figure 4.5c further highlights the mechanical response of the material in showing the change in mode of the von Mises strain as a function of the von Mises strain. The points corresponding to the microstructure snapshots (Figure 4.5b) are labeled according to their applied compressive stress for clarity. When the weighted average and mode are equal, atomic strain is normally distributed throughout the population. When the weighted average is greater than the mode, some atoms experience a disproportionately large strain as compared to the rest of the population. For nc-ZnO, the GB weighted average exceeds the mode at ~3% strain and continues to increase more quickly than the mode of the von Mises strain. Atoms in the grain remain evenly distributed up to ~11% strain whereafter the weight average increases despite no change in the mode of the strain.

MD simulations highlight the dominant microstructural mechanism for deformation: grain-boundary slip. Analysis of atomic strain in Figure 4.5 shows strain is primarily carried by the grain boundaries with the applied strain matching the strain within the grain boundaries through 5% strain. Beyond this point, GB strain increases, and clear evidence of GB sliding is seen due to the sharp contrast in lateral displacement across grain boundaries (Figure 4.5b). Figure 3.5 also clearly demonstrates a stick-slip boundary sliding and highlights the relative ease with which different types of boundaries move. The $\Sigma3$ boundary begins slip around 7% strain while the $\Sigma7$ boundary does not initiation motion until ~10% strain.

As strain in the sample increases, more boundaries are activated by local shear conditions and GB motion spreads throughout the sample. This behavior is observed as early as ~3% strain with the skewing in the weighted Von Mises strain distribution (Figure 4.5c). The heavy tailed distribution of motion continues to accelerate with applied strain, indicating a heterogeneous activation of grain boundaries. As more grain boundaries become activated, a network of GB slip can form leading to global shearing behavior which aligns with our experimentally observed behavior.

We note that the MD simulations indicates that in conditions where significant deformation is achieved without the formation of nanocracks, nc-ZnO can initiate intragranular slip as demonstrated by the skewing of the von mises strain without any increase in its mode starting at 10% strain (Figure 4.5). Globally we observe a transition to easy flow at 10% strain as dislocation activity becomes an accessible mechanism for deformation (Figure 3.4).

4.3 Summary and Conclusions

Grain boundaries play a critical role in the observed failure size effect for nanoarchitechted nc-ZnO. While GB slip is known to be a dominant deformation mechanism for nanocrystalline materials in the inverse Hall-Petch regime (< 30 nm grain size)[4] [32, 73], this work experimentally demonstrates and links microstructural mechanisms to a shift from classic brittle failure to shearing to deforming behavior with reduction in pillar size. This size

---

[4] This transition assumed other stress-relief mechanisms such as large stress-concentrating voids are not readily accessed.

phenomenon can be understood through a suppression of classic brittle failure mechanisms and emergence of cooperative shearing, a GB mediated deformation mechanism. Unlike other nanoscale ceramic studies, these ZnO pillars highlight the mechanical response of nanocrystalline microstructures and grain boundary plasticity mechanisms in micron-sized structures.

From these fundamental investigations into microstructural contributions to both mechanical and electromechanical behavior in nano-architected ZnO, we demonstrate new emergent phenomena and open critical insights to their nanoscale mechanisms. Through illuminating the key considerations and parameters which dictate nanoscale material behavior, this work lays the foundation for integrating additively manufactured nanocrystalline piezoelectrics and structural ceramics into future generations of nanotechnology.

Chapter 5

CHARACTERIZING THE MICROSTRUCTURES OF CU, NI, AND CUPRONICKEL ALLOYS PRODUCED VIA HYDROGEL INFUSION ADDITIVE MANUFACTURING

This chapter has been adapted from:

Max Saccone, Rebecca A Gallivan, Kai Narita, Daryl W Yee, and Julia R Greer. Microscale fabrication of 3D multicomponent metals via hydrogel infusion. *Manuscript submitted for publication.*

M.A.S, D.W.Y, and J.R.G. conceived of and designed the experiments. M.A.S and D.W.Y designed the photoresin, printing parameters, and swelling protocol and fabricated samples. M.A.S, D.W.Y, and K.N. performed the thermal treatments and FIB/SEM/EDS experiments. M.A.S performed the DSC, TGA, and XRD experiments. R.A.G. performed the nanoindentation and EBSD experiments. All authors analyzed data and discussed the findings. M.A.S, D.W.Y, and J.R.G. wrote the manuscript. All authors edited and approved the manuscript.

Shifting from nanoscale oxides, this (and the following) chapter will focus on micro-scale metallic structures fabricated via a hydrogel enabled additive manufacturing processed called hydrogel infusion (HI) [170, 211]. Though this technique can produce a wide variety of materials including Ag, Fe, high-entropy alloys (HEAs), W, ZnO, and many other oxides, the cupronickle alloy system was chosen due to both the relatively flaw free as-printed structures observed during preliminary exploration of the technique and homogeneous alloy formation. As a new manufacturing process, characterization of the produced microstructure is critical to contextualize these materials for application and to provide insight to the role of the process on material characteristics.

5.1 Fabrication of Hydrogel Infusion Metallic Materials

HI is a new additive manufacturing technique which allows printing of various metallic materials through a nucleation, growth, and reduction process rather than the melting-based methods found in most metallic printing techniques. Figure 1.2 provides a schematic outlining the process. Initially, the desired structure is printed as an organogel using digital light processing (DPL). DPL is a form of photopolymerization where selective resin curing

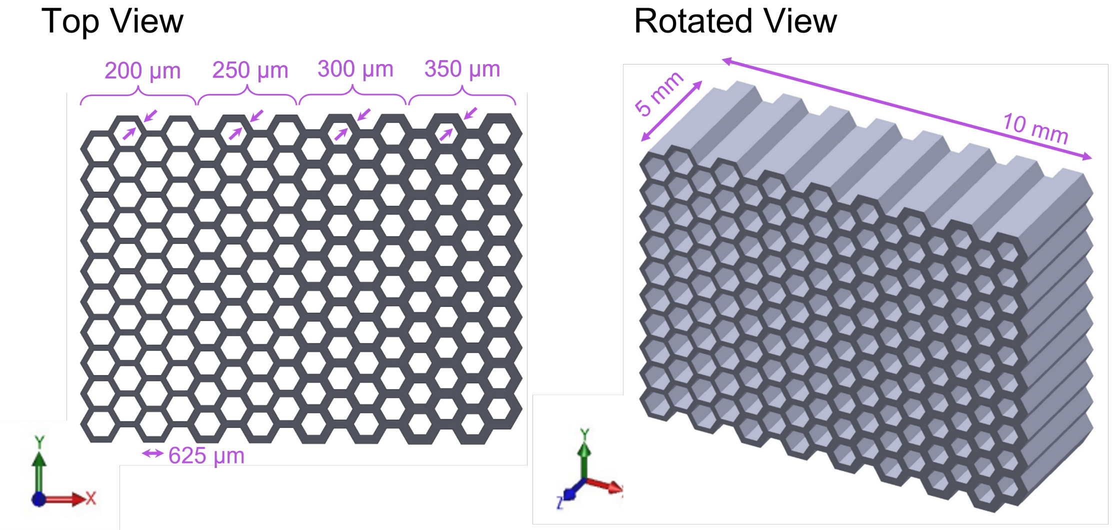

Figure 5.1: **Schematic Figures of Honeycomb Lattice.** CAD model used for printing honeycomb lattice structure and the corresponding feature dimensions. The left shows a top-down view (i.e., a view of the x-y plane); and the right shows a three-dimensional view with the z direction pointing toward the left-hand of the page.

occurs in a layer-by-layer process. This technique typically has resolution on the order of 50 µm. The initial resin composition uses an organic solvent to improve stability during the printing process. The structure's solvent is then changed to water to better incorporate the metal salts which dictate the final structure's composition. Next, metal salts are swollen into the lattice leaving a structure full of metal ions. These salts can be a mixture of various materials allowing for alloying of even high-entropy alloys. The structures are then calcined to form an oxide material. For oxides where it is thermodynamically stable, structures can be further reduced to the parent metal. This technique and its development are explained in more depth in Saccone & Gallivan *et al.* [170] as well as Yee (2020) [211]. Moving forward, the following section will provide the specific processing parameters used for generating the Cu, $Cu_{80}Ni_{20}$, $Cu_{55}Ni_{45}$, and Ni materials used in this microstructre characterization study.

First organogels are printed into 20 x 12.5 x 5 mm honeycomb lattices with a constant unit cell outer diameter of 1.25 mm (Figure 5.1). The lattice is divided into 4 sections with different wall thicknesses (200, 250, 300, and 350 µm respectively). Each section is 4 x 10 unit cells giving an entire lattice of 12 x 10 unit cells. Samples were made in a 405 nm wavelength DLP 3D printer (Autodesk Ember). Organogel resin formulation can be found in Appendix J.1. A solvent exchange is then preformed to shift the lattice structure from a DMF based gel to a hydrogel (details in Appendix J.2). The hydrogels are then swollen at 70° for 24 hours in a metal salt solution. The specific volume percentage of 2M copper nitrate hemi(petahydrate) ($Cu(NO_3)_2 \cdot 2.5\ H_2O$) and 2M nickel nitrate hexahydrate ($Ni(NO_3)_2 \cdot 6\ H_2O$) used in the solution for each composition can be found in Table 5.1.

Volume % of $Cu(NO_3)_2$ solution	Volume % of $Ni(NO_3)_2$ solution	Final Material
100	0	Cu
75	25	$Cu_{80}Ni_{20}$
50	50	$Cu_{55}Ni_{45}$
0	100	Ni

Table 5.1: **Swell-in Solution Concentrations.** The particular volumetric percentage of Cu and Ni salts used to make pure and alloyed metallic structures.

The metal ion-swelled hydrogel honeycombs are placed in and covered by alumina boats within an alumina tube (MTI, 80 cm length, 51 mm inner diameter) that itself sat inside of a larger fused quartz tube (MTI, 1 m length, 92 mm inner diameter) in a vacuum tube furnace (MTI OTF-1500X). The addition of the inner alumina tube significantly reduced the amount of SiO_2 particles observed after thermal treatment [170]. Samples are then calcined at a heating rate of 0.25 °C/min up to a maximum temperature of 700 °C. This is followed by a 3 hr isothermal hold and a cooling rate of 2 °C/min, under a compressed air flow of 50 sccm at a pressure of ~7 Torr. Samples are then reduced in forming gas at a flow rate of 150 sccm at ~22 Torr by heating at 3 °C/min to 900 °C, followed by a 6 hr isothermal hold, and cooled at 3 °C/min.[1]

For alloyed samples, energy-dispersive X-ray spectroscopy (EDS; Bruker Quantax 200, XFlash 6|60 detector) with an applied voltage of 20 kV provided confirmation of the specific composition. As seen in the resulting compositions from Table 5.1, there is a preference for Cu incorporation from swell-in to the final alloys, thus the following experiments will use the alloy compositions of $Cu_{80}Ni_{20}$ and $Cu_{55}Ni_{45}$. Other work by Saccone & Gallivan *et al.* [170] demonstrates through X-ray diffraction (XRD) that the cupronickel alloys formed via this technique are homogeneous alloys. Additionally, EDS analysis does not identify any micro-scale Cu- or Ni-rich areas but rather shows an even distribution of Cu and Ni across the structure. Figure 5.2 shows representative samples of the produced Cu, $Cu_{80}Ni_{20}$, $Cu_{55}Ni_{45}$, and Ni, as well as some other features of the as-printed materials.

---

[1] Samples were produced with the assistance of Thomas T. Tran.

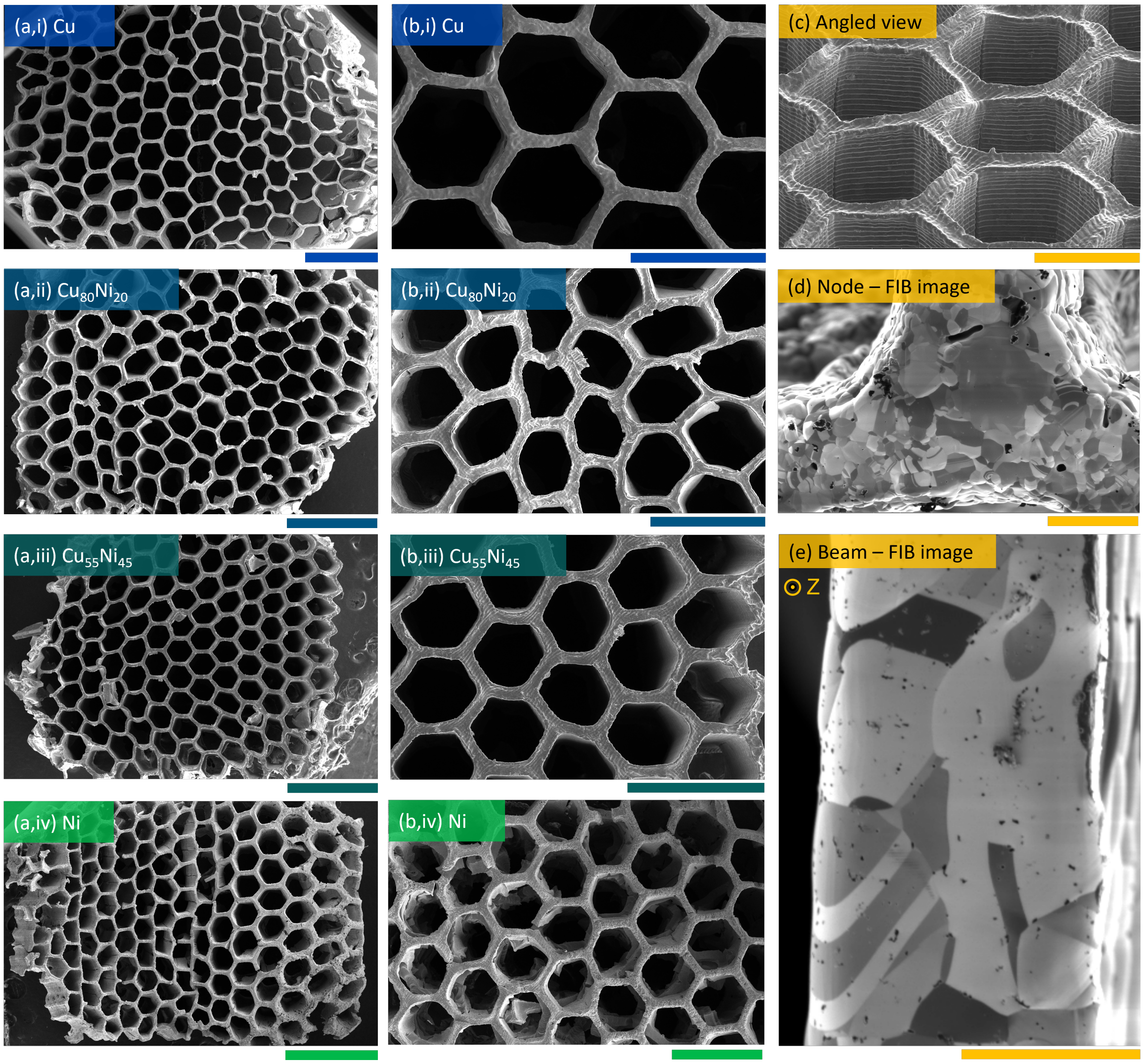

Figure 5.2: **Representative SEM Images of Hydrogel Infusion Honeycomb Lattices.** (a) Shows zoomed-out SEM images of the grids for (i) Cu, (ii) $Cu_{80}Ni_{20}$, (iii) $Cu_{55}Ni_{45}$, and (iv) Ni. (b) Zooms into the lattice structure for (i) Cu, (ii) $Cu_{80}Ni_{20}$, (iii) $Cu_{55}Ni_{45}$, and (iv) Ni to give a detailed view of the node and beam structure. (c) shows an angled view to reveal the side walls of the lattice. Focused ion beam channeling images of a (d) node and (e) beam element highlight some of the different grains and twinned regions found in those structures through contrast. All images were taken as-printed and prior to embedding in epoxy. Scale bars are (a) 1 mm, (b) 500 µm, (c) 200 µm, and (d-e) 20 µm.

5.2 Microstructural Characterization through Electron Backscatter Diffraction

To establish a baseline for the microstructural properties of these HI metals and metal alloys, EBSD mappings[2] are performed using an Oxford EBSD System in a ZEISS1550VP SEM with 20 kV and 120 µm aperture on Cu, $Cu_{80}Ni_{20}$, $Cu_{55}Ni_{45}$, and Ni samples. Kikuchi band structure analysis was done in the AztecHKL software to provide phase and orientation information across the scanned region. Mapping was performed on 3-5 different locations on 2-4 samples for each composition in order to provide a statistical basis for understanding the microstructural landscape and any heterogeneities present. This section focuses on reporting several characteristics found in HI cupronickle systems including (1) phase mapping, (2) grain characterization including size, shape, and texturing, (3) the density of various coincident site lattice (CSL) boundaries, and (4) residual strain in HI Cu, $Cu_{80}Ni_{20}$, $Cu_{55}Ni_{45}$, and Ni.

Sample Preparation

As-printed samples were mounted onto aluminum stubs using colloidal graphite to ensure good electrical contact and adhesion during mapping. These as-printed samples did not undergo polishing prior to mapping as the surface is locally smooth enough to produce good signal. As-printed samples provide information on microstructures formed at the surface of the structure; however, they technique is sensitive to macro-scale topology which can reduce the signal locally or create shadowing effects.

Additionally, through mechanical and electrical polishing, the interior structure can be explored while providing large regions smooth surfaces which can produce strong backscattered electron signal. This methodology was applied to all compositions to provide more insight to possible local heterogeneity that arises due to the printing process. Samples were first mounted into epoxy (Buehler Epoxy Cure 2) loaded with Ni powder in order to improve conductivity and minimize drift during mapping. These samples are then mechanically polished using the following scheme: a 400 grit SiC paper to expose the sample followed by a 600 grit SiC paper, and then a 1200 grit SiC paper. After mechanical polishing, the samples are electropolished (Struers LectroPol-5 with a stainless steel cathode plate) in an electrolyte solution of 54:46 vol% H_2O:$H_3(PO_4)$ (85%). A voltage of 15-20 V is applied for up to 3 seconds. Samples have variability in voltage and time to minimize grain boundary etching for each sample. Samples prepared in this way will be referred to as electropolished. Finally the epoxy-embedded electropolished samples are mounted onto Al stubs using colloidal graphite to ensure good electrical contact and adhesion during imaging.

---

[2] More information regarding this technique can be found in Appendix M.

Orientation Map Analysis Methods

Figure 5.3 provides representative EBSD orientation maps for Cu, $Cu_{80}Ni_{20}$, $Cu_{55}Ni_{45}$, and Ni samples where the crystallographic orientation is denoted by a specific color. Maps discussed in this chapter generally have pixel sizes of 200 nm and thus features smaller than 200 nm are not detected. These maps have had minimal post-processing, only removing isolated pixels which are not associated with the overall pattern and filling in pixels whose nearest neighbors all have the same orientation. This minor extrapolation and cleaning of the EBDS maps helps the processing software, Tango (HKL Channel 5), better identify grains and boundaries in the maps. All reported values of grain size, boundary misorientation angle, and all specific CSL labeling are generated by the software. To be counted as a grain, the region must contain at least 3 pixels of the same orientation. This threshold helps to ensure that the pixels represent a region rather than noise. Additionally, Σ3 (otherwise known as twin) boundaries are ignored for the purpose of identifying grain boundaries and thus are included as part of the region considered to be a grain.

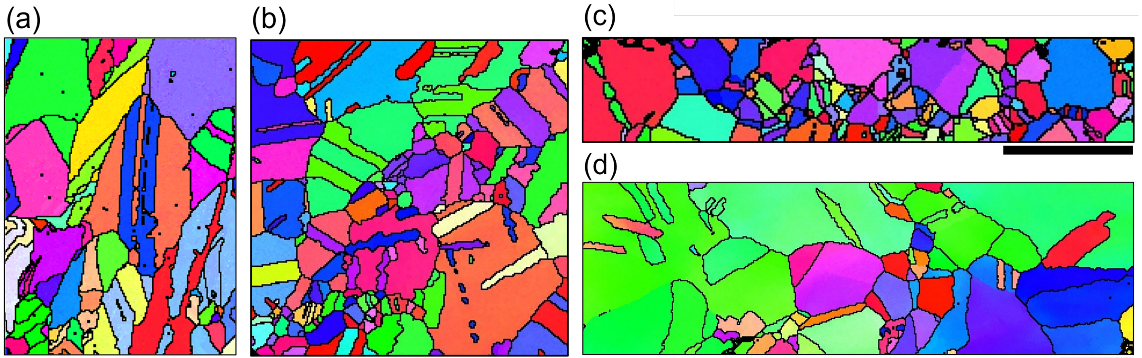

Figure 5.3: **Representative EBSD for Cu, $Cu_{80}Ni_{20}$, $Cu_{55}Ni_{45}$, and Ni**. The EBSD mapping shows crystal orientation along the z-axis of the lattice for (a) Cu, (b) $Cu_{80}Ni_{20}$, (c) $Cu_{55}Ni_{45}$, and (d) Ni samples with boundaries between orientation regions outlined in black for visual ease. All scale bars are 10 µm. Coloring scheme follows the standard EBSD pole mapping with red as <001>, green as <101> and blue as <111>. See Appendix M.2 for a large legend.

Finally, dislocations densities can be estimated from EBDS maps when there are high densities of GNDs. This is due to the shifts in orientation or strain in the material which leads to a rainbowing or ombre effect in the pole map.

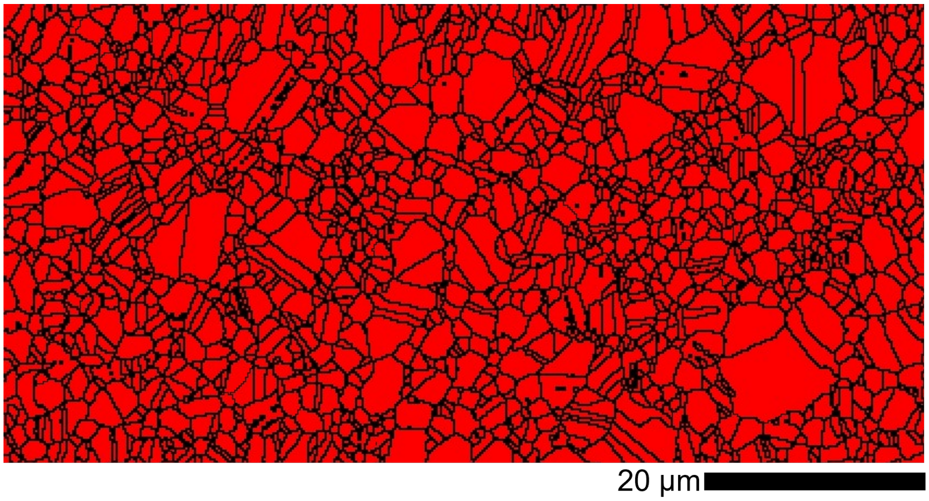

Figure 5.4: **Crystal Phase Mapping from EBSD of Representative Cupronickel Alloy.** The image shows the regions where the material has a FCC crystal phase in red. Boundaries of orientation are outlined in black to visually guide the eye with regards to the microstructure.

Phase Mapping

Figure 5.4 highlights a representative phase mapping where different colors indicate different crystalline structure. In the figure only one color (red) is present as only an FCC phase is detected. All of the investigated materials are purely FCC phase for both as-printed and electropolished and contain no detected regions of oxide or other metallic phases. This matches the XRD analysis performed in Saccone & Gallivan *et al.* [170] and demonstrates complete reduction of the oxides throughout the structure.

Grain Size Distribution

Grain size distribution generally follows a lognormal distribution as seen in Figure 5.5 which shows histograms of the grain sizes for Cu, $Cu_{80}Ni_{20}$, $Cu_{55}Ni_{45}$, and Ni. The distributions in Figure 5.5 highlight a general consistency of grain sizes across composition with mean grain sizes of 2-5 μm and mode grain sizes of 1-1.5 μm. The most notably different feature is the relatively small tail in $Cu_{55}Ni_{45}$, indicating a reduced presence of large grains. The standard error of the mean is reported[3] in Figure 5.5 and provides confidence in the reported mean for the sampled distribution. There is no observed difference in grain size for nodes of

---

[3] Standard error is chosen here as it indicates the confidence in measurement of the mean, and its calculation is applicable to any type of distribution. Standard deviation on the other hand is most meaningful when looking at normal distributions and thus could provide a misleading picture of grain distribution when directly applied to these histograms.

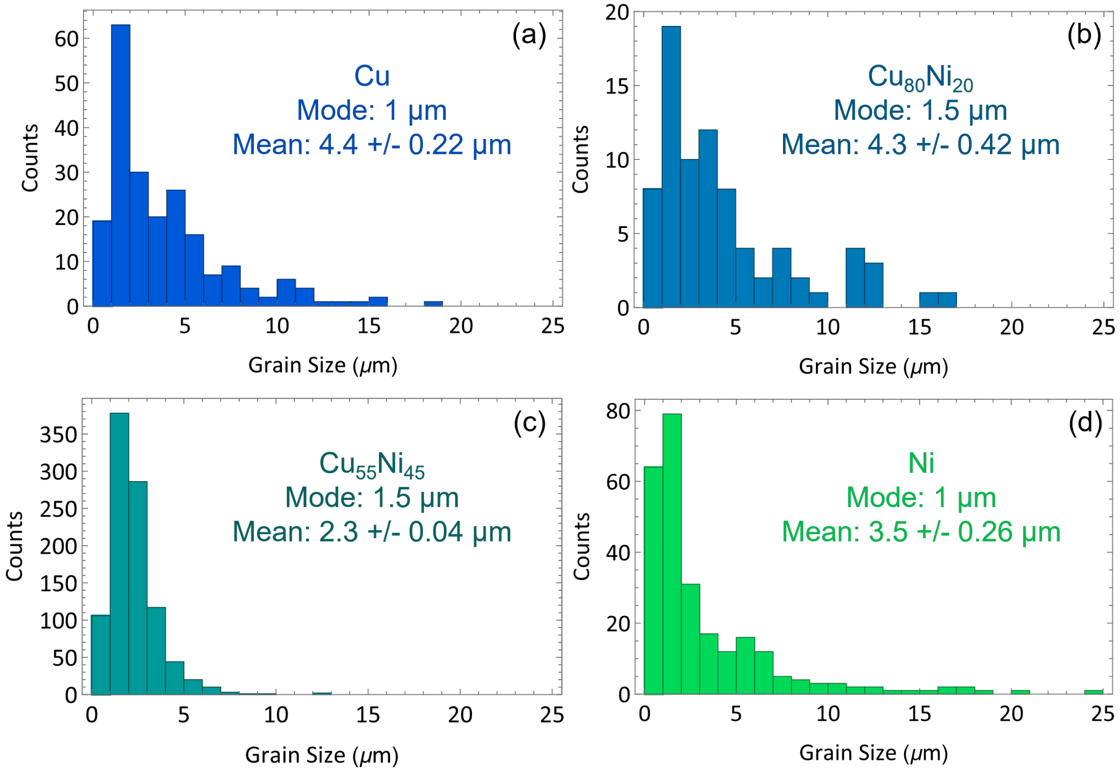

Figure 5.5: **Histograms of Grain Size Distribution.** Distributions shown for (a) Cu, (b) $Cu_{80}Ni_{20}$, (c) $Cu_{55}Ni_{45}$, and (d) Ni with the mode and mean reported in each respective subfigure.

the lattice as compared to the beams or for as-printed structures compared to electropolished samples.

Some EBDS analysis conducted in early stages of this work used as-printed octet lattices rather than honeycomb structures. Spacial trends in grain size were observed for the octet lattice structures. Specifically, the beam regions had smaller grain sizes as compared to nodes with a 13% and 31% decrease in grain size for Cu and CuNi[4] respectively. This local inhomogeneity likely stems from the geometric confinement or different local kinetics in the beams which were often half the width of the node.

Texturing

Using the software Mambo (HKL Channel 5), pole and inverse-pole figures can be generated to understand the distribution of grain orientations and identify and patterns of texturing or preferential grain orientation. Pole figure maps show the x-y-z direction of a particular crys-

---

[4] These results were taken for a $Cu_{50}Ni_{50}$ in Ref [170] which differs from the alloy compositions used in the work reported for this thesis.

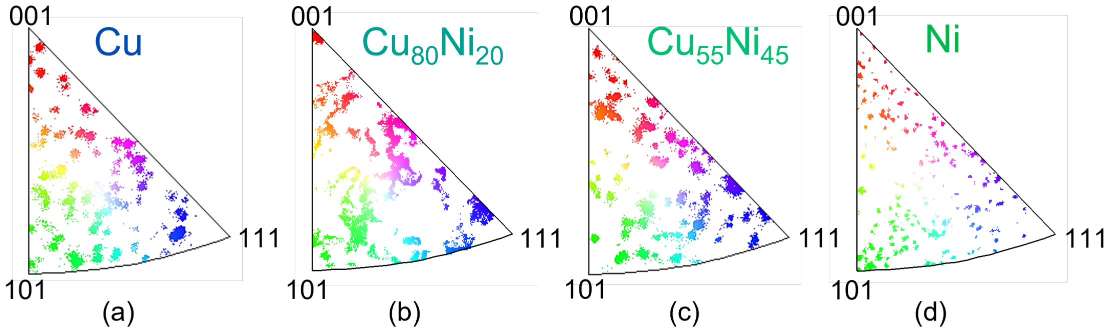

Figure 5.6: **Inverse Pole Figures for HI Metals.** Inverse pole figures for (a) Cu, (b) $Cu_{80}Ni_{20}$, (c) $Cu_{55}Ni_{45}$, and (d) Ni along the z axis show no texturing and even distribution of grain orientations across the whole crystallographic space.

tal orientation while inverse-pole figures simply display all the crystallographic orientations present along a particular direction. Figure 5.6 shows a representative inverse-pole figures along the z axis which matches the build direction during the DLP printing. No texturing is observed for any composition. We also see no clustering in the x and y directions which represent the general in-plane orientation of the structure (Appendix Figure K.1).

Grain Shape

Grains are found to be generally equiaxed across all compositions with the average aspect ratio[5] between 1.5 and 2.2 (see Table 5.2). This is well below the typical aspect ratio of 3+ found in columnar grain structures [20]. EBSD maps of the normal (Figure 5.7a) and cross-sectioned[6] (Figure 5.7b) surface show no change in the general grain shape.

Material	Aspect Ratio
Cu	2.1 +/- 0.37
$Cu_{80}Ni_{20}$	1.6 +/- 0.1
$Cu_{55}Ni_{45}$	1.7 +/- 0.09
Ni	2.0 +/- 0.03

Table 5.2: **Grain Shape.** The aspect ratio of the major to minor axis in the elliptical approximation of the grain for all compositions.

---

[5] Aspect ration here denotes the ratio of the major axis of the ellipsoid approximation for the grain, a, divided by the minor axis of the ellipsoid approximation, b.

[6] The cross-section honeycomb surface exposes the walls of the structure. This surface is perpendicular to the polished surface outlined in Section 5.2.

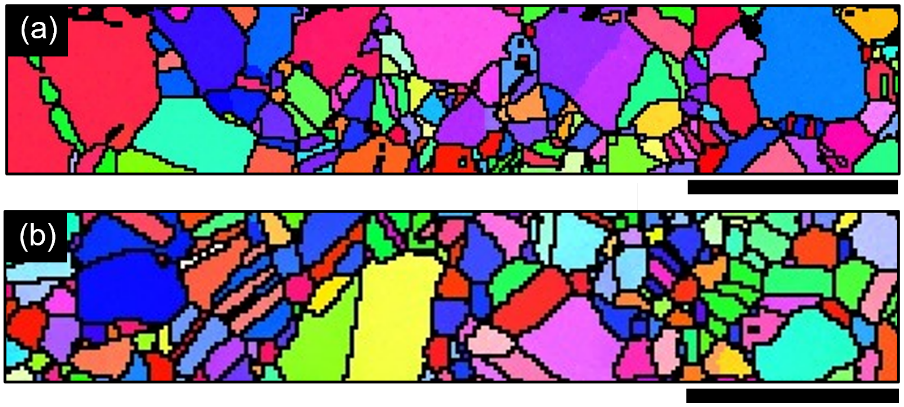

Figure 5.7: **Comparison of Grain Shape.** Grains are shown to be similarly shaped and not forming any columnar morphologies in the (a) normal (x-y plane) and (b) cross-sectional (parallel to z plane) surfaces. All scale bars are 10 µm.

Twin and other CSL Boundaries

CSL boundaries are special types of boundaries discussed in the Introduction (Section 1.3). This section will focus on describing the twin and other CSL boundary characteristics of these HI Cu, $Cu_{80}Ni_{20}$, $Cu_{55}Ni_{45}$, and Ni through line densities, number densities, and other metrics. It is important to note that materials with low stacking fault energies (SFE) have a greater propensity for twin. The SFE of Cu and Ni has been measured as 55 mJ/m^2 [61] and 130 mJ/m^2 [33] respectively. Literature on the SFE for cupronickel alloys reports a variety of values and trends, from linear mixing between Cu and Ni to relatively similar SFE values until Ni-rich alloy compositions where it rapidly increases [130].

Material	% Grains Twinned	Average # Twin per grain
Cu	88 +/- 9%	5.7 +/- 0.20
$Cu_{80}Ni_{20}$	89 +/- 5%	4.3 +/- 0.41
$Cu_{55}Ni_{45}$	75 +/- 13%	3.9 +/- 0.81
Ni	83 +/- 7%	3.6 +/- 0.11

Table 5.3: **Twin Prevalence in Cu, $Cu_{80}Ni_{20}$, $Cu_{55}Ni_{45}$, and Ni.** Average values and standard deviation of grains containing at least one twin and the number of twins found in a grain.

No variation was seen by location or between as-printed and electropolished so the reported values in this section are representative of all samples. Table 5.3 outlines the prevalence of these boundaries within the materials. Generally, the twins are fairly well distributed with >75% of grains containing at least one Σ3 boundary for all compositions. The average number of twin boundaries within a grain increases as we increase the percentage of Cu present, which follows the intuitions from stacking fault energies. It is important to note that

Material	Twin Line Density (µm/µm^2)	Twin # Density (1/µm^2)
Cu	1.9 +/- 0.31	0.75 +/- 0.12
$Cu_{80}Ni_{20}$	2.0 +/- 0.35	0.82 +/- 0.03
$Cu_{55}Ni_{45}$	1.6 +/- 0.43	0.54 +/- 0.20
Ni	1.8 +/- 0.17	0.34 +/- 0.03

Table 5.4: **Twin Densities in Cu, $Cu_{80}Ni_{20}$, $Cu_{55}Ni_{45}$, and Ni.** Average values and standard deviation of twin line length and number density. Eq. 5.1 shows how twin line density is calculated.

$Cu_{55}Ni_{45}$ samples show significantly more variation in both percentage of twinned grains and average number of twins per grain. Though possibly an anomaly of the processing, another hypothesis is that this variance arises from some kinetic competition between CuO and NiO during reduction that leads to more localized regions of Cu-like and Ni-like ability for twin formation. However, greater investigation into the growth and reduction of the system is needed to fully address the distinct behavior of $Cu_{55}Ni_{45}$. No correlation was found between grain size and boundary presence.

To further contextualize the presence of twins, we turn to measurements of density. Twin boundary line density (ρ_{line}) is calculated as:

$$\rho_{length} = \frac{\Sigma_{i=1}^{N} l_i}{A} \tag{5.1}$$

where l_i is the boundary line length for a particular boundary and N enumerates all the boundaries present within a given area, A. Another important consideration is the number of boundaries present. Mechanistically, one long boundary presents a different landscape than two short boundaries as each boundary acts as its own energetic barrier to dislocation motion. Boundary number density (ρ_{number}) is defined as:

$$\rho_{number} = \frac{N}{A} \tag{5.2}$$

While the expected density of twin boundaries is material and process dependent, line density values above 1x10^6 m^{-1} are universally considered highly twinned [11]. No general metric for high twin number density was found in the literature.

Table 5.4 highlights the values of both line and number densities for all compositions. The line density does not have a strong compositional trend. All materials are well described with average line densities of 1.6-2.0 µm^{-1}. However, number density does show a strong trend of increased twin density with increase Cu composition. In the measured densities, $Cu_{55}Ni_{45}$ sees the large variation as seen in earlier metrics.

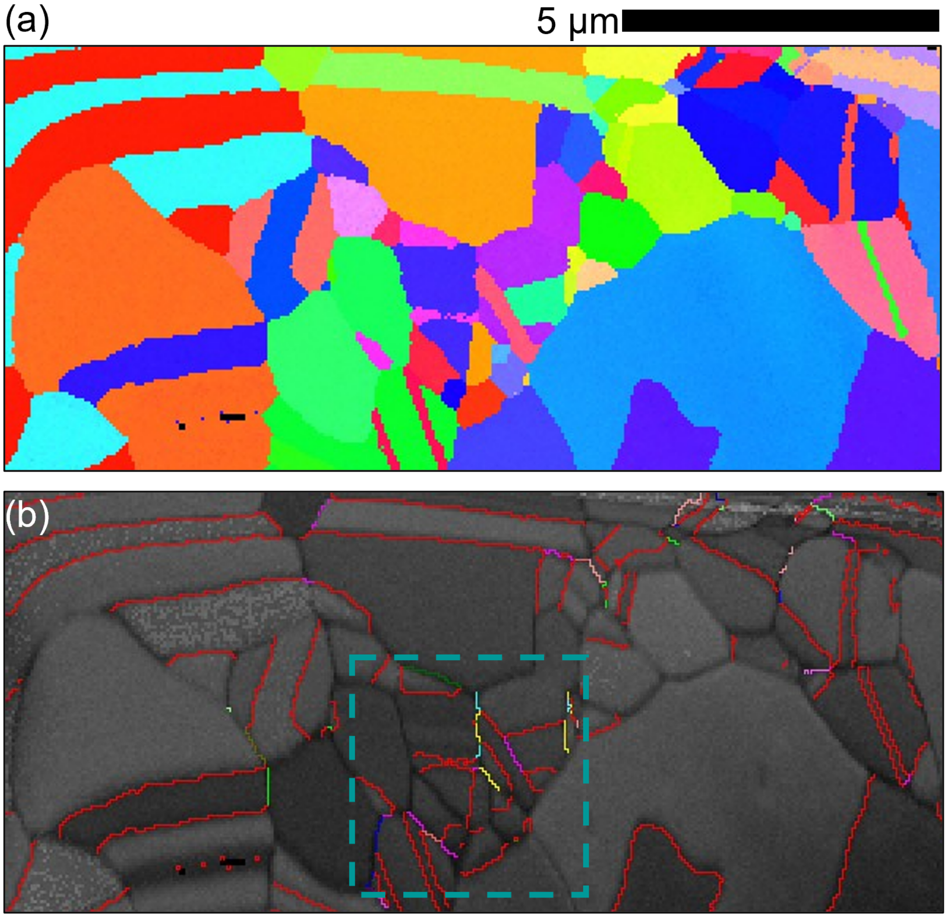

Figure 5.8: **Highlighting CSL Boundary Clusters**. Representative EBSD map from $Cu_{80}Ni_{20}$ showing (a) crystal orientation and (b) band contrast maps. CSL boundaries are highlighted on the band contrast map with red for $\Sigma3$, green for $\Sigma5$, pink for Σ 9, and yellow for Σ 11. The dashed teal box highlights a region of clustered higher order CSL boundaries in contrast to the ubiquitous distribution of twin ($\Sigma3$) boundaries.

Other CSL boundaries appear in far more clustered structures as shown in Figure 5.8 and do not show clear compositions trends. It should be noted that Cu and Ni have different energetically favorable boundary types [222] that make direct cross-comparison challenging. However, the grain boundary energy associated with higher order CSL boundaries is similar within a particular material making the comparison between twin and CSL boundaries as a group reasonable for a particular material. Thus moving forward we will address non $\Sigma3$ CSL boundaries as a singular class rather than enumerate the specific contributions of each boundary type.

Table 5.5 shows the average percentage of CSL boundaries which are not $\Sigma3$ type boundaries for a representative site. While the average contribution from CSL boundaries across

Material	% of CSL boundaries that are not $\Sigma 3$
Cu	14 +/- 3.6
$Cu_{80}Ni_{20}$	14 +/- 2.1
$Cu_{55}Ni_{45}$	14 +/- 8.9
Ni	13 +/- 3.2

Table 5.5: **Non $\Sigma 3$ CSL Boundaries Percentage.** The average portion and standard deviation by site of all CSL boundaries which are high order (i.e., not $\Sigma 3$) boundaries.

compositions remains consistent, the variation is high due to the clustering of these boundaries.

Summarily, we observe universally high twin line densities with no trend in composition. In contrast twin number densities generally increase with increased Cu composition. This implies that twin boundaries are longer in compositions with higher Ni concentration. Other higher order CSL boundaries make up approximately 14% of the CSL boundaries present in these HI materials independent of composition.

Residual Strain and Dislocation Densities

No residual strains are observed in any of sites mapped through EBSD. As mentioned earlier this would manifest as a rainbow-like gradient due to shifts in the lattice from that strain. While some small regions not captured in these maps may locally have high dislocation densities or strained grains, HI metals can generally be thought of as displaying similar microstructures to well-annealed Cu which has been traditionally processed.

5.3 Microstructural Characterization through TEM

Sample Preparation

A lamellae of thicknesses <100 nm is prepared for liftout from an as-printed structure thorugh the following procedure. The top surface of a beam region in Cu is protected with a 100 nm thick layer of platinum (Pt) deposited via a Gas Injection System (GIS) using an electron beam in an FEI Versa DualBeam SEM followed by a ~400 nm thick layer of Ga+ FIB-deposited Pt in the same chamber. Next, a Ga+ ion beam is used to carve out a J-cut of the material so that the lamella is only attached by a small bridge to the rest of the substrate. The lamella is attached to a tungsten needle (EZlift program) through FIB-deposited Pt before being detatched from the samples and transfered to a copper halfmoon grid. The sample is then glued via FIB-deposited Pt to the grid. After detaching the tungsten needle, a series of cuts are made with a decreasing Ga+ voltage/current (30 kV, 100 pA; 30 kV, 10 pA; 16 kV 23 pA). These cutrs are used to progressively thin the cross-section of the bundle

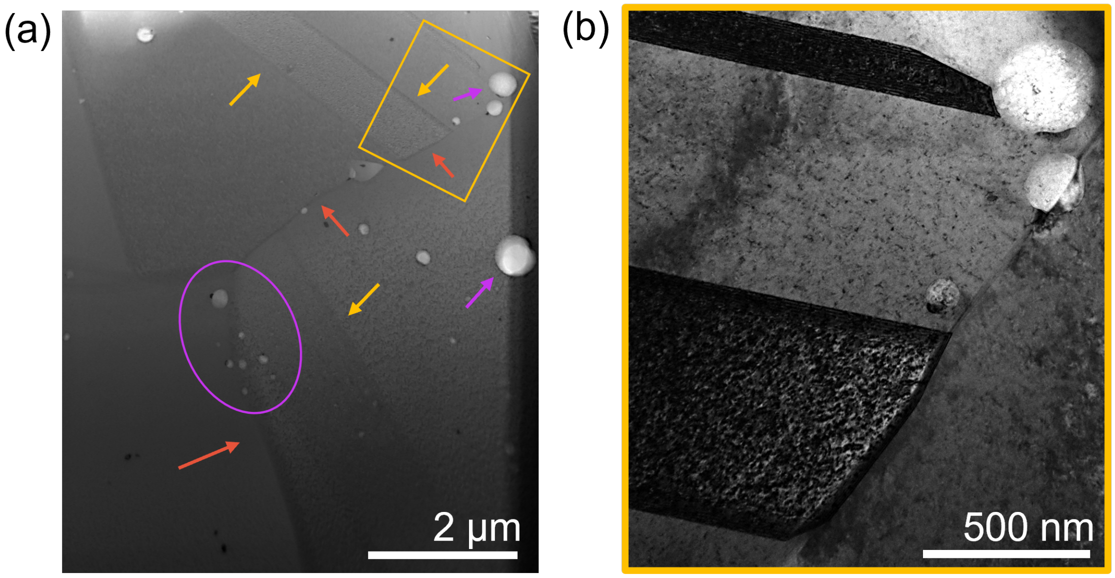

Figure 5.9: **TEM Micrograph of Hydrogel Infusion Produced Cu.** (a) Overview image of region shows the presence of twinned regions on the order of ~100 nm (orange arrows), well formed grain boundaries (red arrows), and nanoscale inclusions (purple arrows and circle). (b) The zoomed in section highlights these three features.

structure to <100 nm. The TEM images are taken in a Jeol JEM-2800 TEM with a 200kV beam.

Observed Microstructure

TEM analysis of HI-derived Cu shows twins and grain boundaries in more detail than observed in EBSD (Figure 5.9). We observe that grain boundaries and twin boundaries are well-formed, with no voids at triple junctions. Additionally, there do not appear to be any observable secondary phases (i.e., unreduced CuO or amorphous carbon) besides the small aluminosilicate inclusions. EDS shown in Figure 5.10 confirms composition of these inclusions which are a contaminate from the mullite furnace tube used during calcining and reduction. These aluminosilicate particles range from 50 nm to 1 µm in size and are not homogeneously distributed throughout the sample. They appear at various depths away from the surface indicating that they may have been incorporated into the hydrogel lattice before calcining. Finally there does not appear to be any evidence for unusually high dislocation densities. This matches with a lack of residual strain observed in EBSD for Cu samples.

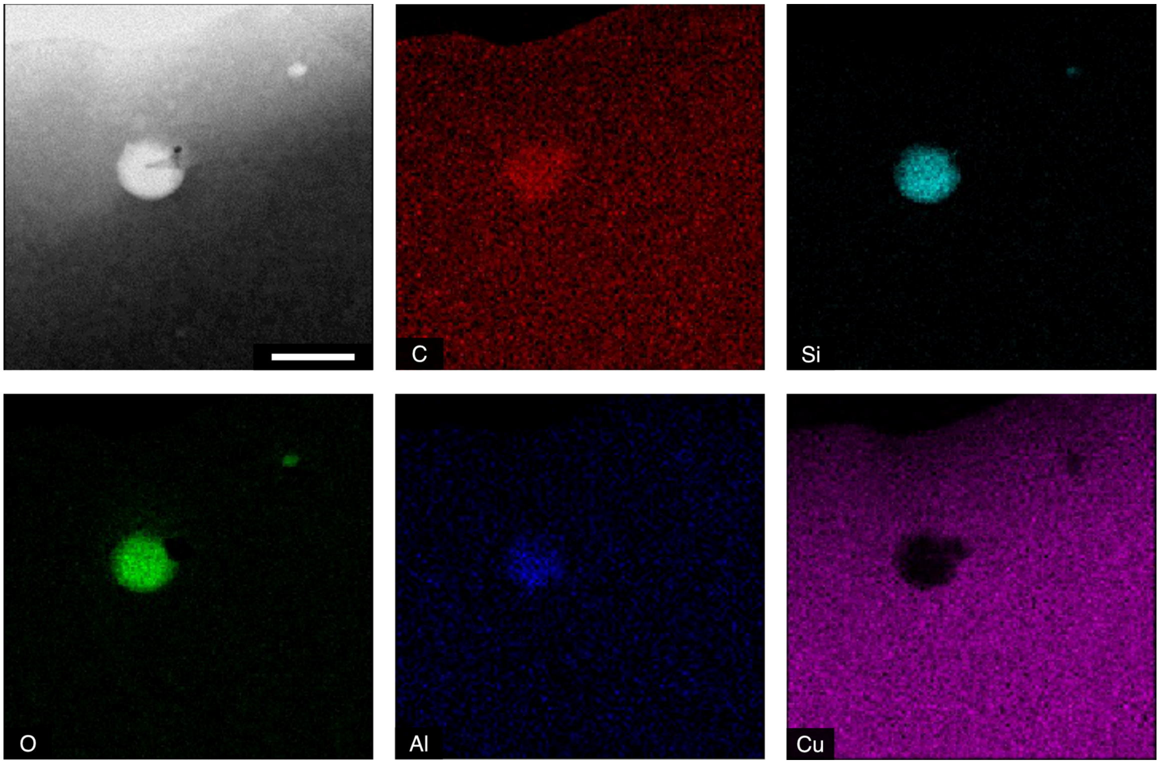

Figure 5.10: **High-Resolution EDS Mapping of Aluminosilicate Particle in HI Cu.** (a) The TEM micrograph showing the particle analyzed through high-resolution EDS mapping. Intensity of coloring shows the relative presence of (b) C, (c) Si, (d) O, (e) Al, and (f) Cu.

Discussion on Carbon Inclusion

As a light element, carbon is notoriously difficult to quantify in trace amounts, particularly when dissolved into a host lattice as opposed to forming a precipitate or complex. While some literature indicates that metastable carbon solid-solutions can be formed with Cu, this phase is typically produced under high pressure processing (e.g. ball milling) [125] and in small atomic % of carbon making identification particularly challenging. Additionally, it is difficult to prove the absence of something, particularly with techniques such as TEM, which make statistical sampling even more challenging. Though there is no evidence for carbon precipitates, amorphous carbon inclusions, or complexions along the grain boundary, we cannot claim there is no carbon present in these materials. Particularly along high-angle grain boundaries and high-index CSL boundaries, there are opportunities for small amounts of carbon to remain trapped or dissolved that would not be visible without careful HRTEM investigations. Given the high carbon content during processing, it is likely that some carbon remains either dissolved or as extremely small particles; however, it is unclear if these materials contain a critical concentration of carbon necessary to contribute meaningful changes to the material’s properties.

5.4 Summary and Conclusions

Lack of texturing, significant residual strain, or high dislocation densities, equiaxed grain shape, and the general well-annealed microstructure of these HI metals stands in contrast to many of the additively manufactured metals produced through melting based techniques. The microscopic view of the grain structure in HI metals demonstrates a uniquely normal microstructure. However, the presence of a high density of annealing twins in the absence of recrystallization processes hints at a farther from equilibrium behavior than otherwise anticipated. These high line densities, most commonly seen in complex alloys or under extreme processing conditions, are material agnostic, which stands against the general intutition from SFE. Stable incoherent twin boundaries are also present in these materials and further demonstrate the microstructural complexity found in these as-printed metals.

For a more complete understanding of this new process, a deeper investigation into the nanoscopic and atomic-level structuring along grain boundaries is key. Additionally, annealing studies and exploration of the kinetic processes during nucleation, growth, and reduction are important next steps to opening our understanding of these processes and the microstructures one can produce from it. In fundamentally exploring the nucleation and diffusion mechanisms at play in this process, we can better shed light on the origin of far-from-equilibrium microstructures and open numerous possibilities for advanced defect and boundary engineering.

Chapter 6

INSIGHTS TO MICROSTRUCTURE-MECHANICS RELATIONSHIPS IN HYDROGEL INFUSION ADDITIVELY MANUFACTURED CU, NI, AND CUPRONICKEL ALLOYS

This chapter has been adapted from:

Max Saccone, Rebecca A Gallivan, Kai Narita, Daryl W Yee, and Julia R Greer. Microscale fabrication of 3D multicomponent metals via hydrogel infusion. *Manuscript submitted for publication.to*

M.A.S, D.W.Y, and J.R.G. conceived of and designed the experiments. M.A.S and D.W.Y designed the photoresin, printing parameters, and swelling protocol and fabricated samples. M.A.S, D.W.Y, and K.N. performed the thermal treatments and FIB/SEM/EDS experiments. M.A.S performed the DSC, TGA, and XRD experiments. R.A.G. performed the nanoindentation and EBSD experiments. All authors analyzed data and discussed the findings. M.A.S, D.W.Y, and J.R.G. wrote the manuscript. All authors edited and approved the manuscript.

It is well known that microstructure explains much of the mechanical behavior of materials[1]. As new manufacturing techniques often shift the microstructural landscape, it is particularly important to link the mechanical and microstructural properties to fully understand key engineering opportunities and limitations. Building from the microstructural analysis in Chapter 5, nanoindentation is used to probe the hardness of Cu, $Cu_{80}Ni_{20}$, $Cu_{55}Ni_{45}$, and Ni metals made through HI. As Cu, Ni, and cupronickel alloys have been previously studied via indentation [12, 15, 35, 53, 193], these experiments help to form a baseline for the relative performance of HI metals.

6.1 Nanoindentation

Samples were prepared for nanoindentation by mounting the honeycomb lattice in epoxy (Buehler Epoxy Cure 2) and letting the epoxy cure for 12 hours in silicone molds. The honeycomb lattices are the same preparation and structure as dsicussed in Section 5.1. The samples were polished to expose the honeycomb structure first with 400 grit SiC paper before smoothing the surface with 600 grit SiC paper, 1200 grit SiC paper, and then a 0.25

---

[1] It also explains material behavior more generally including electrical, optical, etc.

µm grit suspension (Beuhler MetaDi Polycrystalline Diamond Slurry). Indentation was performed on an Agilent G200 Nano Indenter with XP module using a Berkovich tip with an area function given by:

$$A(h) = 24.5h^2 + 364.982h - 1701.69h^{1/2} + 1079.23h^{1/4} \tag{6.1}$$

where h is the indentation depth and A(h) is the contact area of the tip[2]. Samples were indented at 10^{-3} strain rate to a maximum depth of 500 nm, followed by a 2 s hold and subsequent unloading. The indentation regions were selected in relatively pore-free areas and indentation sites were least 10 µm away from the any edge or other indentation site to ensure no interaction from previous tests or boundaries. For statistical robustness, each sample contained at least 20 valid indentation tests with most samples containing 60-300 valid indentations.

All hardness data reported is taken as an average hardness from 300-500 nm as no trend in hardness was found with depth within this range. Initial instabilities or non-physical calculations of hardness are due to break downs in the area function where the tip is not perfectly sharp, or minor surface variation may impact the calculated hardness. Based on the calibration of the system and the observed data, accuracy of the hardness calculation occurs well before 300nm. However, the choice of a 300-500 nm range ensures measurements are taken well into the indentations. By measuring the hardness as an average across this range, we ensure the measurements are minimally subjected to noise.

6.2 Hardness in Hydrogel Infusion Cupronickel Systems

In many additively manufactured metals, location within a structure can influence the material property due to microstructural variations which arise from boundary or kinetically driven effects of the printing path. To test if there are spacial shifts in mechanical properties, indentations are taken across a variety of sites in both the node and beam region of the honeycomb lattice. Table 6.1 shows the difference in measured hardness between the beam and node regions for a representative sample of each composition. The difference in the mean hardness by region is less than the standard deviation of the hardness measured in those regions. Thus, no statistically significant variation is observed between these structural features and the following mechanical analysis will only label composition.

For each composition, 3 different samples were measured to understand the difference between hardness variation within a sample as compared to the process variation sample-to-sample. Figure 6.1 shows the mean hardness and standard deviation of each tested sample.

---

[2] The area function and instrument calibration was done on a fused silica standard.

Material	Difference in Hardness (GPa)	Standard deviation for a Site (GPa)
Cu	0.03	0.35
$Cu_{80}Ni_{20}$	0.04	0.25
$Cu_{55}Ni_{45}$	0.03	0.30
Ni	0.05	0.44

Table 6.1: **Regional Variation in Hardness.** Absolute difference in the measured hardness at the node and the beam for Cu, , $Cu_{80}Ni_{20}$, $Cu_{55}Ni_{45}$, and Ni. Standard deviation of measured hardness for this representative sample.

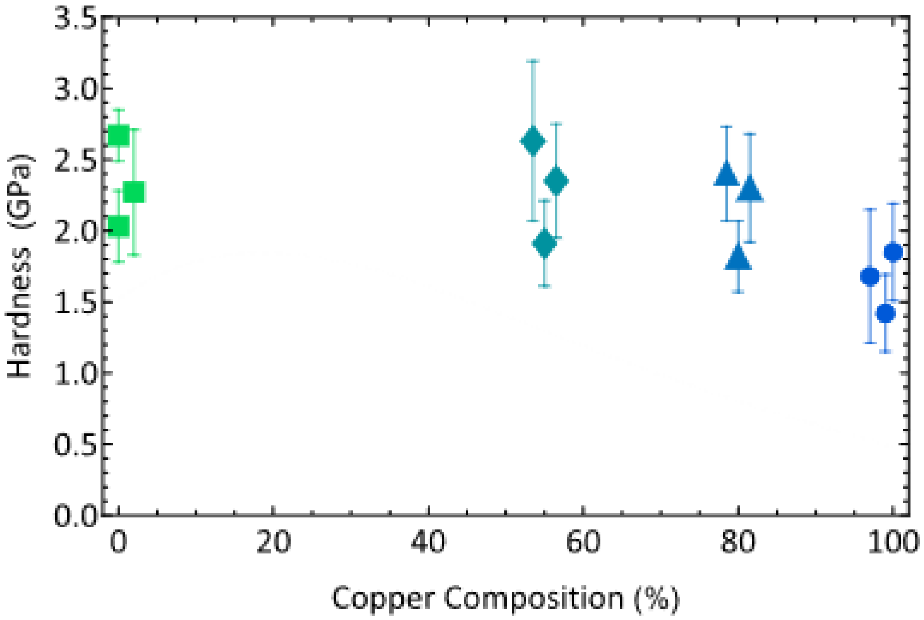

Figure 6.1: **Hardness in Hydrogel Infusion Cupronickel Alloys.** Plotted average and standard deviation of hardness as a function of compositions for cupronickel alloys for each tested sample. Samples are offset slightly by composition for readability. Only Cu, $Cu_{80}Ni_{20}$, $Cu_{55}Ni_{45}$, and Ni are tested. Grey dashed line represents solid-solution hardening behavior from previous literature [12]. Coloration of points is a mixture of blue (Cu) and green (Ni) corresponding to the alloy composition.

Table 6.2 provides the specific values for the measured hardness, standard deviation, and standard error for each sample.

Sizeable standard deviations (up to ~30% of the mean value) for each sample suggests localized nano-scale inhomogenities or variations. This fluctuation in hardness likely stems from variation in microstructure (i.e., the proximity to a grain or twin boundary), the local dislocation distributions, any hidden pores, and so forth. The size of the variance does not scale with mean hardness, indicating no clear relationship between the distribution of hardness and a change in the hardening mechanism. $Cu_{55}Ni_{45}$ demonstrates some of the

Material	Sample	Mean Hardness (GPa)	Standard Deviation (GPa)	Standard Error (GPa)
Cu	#1	1.85	0.35	0.03
	#2	1.52	0.37	0.07
	#3	1.68	0.47	0.06
$Cu_{80}Ni_{20}$	#1	2.32	0.38	0.08
	#2	2.39	0.33	0.03
	#3	1.82	0.25	0.03
$Cu_{55}Ni_{45}$	#1	1.91	0.30	0.03
	#2	2.35	0.40	0.03
	#3	1.52	0.56	0.11
Ni	#1	2.67	0.18	0.04
	#2	2.03	0.25	0.02
	#3	2.27	0.44	0.03

Table 6.2: The mean hardness, standard deviation, and standard error of each sample of Cu, $Cu_{80}Ni_{20}$, $Cu_{55}Ni_{45}$, and Ni measured by nanoindentation.

largest variation for individual samples. This matches with the relatively larger variation in twin boundary density observed for this composition. Though other microstructural features may be contributing to this localized change in hardness, twin boundaries are likely a large contribution.

The calculated standard error is small for all samples and indicates high confidences in the measured mean. Thus while standard deviation in hardness shows that an individual sample is likely to contain microscopic regions of similar hardness, the global behavior is statistically distinct sample-to-sample. This points to a processing-driven initiation of the distribution of hardening features. Localized interactions with plasticity mechanisms follows a fairly consistent deviation from this mean behavior.

As anticipated, the hardness of Ni is higher than Cu. A slight decrease in hardness with increased Cu content is observed. This deviates from the intuition of the cupronickel solid-solution hardening demonstrated by Bahr & Vasquez [12]. solid-solution hardening generally described the added hardening effect which comes from mixing in a solute atom to the lattice [28]. Dislocations encounter additional barriers to plasticity through the variation in local atomic potential [28]. Through systematically measured hardness with nanoindentation across various microcrystalline cupronickel alloys, Bahr & Vasquez [12] show a dramatic shift in hardness with a peak hardening in the nickel-rich regime of the alloy (See Appendix Figure L.1). However, this reference reports 50 µm grain sizes which are an order of magnitude larger than our materials. Thus, in order to properly analyze this trend, we must account for grain size and the presence of other various microstructural features which may impact the measured hardness in cupronickel alloys.

6.3 The Role of Boundaries on Hardness

To fully contextualize the hardness of these HI metals reported in Section 6.2, it is key to incorporate the microstructural perspective and analysis. Different materials are known to have stronger or weaker sensitives to the presence of boundaries as a hardening mechanisms. This is manifest through the Hall-Petch relations, which describes the increasing hardness of a material with decreasing grain size or average distance from a boundary and can be written through the following equation::

$$H = H_o + kD^{-1/2} \tag{6.2}$$

where H is the measured hardness, H_o is the intrinsic hardness (or hardness in single crystal), k is the scaling coefficient which indicates how sensitive the material is to the presence of boundaries, and D is the grain size. This phenomenon is explained by the interaction between dislocations and boundaries. In large grains, there is a greater ability for dislocations to both generate and move within a grain without meeting resistance and pile-up at a grain boundary, thus reducing the force needed to transmit a dislocation across the grain boundary. As the grain size decreases, the dislocation is more and more likely to encounter a grain boundary and be arrested in its slip motion. There is also less room for dislocation pile-up to occur. With smaller pile-ups, the applied stress required to transmit a dislocation across the boundary increases and thus a greater degree of hardening is observed. It is important to note that while the Hall-Petch relationship is often applied interchangeably to hardness and yield stress by approximating the yield stress as three times the hardness, this approximation is based on experimental observations and does not hold for all materials. As this data works with hardness values and we do not yet know how hardness and yield may be related in HI metals, we will focus on only interpreting the hardness and related hardening mechanisms. We will not draw relations to yield behaviors.

Similarly twin boundaries can act as barriers to dislocation motion. Chapter 5 demonstrates that the HI materials have high densities of $\Sigma 3$ and other CSL boundaries. To account for the contributions to hardening by twin boundaries, the Hall-Petch relationship can be modified with an effective grain size that better reflects the dislocation slip length. Pande *et al.* [155] developed a framework for calculated the additional hardening from isolated twin boundaries through the Hall-Petch relationship (Eq. 6.2). Building from their model, the following equation reformulates the relationship as an effective grain size, D_{eff}, which accounts for the presence of various types of twin boundaries:

$$H = H_0 + k\left(D_{eff}\right)^{-1/2} \tag{6.3}$$

This D_{eff} ultimately subdivides the typically measured grain size into smaller regions as dislocations can encounter these boundaries within the grain. It can be written as:

$$D_{eff} = \frac{D}{1 + pN} \tag{6.4}$$

where D is the grain size of the material; N is the average number of twin boundaries in a given grain; and p_i is the effectiveness of that particular twin boundary as a plasticity barrier. The values for p are scaled relative to the grain boundary barrier strength. For values of $p < 1$, the twin boundary requires less force than a grain boundary to transmit a dislocations. Twin bounadries are generally expected to be smaller dislocation barriers than grains but as an upper bound, we set p equal to 1. This analysis will not consider the relative difference in barrier strength between coherent and incoherent twin boundaries. Plugging Eq. 6.4 into the Hall-Petch equation (Eq. 6.2) we see the following relationship:

$$H = H_0 + k\left(\frac{D}{1 + pN}\right)^{-1/2} \tag{6.5}$$

A more general formulation:

$$H = H_0 + k\left(\frac{D}{1 + \Sigma_{i=1}^{N} p_i n_i}\right)^{-1/2} \tag{6.6}$$

allows for the addition of other types of boundaries which have different plasticity barrier coefficients or relative barrier strength. An important assumption of the Hall-Petch and modified Hall-Petch relationships is that the boundaries can be treated as isolated[3] (i.e., there are no interactions between boundaries or the action of one dislocation on a boundary does not also interact with another boundary). This assumption allows the addition of new boundaries to be independent and no higher order terms are needed when scaling the effective grain size.

To provide an upper bound for the contribution from these twin boundaries, p will be set to 1 for all boundary types. The average contribution of these twins can be effectively calculated by multiplying the fraction of grains with twin boundaries by the average number of boundaries in a twinned grain. Figure 6.2 shows the measured average sample hardness

---

[3] A breakdown of this assumption is one proposed contribution to deviations from the classical Hall-Petch relationship observed as materials approach the inverse Hall-Petch transition.

as compared to the predicted Hall-Petch Relationship and twin boundary correction for Cu, $Cu_{80}Ni_{20}$, and Ni. A scarcity of literature data on Hall-Petch behavior in $Cu_{80}Ni_{20}$ made direction calculation challenging. However, in order to have the observed behavior of $Cu_{80}Ni_{20}$ addressed purely by twin boundary hardening, the k value would need to be 1.19 assuming an intrinsic hardness equal to the hardness demonstrated in Bahr et al. [12] for 50 µm grains. This is a 28% increase as compared to the k value for $Cu_{55}Ni_{45}$. Though this value is not completely unreasonable, it is rests on several upper bound assumptions that weaken the feasibility of twin boundaries explaining the increased hardness.

All HI metals appear to exhibit universally higher hardness when compared to the literature. Table 6.3 highlights this observation by comparing the maximal increase in hardness due at the observed densities of Σ3 boundaries for Cu, $Cu_{55}Ni_{45}$, and Ni with the observed increase in hardness. The increase in hardness from the Hall-Petch prediction shows some deviation from the underlying solid-solution behavior of the alloy. Pure metals exhibit a larger increase than the alloy. Figure 6.3 shows that this deviation from solid-solution hardening is not correlated to twin boundary number density, nor is the increased degree of hardening. As Figure 6.3 (and Figure 6.4) calculates the difference from the unmodified Hall-Petch relationship, the shift from solid-solution hardening becomes even more pronounced when taking into account twin boundary contributions.

However, when looking at the correlation between twin line length density and increased hardness, Figure 6.4 demonstrates a positive correlation. With increased length of boundary, the likelihood of a dislocation encountering resistance and thus participating in hardening should increase. These initial findings indicate that the number of barriers to dislocation motion is less critical than the probability of encountering a barrier. Additionally, the alloyed material is more sensitive to boundaries than the pure metals. This lends to the presence of twins explaining a larger portion of increased hardness. However, a substantial portion of the hardening remains unexplained by twin boundaries and the relatively smaller increase in hardness cannot be encapsulated simply by the number of twin boundaries present. We make note that the presented hardening increase due to twins is an upper bound. Thus this comparison between hardness increased due to twins and the measured increase in hardness of HI metals represents the maximal contribution that twins could have in hardening behavior. Likely the twin boundaries contribute less.

Additionally, as non Σ3 CSL boundaries made up a relatively invariant fraction of the CSL boundaries, their contribution can be considered to generally scale with that of twin boundaries in the first approximation. Therefore, non Σ3 CSL boundaries are not expected to be strongly related to the greater relative increase in hardness found in HI metals.

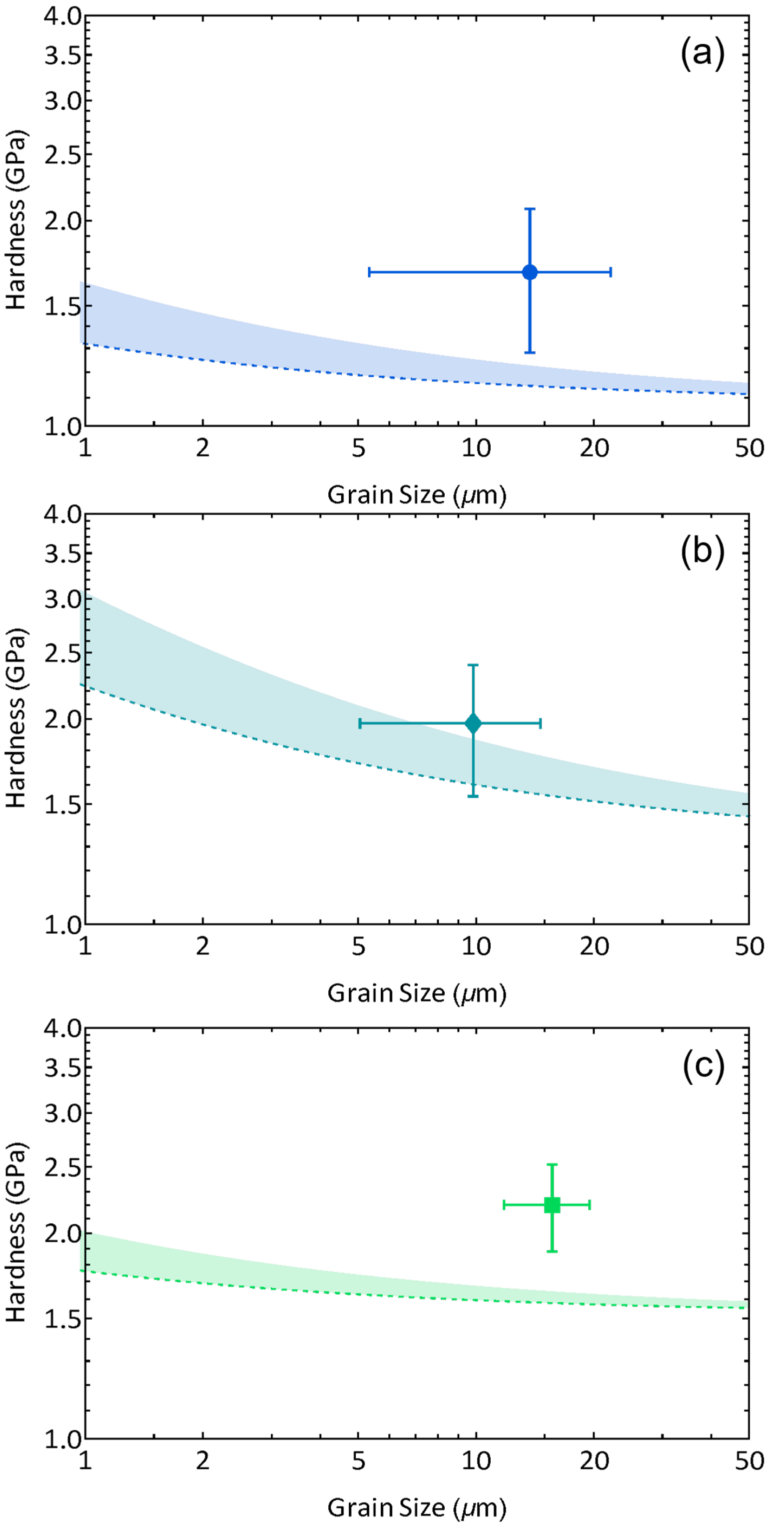

Figure 6.2: **Hall-Petch and Twin Boundary Hardening Compared to Hydrogel Infusion Metals.** Plotted as the mean hardness and area-weighted grain size for (a) Cu, (b) $Cu_{55}Ni_{45}$, and (c) Ni. The dashed line represents the predicted Hall-Petch Relationship from literature, and the shaded area is the possible increase in hardness due to the presence of twins as outlined in Eq. 6.4

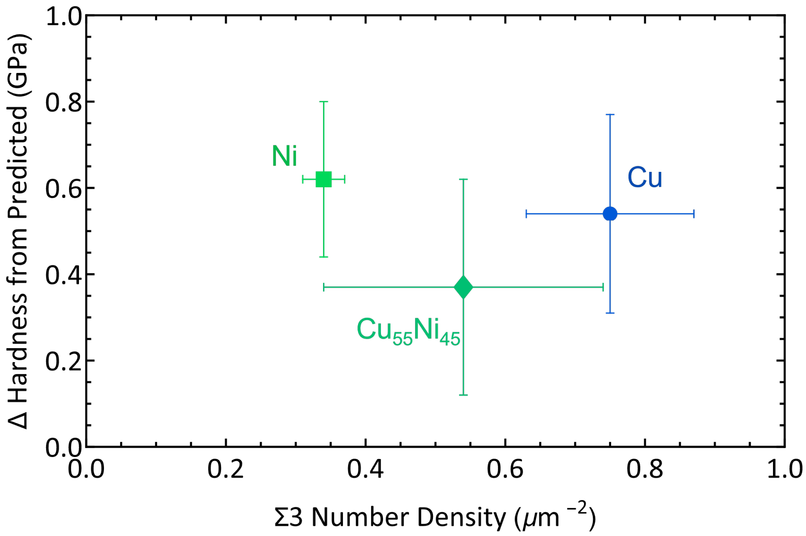

Figure 6.3: **Twin Number Density Relationship to Increased Hardness in HI Metals.** The average and standard deviation of both the twin number density and the deviation from literature reported hardness.

Material	Twin Correction Increase (GPa)	Observed Increase (GPa)
Cu	0.08	0.54
$Cu_{55}Ni_{45}$	0.26	0.37
Ni	0.06	0.62

Table 6.3: **Percentage Increase in Hardness Due to Twins.** The increase in hardness from the corrected Hall-Petch equation for HI Cu, $Cu_{55}Ni_{45}$, and Ni metals using the average twin densities observed and the experimentally observed increase in hardness.

From the clear correlation between line density and increased hardness from the predicted hardness, we see evidence for a twin boundary related mechanism for the degree of high hardness observed in HI curponickel metals. Though these twin boundaries do not fully explain the observed mechanical behavior, they support a substantive contribution in $Cu_{55}Ni_{45}$. While this lower twin boundary presence in the alloy provides a qualitative explanation for its smaller relative increase in hardness than the pure metals, further exploration of the microstructural space such as identifying any correlations between the residual of hardness and a local twin density may shed more light onto the role of twin boundaries in HI metal properties. While these findings supports twin boundaries as a contributing mechanism in the observed hardening, it also hints at additional or more complex microstructural relationships at play.

Another feature highlighted in Figures 6.4 and 6.3 is the overlap and similar size in standard error for the residuals of the measured hardness. As the standard error identifies the

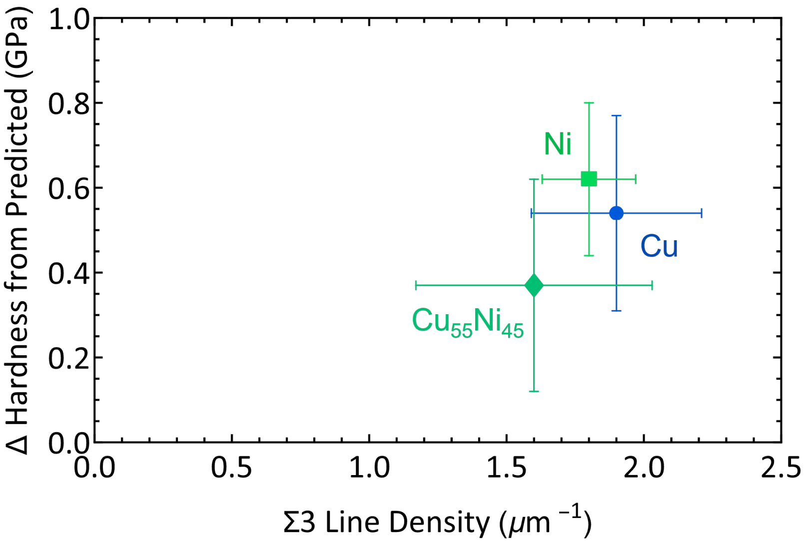

Figure 6.4: **Twin Line Density Relationship to Increased Hardness in HI Metals.** The average and standard deviation of both the twin line density and the deviation from literature reported hardness.

likely range of mean hardness, this metric is used in conjunction with the deviation from predicted hardness. This observed sample-to-sample variation highlights a sensitivity to minor variation innate to the processing method and points to further exploration and investigation of this highly kinetic processing method. Though individual materials could have very different relationships between the HI method and its resulting microstructure, the dominant hardening mechanisms are consistently present across all compositions.

The universal dramatic hardening of HI metals is not fully explained by high twin densities and must involve some other hardening mechanism, whether related to or completely independent from the boundaries discussed thus far. Some possible additional mechanism for hardening could be extremely small nano-pores on the order of <10 nm not readily seen in our TEM micrographs. Nano-pores of this size can act as a strengthening mechanism during nanoindentation by interacting with, and in some cases pinning, dislocations. However, these features mostly contribute to the variation in measured hardness unless in an excess of 10^{12} voids/cm^2 (or 100 voids/μm^2) [136]. Thus, for the TEM micrograph in Figure 5.9b, we would anticipate ~200-250 voids present. Though a few voids may be difficult to identify at the displayed magnifications, such a large density is clearly not observed. With no strong evidence for secondary phases, or grain boundary complexions, the only other observed microstructural factor which could contribute includes the heterogeneously dispersed aluminosilicate inclusions. The aluminosilicate inclusions are generally nanoscopic and heterogeneous throughout the structure. Given this distribution, we anticipate that any contributions to mechanical behavior from this feature would simply increase the local variance in measured hardness rather than increasing the average value. Ultimately the complete mechanistic understanding of hardness in HI metals remains an open question and deeper investigation needs to shine light onto how these boundaries may have different plasticity interactions than traditionally processed materials.

6.4 Summary and Conclusions

These nanoindentation results provide insight to a bulk-like response of Hi cupronickel metals. While the spread in measured hardness can be attributed to variance in the locally probed microstructure (i.e., close proximity to twin boundaries and grain boundaries, increasing hardness, and the presence of micro-porosity reducing it), the greater average hardness is indicative of a global complexity in the material not explained by a simple microstructural mechanism. Specific investigation into the role of twin boundaries shows no strong or defining correlation with the number of boundaries but clear correlation with line length density. Estimations of the twin boundary strengthening effect demonstrate additional mechanisms and material-specific interactions need to be uncovered to fully explain the hardening characteristic of HI metals.

Specifically, a more systematic coupling of hardness and microstructure could help untangle the role of composition and boundaries. By indentation on mapped EBSD regions, better insight into the local microstructure may assist in shedding light on the specific relationship between the hardness and microstructure of these materials. However, primary candidates for explaining the high hardness in HI metals include (1) the constituent material, (2) grain boundaries more broadly, and (3) special hardening contributions from triple junctions.

Within a singular grain, there may be a higher than typical density of dislocation loops or extremely small dissolved carbon which act as pinning points for dislocations, thus increasing hardness. Though less plausible, an unusually high fraction of dislocations which are edge as compared to screw character could result in an unexpectedly strong hardening response in the material as edge dislocations have greater resistance to twin boundaries than screw dislocations [121].

Due to the kinetic processes of the alloy from its phase-separated parent oxides, the grain boundaries may be inherently different than GBs found in cupronickel alloys produced through traditional methods. While compressions on FIB-made GB-containing nanopillars may illuminate any anomalous mechanical behavior, more in-depth high-resolution TEM and possibly high-resolution 3D-EBSD[4] would greatly aid in understanding the role of GBs in hardness.

Finally we consider the possibility of triple junctions providing an additional hardening mechanism. This will be highly dependent not only on the density of triple junctions but also the character of boundaries entering those junctions. Some work has shown triple junctions to increase hardness while others have indicated that triple junctions featuring high-mobility CSL type boundaries do not [49, 103, 104]. All these hypotheses require further microstructural characterization and would benefit from both a more densely explored alloying composition space and micropillar investigations on various boundaries and junctions within the material.

While the experiments outlined in this chapter open many more questions about the mechanical behavior of HI metals, we demonstrate twin boundaries alone do not explain an uncharacteristically high hardness measured in HI Cu, Ni, and cupronickel alloys. These materials demonstrate the intriguing opportunity for further investigation into competing complexities within HI manufactured metals. Furthermore, the 1.5x relative increase in the adjusted hardness of pure metals as compared to alloys hints at a greater material-dependent relationship to these plasticity processes than seen in other manufacturing methods. The dramatically altered mechanical response of HI cupronickel alloys opens a new avenue for engineering and investigating complex material behavior.

---

[4] For the lengthscales of interest in our microstructure, 3D EBSD maps are typically taken by FIBing away layers after each high-resolution scans. After this destructive process, the images can be combined to reconstruct whole volume with unique metrics like grain boundary roughness, contouring, and grain volume estimates.

Chapter 7

CONCLUDING REMARKS

7.1 Summary

This work emphasizes the importance of boundaries and interfaces at the nanoscale. We demonstrate how the interfaces between nanowires dictate much of the failure in dense nanowire bundles. We show that the interplay of both grain and structure dimensions in nano-architected nc-ZnO leads to unique size effects and emergent phenomena. We laid the foundation in exploring and untangling the contributions of twin boundaries, grain size, and other microstructural features in Hydrogel Infusion microlattices.

The outlined experiments highlight the role of localization in micro and nano-scale behavior. Accumulation of localized failure in nanowire bundles shifts leads to access of buckling modes and ultimate failure strength at lower engineering stresses than predicted from a simple parallel nanowire model. Stress-relaxation along the grain boundaries in nc-ZnO enables post-yield piezoelectric behavior. However, these grain boundaries also locally concentrate stress leading to cooperative shear banding in micron-sized structures. Even in microcrystalline alloys, this localization is apparent as the fluctuation in local hardness is linked to the presence of twin boundaries. This further extends to help the dissection of microstructure and mechanical properties in HI metals, particularly when investigating their high hardness.

We have also emphasized the importance of a statistical viewpoint to help explain emergent behavior. Through statistical treatment of localized failure accumulation, we devise a model for predicting global failure in nanowire bundles. In microscale materials, we highlight how even with millions of grains, a material may not have an net-averaging response. Though demonstrated for intrinsic electromechanically coupled materials, the fluctuation due to imperfect cancellation can apply to many crystallographically coupled properties.

This work puts forth investigations of three newly manufactured micro- and nano-scopic material systems. We report and provide analytic frameworks for approaching the observed behavior which arise from novel microstructural considerations. Through these examples we highlight the important role of boundaries and other microstructural features on emergent mechanical and mechanically-coupled phenomena at the nanoscale.

7.2 Outlook

As technology asks for materials at new extremes, we, as material scientists, navigate a fine balance between investigating the produced performance of the real material and understanding the fundamental mechanisms which make up and contribute to the global picture. At the nanoscale, we sit on the cusp of continuum where the discrete nature of microstructure becomes far more finely resolved. Only recent advances have enabled the engineering and design of nanoscopic materials to truly bridge the gap in structural and nano-mechanics. With this ability to build complex nano-architectures from functional materials, we have opened opportunities not only to engineering the next generation of nanotechnologies but also to study underlying questions about microstructural phenomena.

When Microstructure Becomes More Complex

As emphasized in this work, mechanical properties of structural materials are derived from their microstructural features, particularly boundaries. While the effects of individual features are well understood in isolated or simple systems, a novel class of materials, defined by its non-equilibrium and complex microstructure, is emerging. These materials exhibit enhanced properties due to both competitive and cooperative interactions between various components at the microscale, and even some microscopic materials are shown to have unexpected behavior due to their unusual microstructures. Particularly in microscopic and nanoscopic structures, the average continuum-like behavior may fail to predict or explain observed response due to high sensitivity to localized behavior. To paint a fully robust picture, we need to build a better understanding and stronger theoretic basis for the complex (and likely non-linear) interactions between lengthscale and boundaries on mechanical and mechanically-coupled phenomena.

Advancing the Techniques for Measurements and Analysis of Microstructure-to-Mechanical Properties

With the emergence of more complex microstructures, new opportunities have arisen in both engineering and fundamental investigations as discussed throughout this thesis. However, novel methods are necessary to better and more fully unravel the intricacies of emergent microstructure-mechanical behavior. As we begin to untangle the many possible contributions or non-linear interactions stemming from new processing techniques, advanced statistical treatments are critical for learning causal relationships and building models for material behavior. One set of these statistical tool, which hold great promise, is Machine Learning (ML). Often associated with developing predictive models, ML has been derided as a black-box or blind approach where little mechanistic insight can be drawn to

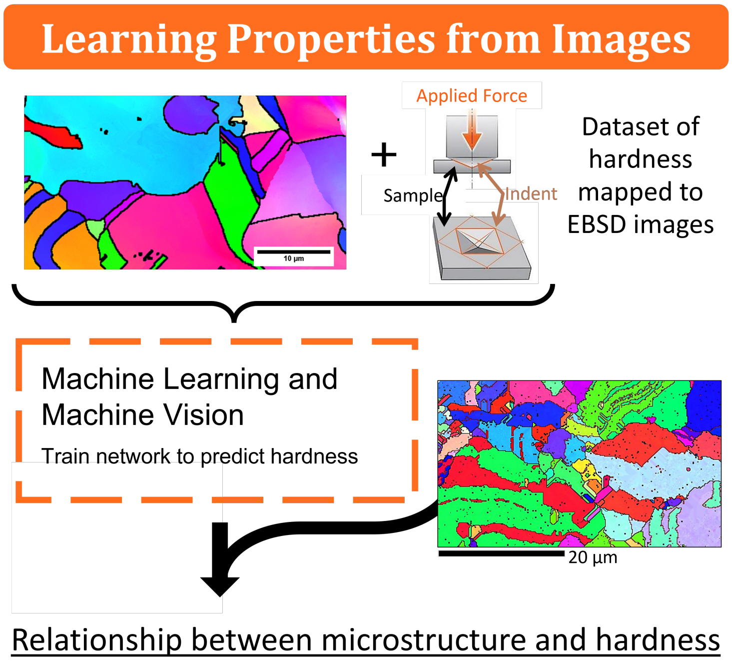

Figure 7.1: **Machine Vision Aided Microstructural Learning.** Schematic outlining one possible way in which EBDS and mechanical testing could be coupled through machine vision to learn the sensitivity and relationship of complex or localized structures on performance.

the underlying and fundamental behavior which gives rise to the observed relationship. However, this criticism highlights an incredibly important point: statistical methods need to be paired with intentionally designed experiments to extract meaningful relationships between variables. The particular power of ML lies in its application to data with many variables (otherwise known as high dimensional data) and its ability to provide insight to the sensitivity, categorization, and coupling of those variables.

For materials, this is incredibly powerful within microstructural focused investigations, where so many features can contribute to observed properties. Imaging techniques often produce our most data- and information-rich measurements of microstructural attributes. When coupled with other types of testing, we can link specific features to properties and further understand the mechanisms of material behavior. Machine vision is a type of machine learning which is highly specialized to help identify features in images. Paired with techniques like EBSD and other machine learning algorithms, machine vision not only can help provide rapid analysis of produced data, but also lend insight to the components most critical to predicting properties, generate equivalent microstructures for simulations, and more. As AM and other manufacturing techniques push the rapid development of new, complex, and extreme microstructures, the advancement of machine vision-aided analysis can enable stronger statistically inclusive investigations into complex systems with various competing mechanisms.

Nano-architected Materials Engineering

Nano-architectures have been investigated, studied, and designed to push the extremes of structural capability at the smallest scales. For mechanical functionality, studies have focused on leveraging form rather than constituent material because these structures are most easily produced with polymers. Some investigations into hollow metallic and alumina structures and carbonaceous materials have set the stage for a more materially focused bridge between nanomechanical and nanoarchitected [18, 161]. However, these microstructures are predominantly amorphous, leaving out so many of the fun defects and mechanisms which serve as our tiniest engineering tools. As nanoscale additive manufacturing opens the material space to crystalline, microstructrually complex materials, there is enormous opportunity to join the disciplines of both nanoscale structural mechanics and nanomechanics. To pave the path for future generations of nanotechnology, we need to dive more deeply and understand the role of more complex stress states, statistical and stocastic behavior, and nanoscale processing on microstrural mechanisms. If we can harness these interactions, not only can we launch an amazing new engineering space, but we also chip away at the deeper underlying phenomena that ultimately form the foundation of nanoscience.

Using Hydrogel Infusion for Materials Microstructural Engineering

Chapters 5 and 6 demonstrate the potential of Hydrogel Infusion as a technique for creating micro-scale additively manufactured materials with distinct microstructural features from the prevalent melt-pool based AM of metals. In addition to opening the material space, HI metals exhibit a high hardness as compared to other traditional methods of material manufacturing. However, this is barely scratches the surface of opportunities for expanding material and microstructural engineering through the HI method.

From a fundamental perspective, HI provides both the challenge and leverage of phase transformation on boundary structures. Whether a simple stable transformation or a complex shift in crystallographic structure, HI materials open a new playground for thinking about the underlying physics of microstructural evolution. Hydrogel infusion is an easy platform to navigate the material phase space and investigate interfaces, from grain boundaries to free surfaces, at the micro- and nano-scales.

As an engineering opportunity, HI opens imaginative opportunities to use structural length-scale to influence heterogeneous microstructures. In leveraging the architecture, specific local stresses during shrinkage, or diffusion path length could enable heterogeneous microstructures. With such specialization, not only could the structure but the material itself be designed to add specific localized properties or complex structural behavior. By expanding our ability to control microstructural effects to complex geometries, HI opens a new tool for creativity in designing micro- and nano-architected structures.

As AM opens the design of materials at the micro and nano-scale, it is critical to bridge the gap between the nanomechanical world of microstructural mechanisms and the structural mechanics vision of complex architectures. Truly advanced small-scale materials requires the marriage of these disciplines and the creative insights of materials engineering to realize their full promise and potential.

BIBLIOGRAPHY

[1] Fast parallel algorithms for short-range molecular dynamics. *Journal of Computational Physics*, 117(1):1–19, 1995. ISSN 0021-9991. URL `https://doi.org/10.1006/jcph.1995.1039`.

[2] Plasticity in small-sized metallic systems: Intrinsic versus extrinsic size effect. *Progress in Materials Science*, 56(6):654–724, 2011. ISSN 0079-6425. URL `https://doi.org/10.1016/j.pmatsci.2011.01.005`. Festschrift Vaclav Vitek.

[3] R. Agrawal, B. Peng, E. G. Gdoutos, and H. D. Espinosa. Elastic size effects in zno nanowires – a combined experimental-computational approach. *Nano Lett.*, 8:3668, 2008.

[4] Ravi Agrawal and Horacio D. Espinosa. Giant piezoelectric size effects in zinc oxide and gallium nitride nanowires. a first principles investigation. *Nano Letters*, 11(2): 786–790, 2011. URL `https://doi.org/10.1021/nl104004d`.

[5] Ravi Agrawal, Bei Peng, Eleftherios E. Gdoutos, and Horacio D. Espinosa. Elasticity size effects in zno nanowires - a combined experimental-computational approach. *Nano Letters*, 8(11):3668–3674, 2008. URL `https://doi.org/10.1021/nl801724b`.

[6] Ravi Agrawal, Bei Peng, and Horacio D. Espinosa. Experimental-computational investigation of zno nanowires strength and fracture. *Nano Letters*, 9(12):4177–4183, 2009. URL `https://doi.org/10.1021/nl9023885`.

[7] Bok Y Ahn, Eric B Duoss, Michael J Motala, Xiaoying Guo, Sang-Il Park, Yujie Xiong, Jongseung Yoon, Ralph G Nuzzo, John A Rogers, and Jennifer A Lewis. Omnidirectional printing of flexible, stretchable, and spanning silver microelectrodes. *Science*, 323(5921):1590–1593, 2009. URL `https://doi.org/10.1126/science.1168375`.

[8] Frances I Allen, Nathan R Velez, Rachel C Thayer, Nipam H Patel, Mary Ann Jones, Gregory F Meyers, and Andrew M Minor. Gallium, neon and helium focused ion beam milling of thin films demonstrated for polymeric materials: study of implantation artifacts. *Nanoscale*, 11(3):1403–1409, 2019. URL `https://doi.org/10.1039/C8NR08224C`.

[9] Smaïl Amari, Jean-Marie Verilhac, Eric Gros D'Aillon, Alain Ibanez, and Julien Zaccaro. Optimization of the growth conditions for high quality ch3nh3pbbr3 hybrid perovskite single crystals. *Crystal Growth & Design*, 20(3):1665–1672, 2020. URL `https://doi.org/10.1021/acs.cgd.9b01429`.

[10] Mohsen Taheri Andani, Aaditya Lakshmanan, Veera Sundararaghavan, John Allison, and Amit Misra. Quantitative study of the effect of grain boundary parameters on the

slip system level hall-petch slope for basal slip system in mg-4al. *Acta Materialia*, 200:148–161, 2020. URL `https://doi.org/10.1016/j.actamat.2020.08.079`.

[11] Sumit Bahl, Sumeet Mishra, KU Yazar, Immanuel Raju Kola, Kaushik Chatterjee, and Satyam Suwas. Non-equilibrium microstructure, crystallographic texture and morphological texture synergistically result in unusual mechanical properties of 3d printed 316l stainless steel. *Additive Manufacturing*, 28:65–77, 2019.

[12] DF Bahr and G Vasquez. Effect of solid solution impurities on dislocation nucleation during nanoindentation. *Journal of materials research*, 20(8):1947–1951, 2005. URL `https://doi.org/10.1557/JMR.2005.0244`.

[13] B. Balzer, M. Hagemeister, P. Kocher, and L. J. Gauckler. Mechanical strength and microstructure of zinc oxide varistor ceramics. *J. Am. Ceram. Soc.*, 87:1932, 2004.

[14] Andrei V Bandura, Robert A Evarestov, Sergey I Lukyanov, Sergei Piskunov, and Yuri F Zhukovskii. Simulation of young's moduli for hexagonal ZnO [0 0 0 1]-oriented nanowires: first principles and molecular mechanical calculations. *Materials Research Express*, 4(8):085014, aug 2017. URL `https://doi.org/10.1088/2053-1591/aa7732`.

[15] S Bansal, E Toimil-Molares, A Saxena, and Rao R Tummala. Nanoindentation of single crystal and polycrystalline copper nanowires. pages 71–76, 2005.

[16] Afrooz Barnoush, Peter Hosemann, Jon Molina-Aldareguia, and Jeffrey M Wheeler. In situ small-scale mechanical testing under extreme environments. *Mrs Bulletin*, 44 (6):471–477, 2019. URL `https://doi.org/10.1557/mrs.2019.126`.

[17] Sunandan Baruah and Joydeep Dutta. Hydrothermal growth of zno nanostructures. *Science and technology of advanced materials*, 2009.

[18] Jens Bauer, Lucas R Meza, Tobias A Schaedler, Ruth Schwaiger, Xiaoyu Zheng, and Lorenzo Valdevit. Nanolattices: an emerging class of mechanical metamaterials. *Advanced Materials*, 29(40):1701850, 2017.

[19] A. K. Bhattacharya and W. D. Nix. Analysis of elastic and plastic deformation associated with indentation testing of thin films on substrates. *International Journal of Solids and Structures*, 24(12):1287–1298, 1988. URL `https://doi.org/10.1016/0020-7683(88)90091-1`.

[20] VB Biscuola and MA Martorano. Mechanical blocking mechanism for the columnar to equiaxed transition. *Metallurgical and Materials Transactions A*, 39(12):2885–2895, 2008.

[21] S. V. Bobylev, N. F. Morozov, and I. A. Ovid'ko. Cooperative grain boundary sliding and migration process in nanocrystalline solids. *Phys. Rev. Lett.*, 105:055504, Jul 2010. URL `https://doi.org/10.1103/PhysRevLett.105.055504`.

[22] G Boissonnet, C Chalk, JR Nicholls, G Bonnet, and F Pedraza. Phase stability and thermal insulation of ysz and erbia-yttria co-doped zirconia eb-pvd thermal barrier coating systems. *Surface and Coatings Technology*, 389:125566, 2020. URL `https://doi.org/10.1016/j.surfcoat.2020.125566`.

[23] Cecile Bonifacio, Pawel Nowakowski, Mary Ray, and Paul Fischione. Alternative post-fib polishing using low-energy argon ion milling to prevent grid redeposition. *Microscopy and Microanalysis*, 27(S1):426–429, 2021. URL `https://doi.org/10.1017/S1431927621002038`.

[24] Giovanni Bonny, Dimitri Terentyev, Alexander Bakaev, EE Zhurkin, Marc Hou, Dimitri Van Neck, and Lorenzo Malerba. On the thermal stability of late blooming phases in reactor pressure vessel steels: An atomistic study. *Journal of nuclear materials*, 442(1-3):282–291, 2013. URL `https://doi.org/10.1016/j.jnucmat.2013.08.018`.

[25] Michał A. Borysiewicz. Zno as a functional material, a review. *Crystals*, 9(10), 2019. ISSN 2073-4352. URL `https://doi.org/10.3390/cryst9100505`.

[26] DG Brandon. The structure of high-angle grain boundaries. *Acta metallurgica*, 14 (11):1479–1484, 1966.

[27] SI Bulychev, VP Alekhin, M Kh Shorshorov, AP Ternovskij, and GD Shnyrev. Determination of young modulus by the hardness indentation diagram. *Zavodskaya Laboratoriya*, 41(9):1137–1140, 1975.

[28] MZ Butt and P Feltham. Solid-solution hardening. *Journal of materials science*, 28 (10):2557–2576, 1993.

[29] Wei Cai and William D Nix. *Imperfections in crystalline solids*. Cambridge University Press, 2016.

[30] Patrick R Cantwell, Timofey Frolov, Timothy J Rupert, Amanda R Krause, Christopher J Marvel, Gregory S Rohrer, Jeffrey M Rickman, and Martin P Harmer. Grain boundary complexion transitions. *Annu. Rev. Mater. Res*, 50(1):465–492, 2020.

[31] Yao-Yu Cao, Nobuyuki Takeyasu, Takuo Tanaka, Xuan-Ming Duan, and Satoshi Kawata. 3d metallic nanostructure fabrication by surfactant-assisted multiphoton-induced reduction. *Small*, 5(10):1144–1148, 2009. URL `https://doi.org/10.1002/smll.200801179`.

[32] CE Carlton and PJ Ferreira. What is behind the inverse hall-petch effect in nanocrystalline materials? *Acta Materialia*, 55(11):3749–3756, 2007. URL `https://doi.org/10.1016/j.actamat.2007.02.021`.

[33] CB Carter and SM Holmes. The stacking-fault energy of nickel. *The Philosophical Magazine: A Journal of Theoretical Experimental and Applied Physics*, 35(5):1161–1172, 1977.

[34] Mathieu César, Dongping Liu, Daniel Gall, and Hong Guo. Calculated resistances of single grain boundaries in copper. *Physical Review Applied*, 2(4):044007, 2014.

[35] Shou-Yi Chang and Ting-Kui Chang. Grain size effect on nanomechanical properties and deformation behavior of copper under nanoindentation test. *Journal of applied physics*, 101(3):033507, 2007.

[36] Wei-Hao Chen, Chia-Yueh Chou, Bao-Jhen Li, Shao-Liang Cheng, and Cheng-Yi Liu. Plastic deformation of zno thin films through edge and screw dislocation movements. *Journal of the American Ceramic Society*, 104(12):6579–6588, 2021. URL `https://doi.org/10.1111/jace.18010`.

[37] O Chichvarina, TS Herng, KC Phuah, W Xiao, N Bao, YP Feng, and J Ding. Stable zinc-blende zno thin films: formation and physical properties. *Journal of materials science*, 50(1):28–33, 2015.

[38] J. A. Christman, H. Maiwa, S. H. Kim, A. I. Kingon, and R. J. Nemanich. Piezoelectric measurements with atomic force microscopy. *Mater. Res. Soc. Symp. Pro.*, 541:617, 1998.

[39] David J Cooke, Arnaud Marmier, and Stephen C Parker. Surface structure of (1010) and (1120) surfaces of zno with density functional theory and atomistic simulation. *The Journal of Physical Chemistry B*, 110(15):7985–7991, 2006. URL `https://doi.org/10.1021/jp0564445`.

[40] V. Craciun, J. Elders, J.G.E. Gardeniers, J. Geretovsky, and Ian W. Boyd. Growth of zno thin films on gaas by pulsed laser deposition. *Thin Solid Films*, 259(1):1–4, 1995. ISSN 0040-6090. URL `https://doi.org/10.1016/0040-6090(94)09479-9`.

[41] Yuan Xiang Dan Tan and Yongsheng Leng. Molecular simulation study of piezoelectric potential distribution in a zno nanowire under mechanical bending. *MRS Advances*, 2:3433–3439, 2017. URL `https://doi.org/10.1557/adv.2017.318`.

[42] Marcelo Davanco, Liu Jin, Luca Sapienza, Chen-Zhao Zhang, Jose De, Varun Verma, Richard Mirin, Sae Nam, Liu Liu, and Kartik Srinivasan. Heterogeneous integration for on-chip quantum photonic circuits with single quantum dot devices. (8), 2017-10-12 2017. URL `https://doi.org/10.1038/s41467-017-00987-6`.

[43] Jesús del Barrio and Carlos Sánchez-Somolinos. Light to shape the future: From photolithography to 4d printing. *Advanced Optical Materials*, 7(16):1900598, 2019. URL `https://doi.org/10.1002/adom.201900598`.

[44] W. Deng, L. Jin, B. Zhang, Y. Chen, L. Mao, H. Zhang, and W. Yang. A flexible field-limited ordered zno nanorod-based self-powered tactile sensor array for electronic skin. *Nanoscale*, 8:16302, 2016.

[45] M Desaeger and Ignace Verpoest. On the use of the micro-indentation test technique to measure the interfacial shear strength of fibre-reinforced polymer composites.

Composites science and technology, 48(1-4):215–226, 1993. URL `https://doi.org/10.1016/0266-3538(93)90139-8`.

[46] A.V. Desai and M.A. Haque. Mechanical properties of zno nanowires. *Sensors and Actuators A: Physical*, 134(1):169–176, 2007. ISSN 0924-4247. URL `https://doi.org/10.1016/j.sna.2006.04.046`. International Mechanical Engineering congress and Exposition 2005.

[47] Serge Desgreniers, Luc Beaulieu, and Ian Lepage. Pressure-induced structural changes in zns. *Physical Review B*, 61(13):8726, 2000.

[48] Raabe Dierk. 8 - introduction to discrete dislocation statics and dynamics. In KOENRAAD G.F. JANSSENS, DIERK RAABE, ERNST KOZESCHNIK, MARK A. MIODOWNIK, and BRITTA NESTLER, editors, *Computational Materials Engineering*, pages 267–316. Academic Press, Burlington, 2007. ISBN 978-0-12-369468-3. URL `https://doi.org/10.1016/B978-012369468-3/50008-3`.

[49] DJ Dingley and RC Pond. On the interaction of crystal dislocations with grain boundaries. *Acta Metallurgica*, 27(4):667–682, 1979.

[50] Huajian Gao Dongchan Jang, Xiaoyan Li and Julia R. Greer. Deformation mechanisms in nanotwinned metal nanopillars. *Nature Nanotech*, 7:594–601, 2012. URL `https://doi.org/10.1038/nnano.2012.116`.

[51] Jun-Ping Du, WT Geng, Kazuto Arakawa, Ju Li, and Shigenobu Ogata. Hydrogen-enhanced vacancy diffusion in metals. *The Journal of Physical Chemistry Letters*, 11(17):7015–7020, 2020. URL `https://doi.org/10.1021/acs.jpclett.0c01798`.

[52] Luizetta V. Elliott, Erika E. Salzman, and Julia R. Greer. Stimuli responsive shape memory microarchitectures. *Advanced Functional Materials*, 31(9):2008380, 2021. URL `https://doi.org/10.1002/adfm.202008380`.

[53] Friederike Emeis, Martin Peterlechner, Sergiy V Divinski, and Gerhard Wilde. Grain boundary engineering parameters for ultrafine grained microstructures: Proof of principles by a systematic composition variation in the cu-ni system. *Acta Materialia*, 150:262–272, 2018.

[54] H. D. Espinosa, R. A. Bernal, and M. A. Minary-Jolandan. Review of mechanical and electromechanical properties of piezoelectric nanowires. *Adv. Mater.*, 24:4656, 2012.

[55] Horacio D. Espinosa, Rodrigo A. Bernal, and Majid Minary-Jolandan. A review of mechanical and electromechanical properties of piezoelectric nanowires. *Advanced Materials*, 24(34):4656–4675, 2012. URL `https://doi.org/10.1002/adma.201104810`.

[56] Cecilia Fager, Magnus Röding, Anna Olsson, Niklas Lorén, Christian von Corswant, Aila Särkkä, and Eva Olsson. Optimization of fib-sem tomography and reconstruction for soft, porous, and poorly conducting materials. *Microscopy and Microanalysis*, 26(4):837–845, 2020. URL `https://doi.org/10.1017/S1431927620001592`.

[57] Qihong Fang, Yang Chen, Jia Li, Chao Jiang, Bin Liu, Yong Liu, and Peter K Liaw. Probing the phase transformation and dislocation evolution in dual-phase high-entropy alloys. *International Journal of Plasticity*, 114:161–173, 2019.

[58] Christopher J. Fennell and J. Daniel Gezelter. Is the ewald summation still necessary? pairwise alternatives to the accepted standard for long-range electrostatics. *The Journal of Chemical Physics*, 124(23):234104, 2006. URL `https://doi.org/10.1063/1.2206581`.

[59] T Frolov, SV Divinski, M Asta, and Y Mishin. Effect of interface phase transformations on diffusion and segregation in high-angle grain boundaries. *Physical review letters*, 110(25):255502, 2013.

[60] R. Gaillac, P. Pullumbi, and F.-X. Coudert. Elate: an open-source online application for analysis and visualization of elastic tensors. *J. Phys.: Condens. Matter*, 28: 275201, 2016.

[61] PCJ Gallagher. The influence of alloying, temperature, and related effects on the stacking fault energy. *Metallurgical Transactions*, 1(9):2429–2461, 1970.

[62] Patrick Galliker, Julian Schneider, Hadi Eghlidi, Stefan Kress, Vahid Sandoghdar, and Dimos Poulikakos. Direct printing of nanostructures by electrostatic autofocussing of ink nanodroplets. *Nature communications*, 3(1):1–9, 2012. URL `https://doi.org/10.1038/ncomms1891`.

[63] Rebecca A. Gallivan and Julia R. Greer. Failure mechanisms in vertically aligned dense nanowire arrays. *Nano Letters*, 21(18):7542–7547, 2021. URL `https://doi.org/10.1021/acs.nanolett.1c01944`.

[64] Huajian Gao and Yonggang Huang. Geometrically necessary dislocation and size-dependent plasticity. *Scripta Materialia*, 48(2):113–118, 2003. URL `https://doi.org/10.1016/S1359-6462(02)00329-9`.

[65] J. G. E. Gardeniers, Z. M. Rittersma, and G. J. Burger. Preferred orientation and piezoelectricity in sputtered zno films. *Journal of Applied Physics*, 83(12):7844–7854, 1998. URL `https://doi.org/10.1063/1.367959`.

[66] A. Giwa, Z. H. Aitken, P. K. Liaw, Y.-W. Zhang, and J. R. Greer. Effect of temperature on small-scale deformation of individual face-centered-cubic and body-centered-cubic phases of al-.7cocrfeni high-entropy alloy. *Mater. Des.*, 191:108611, 2020.

[67] Rostam Golesorkhtabar, Pasquale Pavone, Jürgen Spitaler, Peter Puschnig, and Claudia Draxl. Elastic: A tool for calculating second-order elastic constants from first

principles. *Computer Physics Communications*, 184(8):1861–1873, 2013. URL `https://doi.org/10.1016/j.cpc.2013.03.010`.

[68] Stéphane Gorsse, Christopher Hutchinson, Mohamed Gouné, and Rajarshi Banerjee. Additive manufacturing of metals: a brief review of the characteristic microstructures and properties of steels, ti-6al-4v and high-entropy alloys. *Science and Technology of advanced MaTerialS*, 18(1):584–610, 2017. URL `https://doi.org/10.1080/14686996.2017.1361305`.

[69] Julia R Greer, Warren C Oliver, and William D Nix. Size dependence of mechanical properties of gold at the micron scale in the absence of strain gradients. *Acta Materialia*, 53(6):1821–1830, 2005. URL `https://doi.org/10.1016/j.actamat.2004.12.031`.

[70] X. Wendy Gu, Colleen N. Loynachan, Zhaoxuan Wu, Yong-Wei Zhang, David J. Srolovitz, and Julia R. Greer. Size-dependent deformation of nanocrystalline pt nanopillars. *Nano Letters*, 12(12):6385–6392, 2012. URL `https://doi.org/10.1021/nl3036993`.

[71] X Wendy Gu, Zhaoxuan Wu, Yong-Wei Zhang, David J Srolovitz, and Julia R Greer. Microstructure versus flaw: mechanisms of failure and strength in nanostructures. *Nano letters*, 13(11):5703–5709, 2013.

[72] Zhouzhou Gu, Rui Yang, Jun Yang, Xiaoyan Qiu, Rongjuan Liu, Yong Liu, Zhiping Zhou, and Yijing Nie. Dynamic monte carlo simulations of effects of nanoparticle on polymer crystallization in polymer solutions. *Computational Materials Science*, 147: 217–226, 2018. URL `https://doi.org/10.1016/j.commatsci.2018.02.009`.

[73] Dezhou Guo, Shuangxi Song, Ruichun Luo, William A. Goddard, Mingwei Chen, Kolan Madhav Reddy, and Qi An. Grain boundary sliding and amorphization are responsible for the reverse hall-petch relation in superhard nanocrystalline boron carbide. *Phys. Rev. Lett.*, 121:145504, Oct 2018. URL `https://doi.org/10.1103/PhysRevLett.121.145504`.

[74] EO Hall. The deformation and ageing of mild steel: Iii discussion of results. *Proceedings of the Physical Society. Section B*, 64(9):747, 1951.

[75] Seung Min Han, Tara Bozorg-Grayeli, James R. Groves, and William D. Nix. Size effects on strength and plasticity of vanadium nanopillars. *Scripta Materialia*, 63 (12):1153–1156, 2010. ISSN 1359-6462. URL `https://doi.org/10.1016/j.scriptamat.2010.08.011`.

[76] Junhua Hao, Zhengjia Wang, and Qinghua Jin. Dft study of structural, elastic, electronic and dielectric properties of blue phosphorus nanotubes. *Scientific Reports*, (9), 2019. URL `https://doi.org/10.1038/s41598-019-47764-7`.

[77] William T Harris. Chemical milling. the technology of cutting materials by etching. *Oxford University Press, New York. 1976, 371 p*, 1976.

[78] KS Sree Harsha. *Principles of vapor deposition of thin films*. Elsevier, 2006. URL `https://doi.org/10.1016/B978-0-08-044699-8.X5000-1`.

[79] A. Herzi, M. Sebais, B. Boudine, O. Halimi, B. Rahal, and L. Guerbous. Fabrication and Characterization of Highly Textured Thin Films of Undoped and Ag-Doped ZnO. *Acta Physica Polonica A*, 135(3):526–531, March 2019. URL `https://doi.org/10.12693/APhysPolA.135.526`.

[80] Eric D Hintsala, Ude Hangen, and Douglas D Stauffer. High-throughput nanoindentation for statistical and spatial property determination. *Jom*, 70(4):494–503, 2018. URL `https://doi.org/10.1007/S11837-018-2752-0`.

[81] Luca Hirt, Stephan Ihle, Zhijian Pan, Livie Dorwling-Carter, Alain Reiser, Jeffrey M Wheeler, Ralph Spolenak, János Vörös, and Tomaso Zambelli. Template-free 3d microprinting of metals using a force-controlled nanopipette for layer-by-layer electrodeposition. *Advanced materials*, 28(12):2311–2315, 2016. URL `https://doi.org/10.1002/adma.201504967`.

[82] Luca Hirt, Alain Reiser, Ralph Spolenak, and Tomaso Zambelli. Additive manufacturing of metal structures at the micrometer scale. *Advanced Materials*, 29(17): 1604211, 2017. URL `https://doi/10.1002/adma.201604211`.

[83] John Price Hirth, Jens Lothe, and T Mura. Theory of dislocations. *Journal of Applied Mechanics*, 50(2):476, 1983.

[84] Haw-Wen Hsiao, Shu Li, Karin A. Dahmen, and Jian-Min Zuo. Shear banding mechanism in compressed nanocrystalline ceramic nanopillars. *Phys. Rev. Materials*, 3:083601, Aug 2019. URL `https://doi.org/10.1103/PhysRevMaterials.3.083601`.

[85] Ting-Jen Hsueh, Chien-Hua Peng, and Wei-Shou Chen. A transparent zno nanowire mems gas sensor prepared by an ito micro-heater. *Sensors and Actuators B: Chemical*, 304:127319, 2020. ISSN 0925-4005. URL `https://doi.org/10.1016/j.snb.2019.127319`.

[86] Changliang Hu, Shuang Xia, Hui Li, Tingguang Liu, Bangxin Zhou, Wenjue Chen, and Ning Wang. Improving the intergranular corrosion resistance of 304 stainless steel by grain boundary network control. *Corrosion science*, 53(5):1880–1886, 2011.

[87] Jie Hu and Min-Feng Yu. Meniscus-confined three-dimensional electrodeposition for direct writing of wire bonds. *Science*, 329(5989):313–316, 2010. URL `https://doi.org/10.1126/science.1190496`.

[88] Michael Huff. Recent advances in reactive ion etching and applications of high-aspect-ratio microfabrication. *Micromachines*, 12(8):991, 2021. URL `https://doi.org/10.3390/mi12080991`.

[89] Derek Hull and David J Bacon. *Introduction to dislocations*, volume 37. Elsevier, 2011. URL `https://doi.org/10.1016/C2009-0-64358-0`.

[90] Robert Ilic. Electron-beam lithography. April 2021. URL `https://www.nist.gov/programs-projects/electron-beam-lithography`.

[91] Peter J Imrich, Christoph Kirchlechner, Christian Motz, and Gerhard Dehm. Differences in deformation behavior of bicrystalline cu micropillars containing a twin boundary or a large-angle grain boundary. *Acta materialia*, 73:240–250, 2014.

[92] S. H. Kim A. I. Kingon J. A. Christman, H. Maiwa and R. J. Nemanich. Piezoelectric measurements with atomic force microscopy. *MRS Online Proceedings Library*, 1999541:617–622, 1998. URL `https://doi.org/10.1557/PROC-541-617`.

[93] Rong Fan Weitong Lin Xiaocui Li James Utama Surjadi, Xiaobin Feng and Yang Lu. Hollow medium-entropy alloy nanolattices with ultrahigh energy absorption and resilience. *NPG Asia Mater*, 13(36), 2021. URL `https://doi.org/10.1038/s41427-021-00306-y`.

[94] Dongchan Jang and Julia R. Greer. Transition from a strong-yet-brittle to a stronger-and-ductile state by size reduction of metallic glasses. *Nature Materials*, 9:215–219, 2010. URL `https://doi.org/10.1038/nmat2622`.

[95] Dongchan Jang, Xiaoyan Li, Huajian Gao, and Julia R Greer. Deformation mechanisms in nanotwinned metal nanopillars. *Nature nanotechnology*, 7(9):594–601, 2012. URL `tps://doi.org/10.1038/nnano.2012.116`.

[96] Farhan Javaid, Habib Pouriayevali, and Karsten Durst. Dislocation-grain boundary interactions: Recent advances on the underlying mechanisms studied via nanoindentation testing. *Journal of Materials Research*, 36(12):2545–2557, 2021. URL `https://doi.org/10.1557/s43578-020-00096-z`.

[97] Andrew T. Jennings and Julia R. Greer. Tensile deformation of electroplated copper nanopillars. *Philosophical Magazine*, 91(7-9):1108–1120, 2011. URL `https://doi.org/10.1080/14786435.2010.505180`.

[98] A.M. Johansen. Monte carlo methods. pages 296–303, 2010. URL `https://doi.org/10.1016/B978-0-08-044894-7.01543-8`.

[99] Surya R Kalidindi and Shraddha J Vachhani. Mechanical characterization of grain boundaries using nanoindentation. *Current Opinion in Solid State and Materials Science*, 18(4):196–204, 2014. URL `https://doi.org/10.1016/j.cossms.2014.05.002`.

[100] Ju-Young Kim and Julia R. Greer. Size-dependent mechanical properties of molybdenum nanopillars. *Applied Physics Letters*, 93(10):101916, 2008. URL `https://doi.org/10.1063/1.2979684`.

[101] Min-Woo Kim, Max L. Lifson, Rebecca A. Gallivan, Julia R. Greer, and Bong-Joong Kim. Recoverable electrical breakdown strength and dielectric constant in ultralow-k nanolattice capacitors. *Nano Letters*, 19(8):5689–5696, 2019. URL `https://doi.org/10.1021/acs.nanolett.9b02282`.

[102] PV Klimov, Julian Kelly, Z Chen, Matthew Neeley, Anthony Megrant, Brian Burkett, Rami Barends, Kunal Arya, Ben Chiaro, Yu Chen, et al. Fluctuations of energy-relaxation times in superconducting qubits. *Physical review letters*, 121(9):090502, 2018. URL `https://doi.org/10.1103/PhysRevLett.121.090502`.

[103] Shigeaki Kobayashi, Sadahiro Tsurekawa, and Tadao Watanabe. Grain boundary hardening and triple junction hardening in polycrystalline molybdenum. *Acta Materialia*, 53(4):1051–1057, 2005.

[104] Shigeaki Kobayashi, Sadahiro Tsurekawa, and Tadao Watanabe. A new approach to grain boundary engineering for nanocrystalline materials. *Beilstein Journal of Nanotechnology*, 7(1):1829–1849, 2016.

[105] Shun Kondo, Tasuku Mitsuma, Naoya Shibata, and Yuichi Ikuhara. Direct observation of individual dislocation interaction processes with grain boundaries. *Science advances*, 2(11):e1501926, 2016.

[106] Decheng Kong, Chaofang Dong, Shaolou Wei, Xiaoqing Ni, Liang Zhang, Ruixue Li, Li Wang, Cheng Man, and Xiaogang Li. About metastable cellular structure in additively manufactured austenitic stainless steels. *Additive Manufacturing*, 38: 101804, 2021.

[107] Sushil Kumar Kuanr, G Vinothkumar, and K Suresh Babu. Substrate temperature dependent structural orientation of ebpvd deposited nio films and its influence on optical, electrical property. *Materials Science in Semiconductor Processing*, 75: 26–30, 2018. URL `https://doi.org/10.1016/j.mssp.2017.11.013`.

[108] Sharvan Kumar. Dislocations: Complex and beautiful. *Journal of Materials*, 60(10): 5, 200.

[109] O.V. Kuzmin, Y.T. Pei, C.Q. Chen, and J.T.M. De Hosson. Intrinsic and extrinsic size effects in the deformation of metallic glass nanopillars. *Acta Materialia*, 60(3):889–898, 2012. ISSN 1359-6454. URL `https://doi.org/10.1016/j.actamat.2011.11.023`.

[110] AI Kuznetsov, R Kiyan, and BN Chichkov. Laser fabrication of 2d and 3d metal nanoparticle structures and arrays. *Optics express*, 18(20):21198–21203, 2010. URL `https://doi.org/10.1364/OE.18.021198`.

[111] Anthony Herman Fu-Hao Kwong. *Mechanical Properties of Small-Scale Sputtered Metallic Glasses*. PhD thesis, California Institute of Technology, 2020.

[112] Wei-Chiao Lai, Chun-Yueh Lin, Wei-Tse Chang, Po-Chang Li, Tsu-Yi Fu, Chia-Seng Chang, TT Tsong, and Shouh Hwang. Xenon gas field ion source from a single-atom tip. *Nanotechnology*, 28(25):255301, 2017. URL `https://doi.org/10.1088/1361-6528/aa6ed3`.

[113] Yann Le Bouar, Alphonse Finel, Benoît Appolaire, and Maeva Cottura. Chapter 13 - phase field models for modeling microstructure evolution in single-crystal ni-base superalloys. pages 379–399, 2022. URL `https://doi.org/10.1016/B978-0-12-819357-0.00022-6`.

[114] J. Lee, S. C. Nam, and Y. Tak. On the origin of electrodeposition mechanism of zno on ito substrate. *Korean J. Chem. Eng.*, 22:161, 2005.

[115] Pavel Lejcek. *Grain boundary segregation in metals*, volume 136. Springer Science & Business Media, 2010.

[116] Markku Leskelä and Mikko Ritala. Atomic layer deposition (ald): from precursors to thin film structures. *Thin Solid Films*, 409(1):138–146, 2002. ISSN 0040-6090. URL `https://doi.org/10.1016/S0040-6090(02)00117-7`. Proceedings of the 2nd Asian Conference on Chemical Vapour Depostion.

[117] G. Li, U. Aydemir, S. I. Morozov, S. A. Miller, Q. An, W. A. Goddard, P. Zhai, Q. Zhang, and G. J. Snyder. Mechanical properties in thermoelectric oxides: Ideal strength, deformation mechanism, and fracture toughness. *Acta Mater.*, 149:341, 2018.

[118] P Li and ZF Zhang. Standing wave effect and fractal structure in dislocation evolution. *Scientific reports*, 7(1):1–6, 2017.

[119] Xiaoyan Li, Ming Dao, Christoph Eberl, Andrea Maria Hodge, and Huajian Gao. Fracture, fatigue, and creep of nanotwinned metals. *MRS Bulletin*, 41(4):298–304, 2016. URL `https://doi.org/10.1557/mrs.2016.65`.

[120] Yan Li, Hang Zhang, Ruifeng Yang, Yohan Laffitte, Ulises Schmill, Wenhan Hu, Moufeed Kaddoura, Eric JM Blondeel, and Bo Cui. Fabrication of sharp silicon hollow microneedles by deep-reactive ion etching towards minimally invasive diagnostics. *Microsystems & nanoengineering*, 5(1):1–11, 2019. URL `https://doi.org/10.1038/s41378-019-0077-y`.

[121] Jan Philipp Liebig, Sebastian Krauß, Mathias Göken, and Benoit Merle. Influence of stacking fault energy and dislocation character on slip transfer at coherent twin boundaries studied by micropillar compression. *Acta Materialia*, 154:261–272, 2018.

[122] Max Louis Lifson. *Electromechanical Properties of 3D Multifunctional Nano-Architected Materials*. PhD thesis, California Institute of Technology, 2019.

[123] Y. Lin, G. Ehlert, and H. A. Sodano. Increased interface strength in carbon fiber composites through a zno nanowire interphase. *Adv. Funct. Mater.*, 19:2654, 2009.

[124] X. J. Liu, J. W. Li, Z. F. Zhou, L. W. Yang, Z. S. Ma, G. F. Xie, Y. Pan, and Chang Q. Sun. Size-induced elastic stiffening of zno nanostructures: Skin-depth energy pinning. *Applied Physics Letters*, 94(13):131902, 2009. URL `https://doi.org/10.1063/1.3109786`.

[125] Xueran Liu, Yongbing Liu, Xu Ran, Jian An, and Zhanyi Cao. Fabrication of the supersaturated solid solution of carbon in copper by mechanical alloying. *Materials Characterization*, 58(6):504–508, 2007.

[126] Zhiyuan Liu, Dandan Zhao, Pei Wang, Ming Yan, Can Yang, Zhangwei Chen, Jian Lu, and Zhaoping Lu. Additive manufacturing of metals: Microstructure evolution and multistage control. *Journal of Materials Science & Technology*, 100:224–236, 2022. URL `https://doi.org/10.1016/j.jmst.2021.06.011`.

[127] Zbigniew Łodziana, Nan-Yu Topsøe, and Jens K Nørskov. A negative surface energy for alumina. *Nature materials*, 3(5):289–293, 2004. URL `https://doi.org/10.1038/nmat1106`.

[128] K Lu. Stabilizing nanostructures in metals using grain and twin boundary architectures. *Nature Reviews Materials*, 1(5):1–13, 2016.

[129] Lei Lu, Yongfeng Shen, Xianhua Chen, Lihua Qian, and Ke Lu. Ultrahigh strength and high electrical conductivity in copper. *Science*, 304(5669):422–426, 2004.

[130] Song Lu, Qing-Miao Hu, Erna Krisztina Delczeg-Czirjak, Börje Johansson, and Levente Vitos. Determining the minimum grain size in severe plastic deformation process via first-principles calculations. *Acta materialia*, 60(11):4506–4513, 2012.

[131] Xiaochong Lu, Xu Zhang, Mingxing Shi, Franz Roters, Guozheng Kang, and Dierk Raabe. Dislocation mechanism based size-dependent crystal plasticity modeling and simulation of gradient nano-grained copper. *international Journal of Plasticity*, 113: 52–73, 2019.

[132] Xiyuan Lu, Gregory Moille, Ashutosh Rao, Daron Westly, and Kartik Srinivasan. On-chip optical parametric oscillation into the visible: generating red, orange, yellow, and green from a near-infrared pump. (7), 2020-10-12 00:10:00 2020. URL `https://doi.org/10.1364/OPTICA.393810`.

[133] Vlado A Lubarda. Dislocation burgers vector and the peach-koehler force: a review. *Journal of Materials Research and Technology*, 8(1):1550–1565, 2019.

[134] M. H. Malakooti, B. A. Patterson, H. Hwang, and H. A. Sodano. Zno nanowire interfaces for high strength multifunctional composites with embedded energy. *Energy Environ. Sci.*, 9:634, 2016.

[135] S. Maniv and A. Zangvil. Controlled texture of reactively rf-sputtered zno thin films. *Journal of Applied Physics*, 49(5):2787–2792, 1978. URL `https://doi.org/10.1063/1.325158`.

[136] PG Manusmare and HP Leighly Jr. Void-strengthening in aluminum and its nature. *Acta Metallurgica*, 24(11):1047–1052, 1976.

[137] Arturo J Mateos, Wei Huang, Yong-Wei Zhang, and Julia R Greer. Discrete-continuum duality of architected materials: failure, flaws, and fracture. *Advanced Functional Materials*, 29(5):1806772, 2019. URL `https://doi.org/10.1002/adfm.201806772`.

[138] Joachim Mayer, Lucille A Giannuzzi, Takeo Kamino, and Joseph Michael. Tem sample preparation and fib-induced damage. *MRS bulletin*, 32(5):400–407, 2007. URL `https://doi.org/10.1557/mrs2007.63`.

[139] Cameron McElfresh, Yinan Cui, Sergei L Dudarev, Giacomo Po, and Jaime Marian. Discrete stochastic model of point defect-dislocation interaction for simulating dislocation climb. *International Journal of Plasticity*, 136:102848, 2021.

[140] João M Medeiros, Désirée Böck, and Martin Pilhofer. Imaging bacteria inside their host by cryo-focused ion beam milling and electron cryotomography. *Current Opinion in Microbiology*, 43:62–68, 2018. ISSN 1369-5274. URL `https://doi.org/10.1016/j.mib.2017.12.006`. Environmental Microbiology * The New Microscopy.

[141] Lucas R. Meza, Satyajit Das, and Julia R. Greer. Strong, lightweight, and recoverable three-dimensional ceramic nanolattices. *Science*, 345(6202):1322–1326, 2014. URL `https://doi.org/10.1126/science.1255908`.

[142] Bedabibhas Mohanty, Kalpana S Katti, Dinesh R Katti, and Devendra Verma. Dynamic nanomechanical response of nacre. *Journal of Materials Research*, 21(8): 2045–2051, 2006. URL `https://doi.org/10.1557/jmr.2006.0247`.

[143] K. Momeni, Gregory M. Odegard, and Reza S. Yassar. Finite size effect on the piezoelectric properties of zno nanobelts: A molecular dynamics approach. *Acta Materialia*, 60(13):5117–5124, 2012. ISSN 1359-6454. URL `https://doi.org/10.1016/j.actamat.2012.06.041`.

[144] A. K. Mukhopadhyay, M. Ray Chaudhuri, A. Seal, S. K. Dalui, M. Banerjee, and K. K. Phani. Mechanical characterization of microwave sintered zinc oxide. *Bull. Mater. Sci.*, 24:125, 2001.

[145] B. P. Nabar, Z. Celik-Butler, and D. P. Butler. Self-powered tactile pressure sensors using ordered crystalline zno nanorods on flexible substrates toward robotic skin and garments. *IEEE Sens. J.*, 15:63, 2015.

[146] Sneha N Naik and Stephen M Walley. The hall-petch and inverse hall-petch relations and the hardness of nanocrystalline metals. *Journal of Materials Science*, 55(7): 2661–2681, 2020. URL `https://doi.org/10.1007/s10853-019-04160-w`.

[147] Mats Nyberg, Martin A. Nygren, Lars G. M. Pettersson, David H. Gay, and Andrew L. Rohl. Hydrogen dissociation on reconstructed zno surfaces. *The Journal of Physical Chemistry*, 100(21):9054–9063, 1996. URL `https://doi.org/10.1021/jp953704h`.

[148] Fumiyasu Oba, Isao Tanaka, Shigeto R. Nishitani, Hirohiko Adachi, Ben Slater, and David H. Gay. Geometry and electronic structure of [0001]/(1230) $\sigma = 7$ symmetric tilt boundary in zno. *Philosophical Magazine A*, 80(7):1567–1581, 2000. URL `https://doi.org/10.1080/01418610008212136`.

[149] Milton Ohring. *Engineering materials science*. Elsevier, 1995. URL `https://doi.org/10.1016/B978-0-12-524995-9.X5023-5`.

[150] Warren Carl Oliver and George Mathews Pharr. An improved technique for determining hardness and elastic modulus using load and displacement sensing indentation experiments. *Journal of materials research*, 7(6):1564–1583, 1992. URL `https://doi.org/10.1557/JMR.1992.1564`.

[151] Chin Boon Ong, Law Yong Ng, and Abdul Wahab Mohammad. A review of zno nanoparticles as solar photocatalysts: Synthesis, mechanisms and applications. *Renewable and Sustainable Energy Reviews*, 81:536–551, 2018. ISSN 1364-0321. URL `https://doi.org/10.1016/j.rser.2017.08.020`.

[152] M Serdar Onses, Erick Sutanto, Placid M Ferreira, Andrew G Alleyne, and John A Rogers. Mechanisms, capabilities, and applications of high-resolution electrohydrodynamic jet printing. *Small*, 11(34):4237–4266, 2015. URL `https://doi.org/10.1002/smll.201500593`.

[153] E Orowan. Zur kristallplastizität. iii. *Zeitschrift für Physik*, 89(9):634–659, 1934.

[154] Fredrik Östlund, Philip R Howie, Rudy Ghisleni, Sandra Korte, Klaus Leifer, William J Clegg, and Johann Michler. Ductile-brittle transition in micropillar compression of gaas at room temperature. *Philosophical Magazine*, 91(7-9):1190–1199, 2011.

[155] Chandra Shekhar Pande, BB Rath, and MA Imam. Effect of annealing twins on hall-petch relation in polycrystalline materials. *Materials Science and Engineering: A*, 367(1-2):171–175, 2004.

[156] M Peach and JS395370039 Koehler. The forces exerted on dislocations and the stress fields produced by them. *Physical Review*, 80(3):436, 1950.

[157] Rudolf Peierls. The size of a dislocation. *Proceedings of the Physical Society (1926-1948)*, 52(1):34, 1940.

[158] NJ Petch. The cleavage strength of polycrystals. *Journal of the iron and steel institute*, 174:25–28, 1953.

[159] Alberto Pique, Raymond CY Auyeung, Heungsoo Kim, Kristin M Metkus, and Scott A Mathews. Digital microfabrication by laser decal transfer. *J. Laser Micro/Nanoeng*, 3(3):163–169, 2008. URL `https://doi.org/10.2961/JLMN.2008.03.0007`.

[160] Michael Polanyi. Über eine art gitterstörung, die einen kristall plastisch machen könnte. *Zeitschrift für Physik*, 89(9):660–664, 1934.

[161] Carlos M Portela, Bryce W Edwards, David Veysset, Yuchen Sun, Keith A Nelson, Dennis M Kochmann, and Julia R Greer. Supersonic impact resilience of nanoarchitected carbon. *Nature Materials*, 20(11):1491–1497, 2021.

[162] Agnieszka Priebe, Ivo Utke, Laszlo Pethö, and Johann Michler. Application of a gas-injection system during the fib-tof-sims analysis—influence of water vapor and fluorine gas on secondary ion signals and sputtering rates. *Analytical Chemistry*, 91(18):11712–11722, 2019. URL `https://doi.org/10.1021/acs.analchem.9b02287`.

[163] Y. S. Puzyrev, X. Shen, C. X. Zhang, J. Hachtel, K. Ni, B. K. Choi, E.-X. Zhang, O. Ovchinnikov, R. D. Schrimpf, D. M. Fleetwood, and S. T. Pantelides. Memristive devices from zno nanowire bundles and meshes. *Appl. Phys. Lett.*, 111:153504, 2017.

[164] D. Raymand, A. C. T. van Duin, M. Baudin, and K. A. Hermansson. Reactive force field (reaxff) for zinc oxide. *Surf. Sci.*, 602:1020, 2008.

[165] Hossein Abdizadeh Reza Ebrahimifard and Mohammad Reza Golobostanfard. Controlling the extremely preferred orientation texturing of sol–gel derived zno thin films with sol and heat treatment parameters. *Journal of Sol-Gel Science and Technology volume*, 93:28–35, 2020. URL `https://doi.org/10.1007/s10971-019-05157-2`.

[166] C. A. D. Rodriguez and G. Tremiliosi-Filho. Electrochemical deposition. *Encyclopedia of Tribology*, pages 918–922, 2013. URL `https://doi.org/10.1007/978-0-387-92897-5_700`.

[167] A. Roy, J. Mead, S. Wang, and H. Huang. Effects of surface defects on the mechanical properties of zno nanowires. *Sci. Rep.*, 7:9547, 2017.

[168] T. K. Roy. Assessing hardness and fracture toughness in sintered zinc oxide ceramics through indentation technique. *Mater. Sci. Eng., A*, 640:267, 2015.

[169] Tapatee Kundu Roy, Debasis Bhowmick, Dirtha Sanyal, and Alok Chakrabarti. Sintering studies of nano-crystalline zinc oxide. *Ceramics International*, 34(1):81–87, 2008.

[170] Max Saccone, Rebecca A Gallivan, Kai Narita, Daryl W Yee, and Julia R Greer. Microscale fabrication of 3d multicomponent metals via hydrogel infusion. 2022. URL `https://doi.org/10.21203/rs.3.rs-1108933/v1`.

[171] Ranjana Saha and William D Nix. Effects of the substrate on the determination of thin film mechanical properties by nanoindentation. *Acta materialia*, 50(1):23–38, 2002. URL `https://doi.org/10.1016/S1359-6454(01)00328-7`.

[172] K.M. Sandeep, Shreesha Bhat, and S.M. Dharmaprakash. Structural, optical, and led characteristics of zno and al doped zno thin films. *Journal of Physics and Chemistry of Solids*, 104:36–44, 2017. ISSN 0022-3697. URL `https://doi.org/10.1016/j.jpcs.2017.01.003`.

[173] Christopher A Schuh, Mukul Kumar, and Wayne E King. Universal features of grain boundary networks in fcc materials. *Journal of materials science*, 40(4):847–852, 2005.

[174] A. V. Sergueeva, N. A. Mara, N. A. Krasilnikov, R. Z. Valiev, and A. K. Mukherjee. Cooperative grain boundary sliding in nanocrystalline materials. *Philosophical Magazine*, 86(36):5797–5804, 2006. URL `https://doi.org/10.1080/14786430600764906`.

[175] Jiazhen Sheng, Ki-Lim Han, TaeHyun Hong, Wan-Ho Choi, and Jin-Seong Park. Review of recent progresses on flexible oxide semiconductor thin film transistors based on atomic layer deposition processes. *Journal of Semiconductors*, 39(1): 011008, 2018. URL `https://doi.org/10.1080/15980316.2017.1385544`.

[176] David S Sholl and Janice A Steckel. *Density functional theory: a practical introduction*. John Wiley & Sons, 2011. ISBN 978-0-470-37317-0.

[177] Mark A Skylar-Scott, Suman Gunasekaran, and Jennifer A Lewis. Laser-assisted direct ink writing of planar and 3d metal architectures. *Proceedings of the National Academy of Sciences*, 113(22):6137–6142, 2016. URL `https://doi.org/10.1073/pnas.1525131113`.

[178] R Smoluchowski. Theory of grain boundary diffusion. *Physical Review*, 87(3):482, 1952.

[179] F. Song, G.L. Huang, H.S. Park, and X.N. Liu. A continuum model for the mechanical behavior of nanowires including surface and surface-induced initial stresses. *International Journal of Solids and Structures*, 48(14):2154–2163, 2011. ISSN 0020-7683. URL `https://doi.org/10.1016/j.ijsolstr.2011.03.021`.

[180] Francesco Stellacci, Christina A Bauer, Timo Meyer-Friedrichsen, Wim Wenseleers, Valérie Alain, Stephen M Kuebler, Stephanie JK Pond, Yadong Zhang, Seth R Marder, and Joseph W Perry. Laser and electron-beam induced growth of nanoparticles for 2d and 3d metal patterning. *Advanced Materials*, 14(3):194–198, 2002. URL `https://doi.org/10.1002/1521-4095(20020205)14:3<194::AID-ADMA194>3.0.CO;2-W`.

[181] Eva-Maria Steyskal, Bernd Oberdorfer, Wolfgang Sprengel, Michael Zehetbauer, Reinhard Pippan, and Roland Würschum. Direct experimental determination of grain boundary excess volume in metals. *Physical review letters*, 108(5):055504, 2012.

[182] Tom Strangman, Derek Raybould, Ahsan Jameel, and Wil Baker. Damage mechanisms, life prediction, and development of eb-pvd thermal barrier coatings for turbine airfoils. *Surface and Coatings Technology*, 202(4-7):658–664, 2007. URL `https://doi.org/10.1016/j.surfcoat.2007.06.067`.

[183] Alexander Stukowski. Visualization and analysis of atomistic simulation data with OVITO–the open visualization tool. *Modelling and Simulation in Materials Science and Engineering*, 18(1):015012, dec 2009. URL `https://doi.org/10.1088/0965-0393/18/1/015012`.

[184] Takanari Takai, Hidenobu Nakao, and Futoshi Iwata. Three-dimensional microfabrication using local electrophoresis deposition and a laser trapping technique. *Optics express*, 22(23):28109–28117, 2014. URL `https://doi.org/10.1364/OE.22.028109`.

[185] Yemin Tang, Amin Sandoughsaz, Kevin J Owen, and Khalil Najafi. Ultra deep reactive ion etching of high aspect-ratio and thick silicon using a ramped-parameter process. *Journal of Microelectromechanical Systems*, 27(4):686–697, 2018. URL `https://doi.org/10.1109/JMEMS.2018.2843722`.

[186] Geoffrey Ingram Taylor. The mechanism of plastic deformation of crystals. part i.—theoretical. *Proceedings of the Royal Society of London. Series A, Containing Papers of a Mathematical and Physical Character*, 145(855):362–387, 1934.

[187] AP Ternovsky, VP Alekhin, MH Shorshorov, MM Khrushchov, and VN Skvortsov. Micromechanical testing of materials by depression. *Ind. Lab.*, 39(10):1620–1624, 1973.

[188] Ottman A Tertuliano, Bryce W Edwards, Lucas R Meza, Vikram S Deshpande, and Julia R Greer. Nanofibril-mediated fracture resistance of bone. *Bioinspiration & Biomimetics*, 16(3):035001, 2021. URL `https://doi.org/10.1088/1748-3190/abdd9d`.

[189] Michael D Uchic and Dennis M Dimiduk. A methodology to investigate size scale effects in crystalline plasticity using uniaxial compression testing. *Materials Science and Engineering: A*, 400:268–278, 2005. URL `https://doi.org/10.1016/j.msea.2005.03.082`.

[190] Ivo Utke, Patrik Hoffmann, and John Melngailis. Gas-assisted focused electron beam and ion beam processing and fabrication. *Journal of Vacuum Science & Technology B: Microelectronics and Nanometer Structures Processing, Measurement, and Phenomena*, 26(4):1197–1276, 2008. URL `https://doi.org/10.1116/1.2955728`.

[191] Aditad Vasinonta and Jack L Beuth. Measurement of interfacial toughness in thermal barrier coating systems by indentation. *Engineering Fracture Mechanics*, 68(7):843–860, 2001. URL `https://doi.org/10.1016/S0013-7944(00)00130-2`.

[192] C. A. Volkert, A. Donohue, and F. Spaepen. Effect of sample size on deformation in amorphous metals. *Journal of Applied Physics*, 103(8):083539, 2008. URL `https://doi.org/10.1063/1.2884584`.

[193] Chao Wang, Md Emran Hossain Bhuiyan, Salvador Moreno, and Majid Minary-Jolandan. Direct-write printing copper-nickel (cu/ni) alloy with controlled composition from a single electrolyte using co-electrodeposition. *ACS applied materials & interfaces*, 12(16):18683–18691, 2020.

[194] Guofeng Wang and Xiaodong Li. Size dependency of the elastic modulus of zno nanowires: Surface stress effect. *Applied Physics Letters*, 91(23):231912, 2007. URL `https://doi.org/10.1063/1.2821118`.

[195] Peng Wang, Fengxian Liu, Yinan Cui, Zhanli Liu, Shaoxing Qu, and Zhuo Zhuang. Interpreting strain burst in micropillar compression through instability of loading system. *International Journal of Plasticity*, 107:150–163, 2018. ISSN 0749-6419. URL `https://doi.org/10.1016/j.ijplas.2018.04.002`.

[196] Wei-hua Wang, Yang Wang, Guo-yang Shu, Shi-shu Fang, Jie-cai Han, Bing Dai, and Jia-qi Zhu. Recent progress on controlling dislocation density and behavior during heteroepitaxial single crystal diamond growth. *New Carbon Materials*, 36(6):1034–1045, 2021. URL `https://doi.org/10.1016/S1872-5805(21)60096-3`.

[197] Shin-Pon Ju Meng-Hsiung Weng Wen-Jay Lee, Jee-Gong Chang and Chia-Hung Lee. Structure-dependent mechanical properties of ultrathin zinc oxide nanowires. *Nanoscale Research Letters*, 6(352), 2011. URL `https://doi.org/10.1186/1556-276X-6-352`.

[198] JM Wheeler and J Michler. Invited article: Indenter materials for high temperature nanoindentation. *Review of Scientific Instruments*, 84(10):101301, 2013. URL `https://doi.org/10.1063/1.4824710`.

[199] J. G. Williams. Large displacement and end block effects in the 'dcb' interlaminar test in modes i and ii. *J. Compos. Mater.*, 21:330, 1987.

[200] ZX Wu, YW Zhang, and DJ Srolovitz. Dislocation—twin interaction mechanisms for ultrahigh strength and ductility in nanotwinned metals. *Acta Materialia*, 57(15): 4508–4518, 2009.

[201] Xiaoxing Xia, Claudio V Di Leo, X Wendy Gu, and Julia R Greer. In situ lithiation-delithiation of mechanically robust cu-si core-shell nanolattices in a scanning electron microscope. *ACS Energy Letters*, 1(3):492–499, 2016. URL `https://doi.org/10.1021/acsenergylett.6b00256`.

[202] F. Xu, Q. Qin, A. Mishra, Y. Gu, and Y. Zhu. Mechanical properties of zno nanowires under different loading modes. *Nano Res.*, 3:271, 2010.

[203] Lifen Xu, Yi Guo, Qing Liao, Jianping Zhang, and Dongsheng Xu. Morphological control of zno nanostructures by electrodeposition. *The Journal of Physical Chemistry B*, 109(28):13519–13522, 2005. URL `https://doi.org/10.1021/jp051007b`.

[204] S. Xu and Z. L. Wang. One-dimensional zno nanostructures: Solution growth and functional properties. *Nano Res.*, 4:1013, 2011.

[205] MK Yaakob, NH Hussin, MFM Taib, TIT Kudin, OH Hassan, AMM Ali, and MZA Yahya. First principles lda+ u calculations for zno materials. *Integrated Ferroelectrics*, 155(1):15–22, 2014. URL `https://doi.org/10.1080/10584587.2014.905086`.

[206] Takashi Yamamoto, Tadashi Shiosaki, and Akira Kawabata. Characterization of zno piezoelectric films prepared by rf planar-magnetron sputtering. *Journal of Applied Physics*, 51(6):3113–3120, 1980. URL `https://doi.org/10.1063/1.328100`.

[207] Yanfa Yan, M. M. Al-Jassim, M. F. Chisholm, L. A. Boatner, S. J. Pennycook, and M. Oxley. $[1\bar{1}00](1102)$ twin boundaries in wurtzite ZnO and group-iii-nitrides. *Phys. Rev. B*, 71:041309, Jan 2005. URL `https://doi.org/10.1103/PhysRevB.71.041309`.

[208] F. Yang. Surface effect on the nanowire forest indentation. *Strength Mater.*, 50:116, 2018.

[209] Daryl W Yee, Max L Lifson, Bryce W Edwards, and Julia R Greer. Additive manufacturing of 3d-architected multifunctional metal oxides. *Advanced Materials*, 31(33):1901345, 2019. URL `https://doi.org/10.1002/adma.201901345`.

[210] Daryl W Yee, Michael A Citrin, Zane W Taylor, Max A Saccone, Victoria L Tovmasyan, and Julia R Greer. Hydrogel-based additive manufacturing of lithium cobalt oxide. *Advanced Materials Technologies*, 6(2):2000791, 2021. URL `https://doi.org/10.1002/admt.202000791`.

[211] Daryl Wei Liang Yee. *Additive Manufacturing of 3D Functional Materials: From Surface Chemistry to Combustion-Derived Materials*. PhD thesis, California Institute of Technology, 2020.

[212] B. Yeom, T. Sain, N. Lacevic, D. Bukharina, S. H. Cha, A. M. Waas, E. M. Arruda, and N. A. Kotov. Abiotic tooth enamel. *Nature*, 543:95, 2017.

[213] T. Yoshida, D. Komatsu, N. Shimokawa, and H. Minoura. Mechanism of cathodic electrodeposition of zinc oxide thin films from aqueous zinc nitrate baths. *Thin Solid Films*, 451–452:166, 2004.

[214] S. J. Young, L. W. Ji, S. J. Chang, T. H. Fang, T. J. Hsueh, T. H. Meen, and I. C. Chen. Nanoscale mechanical characteristics of vertical zno nanowires grown on zno:ga/glass templates. *Nanotechnology*, 18:225603, 2007.

[215] H. Yu, J. Liu, X. Fan, W. Yan, L. Han, J. Han, X. Zhang, T. Hong, and Z. Liu. Bionic micro-nano-bump-structures with a good self-cleaning property: The growth of zno nanoarrays modified by polystyrene spheres. *Mater. Chem. Phys.*, 170:52, 2016.

[216] Michael J Zachman, Zhengyuan Tu, Snehashis Choudhury, Lynden A Archer, and Lena F Kourkoutis. Cryo-stem mapping of solid-liquid interfaces and dendrites in lithium-metal batteries. *Nature*, 560(7718):345–349, 2018. URL `https://doi.org/10.1038/s41586-018-0397-3`.

[217] Michael Zenou, Amir Sa'ar, and Zvi Kotler. Laser transfer of metals and metal alloys for digital microfabrication of 3d objects. *Small*, 11(33):4082–4089, 2015. URL `https://doi.org/10.1002/smll.201500612`.

[218] Liang Zhang, Cheng Lu, and Kiet Tieu. A review on atomistic simulation of grain boundary behaviors in face-centered cubic metals. *Computational Materials Science*, 118:180–191, 2016.

[219] Xu Zhang, Songjiang Lu, Bo Zhang, Xiaobao Tian, Qianhua Kan, and Guozheng Kang. Dislocation—grain boundary interaction-based discrete dislocation dynamics modeling and its application to bicrystals with different misorientations. *Acta Materialia*, 202:88–98, 2021. URL `https://doi.org/10.1016/j.actamat.2020.10.052`.

[220] Zhengrong Zhang and Liying Jiang. Size effects on electromechanical coupling fields of a bending piezoelectric nanoplate due to surface effects and flexoelectricity. *Journal of Applied Physics*, 116(13):134308, 2014.

[221] Wenzhuo Zhao and Yu Duan. Advanced applications of atomic layer deposition in perovskite-based solar cells. *Advanced Photonics Research*, 2(7):2100011, 2021. URL `https://doi.org/10.1002/adpr.202100003`.

[222] Hui Zheng, Xiang-Guo Li, Richard Tran, Chi Chen, Matthew Horton, Donald Winston, Kristin Aslaug Persson, and Shyue Ping Ong. Grain boundary properties of elemental metals. *Acta Materialia*, 186:40–49, 2020.

[223] Jingxu Zheng, Mun Sek Kim, Zhengyuan Tu, Snehashis Choudhury, Tian Tang, and Lynden A Archer. Regulating electrodeposition morphology of lithium: towards commercially relevant secondary li metal batteries. *Chemical Society Reviews*, 49 (9):2701–2750, 2020. URL `https://doi.org/10.1039/C9CS00883G`.

[224] Qiang Zheng, Bojing Shi, Zhou Li, and Zhong Lin Wang. Recent progress on piezoelectric and triboelectric energy harvesters in biomedical systems. *Advanced Science*, 4(7):1700029, 2017. URL `https://doi.org/10.1002/advs.201700029`.

[225] Qiang Zheng, Bojing Shi, Zhou Li, and Zhong Lin Wang. Recent progress on piezoelectric and triboelectric energy harvesters in biomedical systems. *Advanced Science*, 4(7):1700029, 2017.

[226] SN Zhevnenko, IS Petrov, D Scheiber, and VI Razumovskiy. Surface and segregation energies of ag based alloys with ni, co and fe: Direct experimental measurement and dft study. *Acta Materialia*, 205:116565, 2021. URL `https://doi.org/10.1016/j.actamat.2020.116565`.

[227] Kehua Zhong, Ruina Hu, Guigui Xu, Yanmin Yang, Jian-Min Zhang, and Zhigao Huang. Adsorption and ultrafast diffusion of lithium in bilayer graphene: Ab initio and kinetic monte carlo simulation study. *Physical Review B*, 99(15):155403, 2019. URL `https://doi.org/10.1103/PhysRevB.99.155403`.

[228] Xiangli Zhong, C Austin Wade, Philip J Withers, Xiaorong Zhou, Changrun Cai, Sarah J Haigh, and M Grace Burke. Comparing xe+ pfib and ga+ fib for tem sample preparation of al alloys: Minimising fib-induced artefacts. *Journal of Microscopy*, 282(2):101–112, 2021. URL `https://doi.org/10.1111/jmi.12983`.

[229] Linli Zhu, Haihui Ruan, Xiaoyan Li, Ming Dao, Huajian Gao, and Jian Lu. Modeling grain size dependent optimal twin spacing for achieving ultimate high strength and related high ductility in nanotwinned metals. *Acta Materialia*, 59(14):5544–5557, 2011.

[230] Rong Zhu, Dingqu Wang, Shaoqing Xiang, Zhaoying Zhou, and Xiongying Ye. Piezoelectric characterization of a single zinc oxide nanowire using a nanoelectromechanical oscillator. *Nanotechnology*, 19(28):285712, jun 2008. URL `https://doi.org/10.1088/0957-4484/19/28/285712`.

[231] Fredrik Östlund, Karolina Rzepiejewska-Malyska, Klaus Leifer, Lucas M. Hale, Yuye Tang, Roberto Ballarini, William W. Gerberich, and Johann Michler. Brittle-to-ductile transition in uniaxial compression of silicon pillars at room temperature. *Advanced Functional Materials*, 19(15):2439–2444, 2009. URL `https://doi.org/10.1002/adfm.200900418`.

Appendix A

ADDITIVE MANUFACTURING TECHNIQUES AT THE MICRO- AND NANO-SCALE

Method	Precursor	References
Photolithography	Polymeric Resin	[3, 10, 14–16]
Electrophoretic deposition	nanoparticle suspension	[12]
Photoreduction	metal salt solution	[2, 2]
Forward transfer	nanoparticle paste	[7, 9, 17]
Induced deposition or Ion Beam	precursor gas	[13]
Direct Ink Writing	nanoparticles	[1, 11]
Local Ion Electroplating	salt solution	[5]
Meniscus-confined electroplating	salt solution	[6]
Electrohydrodynamic printing	nanoparticle suspension	[4, 8]

Table A.1: **Details and References for Micro- and Nano-scale AM Techniques.** Precursor refers to the resin or pre-printing materials that are transformed into the 3D structure. Note that reference numbering is specific to this appendix.

BIBLIOGRAPHY

[1] Bok Y Ahn, Eric B Duoss, Michael J Motala, Xiaoying Guo, Sang-Il Park, Yujie Xiong, Jongseung Yoon, Ralph G Nuzzo, John A Rogers, and Jennifer A Lewis. Omnidirectional printing of flexible, stretchable, and spanning silver microelectrodes. *Science*, 323(5921):1590–1593, 2009. URL `https://doi.org/10.1126/science.1168375`.

[2] Yao-Yu Cao, Nobuyuki Takeyasu, Takuo Tanaka, Xuan-Ming Duan, and Satoshi Kawata. 3d metallic nanostructure fabrication by surfactant-assisted multiphoton-induced reduction. *Small*, 5(10):1144–1148, 2009. URL `https://doi.org/10.1002/smll.200801179`.

[3] Marco Carlotti and Virgilio Mattoli. Functional materials for two-photon polymerization in microfabrication. *Small*, 15(40):1902687, 2019.

[4] Patrick Galliker, Julian Schneider, Hadi Eghlidi, Stefan Kress, Vahid Sandoghdar, and Dimos Poulikakos. Direct printing of nanostructures by electrostatic autofocussing of ink nanodroplets. *Nature communications*, 3(1):1–9, 2012. URL `https://doi.org/10.1038/ncomms1891`.

[5] Luca Hirt, Stephan Ihle, Zhijian Pan, Livie Dorwling-Carter, Alain Reiser, Jeffrey M Wheeler, Ralph Spolenak, János Vörös, and Tomaso Zambelli. Template-free 3d microprinting of metals using a force-controlled nanopipette for layer-by-layer electrodeposition. *Advanced materials*, 28(12):2311–2315, 2016. URL `https://doi.org/10.1002/adma.201504967`.

[6] Jie Hu and Min-Feng Yu. Meniscus-confined three-dimensional electrodeposition for direct writing of wire bonds. *Science*, 329(5989):313–316, 2010. URL `https://doi.org/10.1126/science.1190496`.

[7] AI Kuznetsov, R Kiyan, and BN Chichkov. Laser fabrication of 2d and 3d metal nanoparticle structures and arrays. *Optics express*, 18(20):21198–21203, 2010. URL `https://doi.org/10.1364/OE.18.021198`.

[8] M Serdar Onses, Erick Sutanto, Placid M Ferreira, Andrew G Alleyne, and John A Rogers. Mechanisms, capabilities, and applications of high-resolution electrohydrodynamic jet printing. *Small*, 11(34):4237–4266, 2015. URL `https://doi.org/10.1002/smll.201500593`.

[9] Alberto Pique, Raymond CY Auyeung, Heungsoo Kim, Kristin M Metkus, and Scott A Mathews. Digital microfabrication by laser decal transfer. *J. Laser Micro/Nanoeng*, 3 (3):163–169, 2008. URL `https://doi.org/10.2961/JLMN.2008.03.0007`.

[10] Max Saccone, Rebecca A Gallivan, Kai Narita, Daryl W Yee, and Julia R Greer. Microscale fabrication of 3d multicomponent metals via hydrogel infusion. 2022. URL `https://doi.org/10.21203/rs.3.rs-1108933/v1`.

[11] Mark A Skylar-Scott, Suman Gunasekaran, and Jennifer A Lewis. Laser-assisted direct ink writing of planar and 3d metal architectures. *Proceedings of the National Academy of Sciences*, 113(22):6137–6142, 2016. URL `https://doi.org/10.1073/pnas.1525131113`.

[12] Takanari Takai, Hidenobu Nakao, and Futoshi Iwata. Three-dimensional microfabrication using local electrophoresis deposition and a laser trapping technique. *Optics express*, 22(23):28109–28117, 2014. URL `https://doi.org/10.1364/OE.22.028109`.

[13] Ivo Utke, Patrik Hoffmann, and John Melngailis. Gas-assisted focused electron beam and ion beam processing and fabrication. *Journal of Vacuum Science & Technology B: Microelectronics and Nanometer Structures Processing, Measurement, and Phenomena*, 26(4):1197–1276, 2008. URL `https://doi.org/10.1116/1.2955728`.

[14] Andrey Vyatskikh, Stéphane Delalande, Akira Kudo, Xuan Zhang, Carlos M Portela, and Julia R Greer. Additive manufacturing of 3d nano-architected metals. *Nature communications*, 9(1):1–8, 2018.

[15] Daryl W Yee, Max L Lifson, Bryce W Edwards, and Julia R Greer. Additive manufacturing of 3d-architected multifunctional metal oxides. *Advanced Materials*, 31(33): 1901345, 2019. URL `https://doi.org/10.1002/adma.201901345`.

[16] Daryl W Yee, Michael A Citrin, Zane W Taylor, Max A Saccone, Victoria L Tovmasyan, and Julia R Greer. Hydrogel-based additive manufacturing of lithium cobalt oxide. *Advanced Materials Technologies*, 6(2):2000791, 2021. URL `https://doi.org/10.1002/admt.202000791`.

[17] Michael Zenou, Amir Sa'ar, and Zvi Kotler. Laser transfer of metals and metal alloys for digital microfabrication of 3d objects. *Small*, 11(33):4082–4089, 2015. URL `https://doi.org/10.1002/smll.201500612`.

Appendix B

DISLOCATIONS: COMPLEX AND BEAUTIFUL

Taylor, Polanyi, and Orowan in 1934,
Identified a dislocation not known before,
In a perfect crystal, they were minor defects
Linear in dimension, but with profound effects

Burgers then defined their vector
Be they screw or edge in character.
Bragg and Nye used many a soap bubble
To view these dislocations with little trouble,

Peierls and Nabarro dug a bit more
And found the energy associated with the core.
Vitek and Duesbery, the core of the bcc screw
Dissected and confirmed, non-planarity is true.

When stressed excessively, they climb and glide
As they gracefully enable slip and slide
In great numbers they march out from a Frank–Read source
And then they really are a tour de force

Cottrell and Bilby examined their lineage
And proclaimed they knew how they strain-age,
While Eshelby, Bacon, Koehler and Peach
With elegant physics their interactions, did teach

Their split personality Shockley found
In silver and gold, where many faults they bound
Cockayne first analyzed them in the dark
His approach, in science books, left a mark

The poem is written by Dr. Sharvan Kumar and published in the Journal of Materials [1].

BIBLIOGRAPHY

[1] Sharvan Kumar. Dislocations: Complex and beautiful. *Journal of Materials*, 60(10):5, 200.

Appendix C

ADDITIONAL NOTES ON MICROCROMPESSION TESTING

C.1 Sneddon Correction

When calculating the true stiffness of a pillar or pillar-like structure during compression, one needs to take into account the added compliance of the substrate which the structure is being compressed into. If the substrate, like the indentor tip, is significantly stiffer than the measured material, the added compliance of the substrate is negligible and can be disregarded. The stiffness of the substrate ($S_{Sneddon}$) can be calculated using the solution for indentation of a rigid circular flat punch indenting into an isotropic elastic half space [1]:

$$S_{Sneddon} = \left(\frac{\sqrt{\pi}\left(1 - \nu^2\right)}{2E_{substrate}\sqrt{A_i}} \right)^{-1} \tag{C.1}$$

where $E_{substrate}$ is the elastic modulus of the substrate in the direction of compression, A_i is the instantaneous cross-sectional area of the pillar-like structure that is indenting into the substrate, and ν is the Poisson's ratio of the substrate.

After obtaining the Sneddon stiffness, one can calculated the true stiffness of the pillar (S_{pillar}) through the following relationship which treats the pillar and substrate as springs in series:

$$S_{pillar} = \left(S_{meas}^{-1} - S_{Sneddon}^{-1} \right)^{-1} \tag{C.2}$$

with S_{meas} as the measured stiffness of the pillar. As a point of comparison we can use the theoretical stiffness of the pillar ($S_{pillar,theory}$) to identify the magnitude of contribution from the substrate. Theoretical stiffness is given as:

$$S_{pillar,theory} = \frac{E_{theory} A_i}{l_i} \tag{C.3}$$

where E_{theory} as the theoretical elastic modulus of the pillar and l_i as the height of the pillar. Table C.1 shows these calculated values for all nanomechanical pillar-like compressions discussed in this work.

Test	Substrate	$S_{Sneddon}(N/m)$	$S_{pillar,theory}$ (N/m)
ZnO Bundle (2µm)	Au	1.9 x 10^5	7.3 x 10^4
ZnO Bundle (4µm)	Au	3.8 x 10^5	2.9 x 10^5
ZnO Pillar (300 nm)	Si	6.1 x 10^4	9.4 x 10^3
ZnO Pillar (5µm)	Si	1.0 x 10^6	3.1 x 10^5

Table C.1: **Sneddon and Theoretical Stiffness** Calculations for the Sneddon correction and Theoetical Stiffness corresponding to all pillar-like nanomechanical compressions performed in this work.

C.2 Displacement Bursts, Load Drops, and other Nanomechanical Features

When assessing nanomechanical testing, a common feature observed is a displacement burst or load drop. These are both due to the material undergoing some sudden stress relaxation event but manifest differently based on differences in the type of loading feedback. A load drop occurs when the system is tracking the load associated with a particular displacement. The material has load reapplied at that displacement leading to the characteristic drops in the data. Displacement bursts occur when the system tracks displacement at particular load. The material load continues to be applied from this new position. Some systems see downward slopes in the burst region with the load after the burst as lower than that before the burst. This has been identified as an instrumentation artifact and not a physically relevant phenomena. These burst/drop features are typically associated with dislocation avalanches or sudden cascading motion of dislocations. Once an activation barrier is overcome for plastic deformation, these events have a relatively stochastic behavior based on the distribution of defects and sources in the material. However any form of stress relaxation can give rise to these distinct excursions including grain boundary motion, cracks, or pore collapse.

When using CSM data as a method for identifying contact and alignment in the material, the expected response is a sudden rise in the stiffness as the tip comes in contact with the top surface of the structure. Once contact is made, the stiffness should be with 10% of the theoretical stiffness predicted from the elastic modulus and shape of the structure. This stiffness should appear to increase during compression if the contact area increases appreciably due to plastic accommodation or Poisson's ratio effects.

BIBLIOGRAPHY

[1] Ian N Sneddon. The relation between load and penetration in the axisymmetric boussinesq problem for a punch of arbitrary profile. *International journal of engineering science*, 3(1):47–57, 1965.

Appendix D

ZNO NANOWIRE FABRICATION AND CHARACTERIZATION

D.1 Electrolysis-Aided Hydrothermal Growth Set-up

The templated substrate is loaded into a custom electrolysis holder (Figure D.1) using a pressure fit window to allow the growth solution access to the substrate. The holder provides electrical connection to the gold film coating on the substrate through a platinum wire. This post will act as the cathode side of reaction. On the other post, a platinum mesh acts as the counter electrode.

A constant voltage of -1.25 V was applied across the electrode using a Keithley 2182A nanovoltmeter before submersion into the growth solution. Application of a voltage has been shown to increase growth rate by a factor of 35. [1] Additionally work by Lifson *et al.* shows that changing the applied voltage has little to no effect on the final diameter size in the solution formulation used for this work [2].

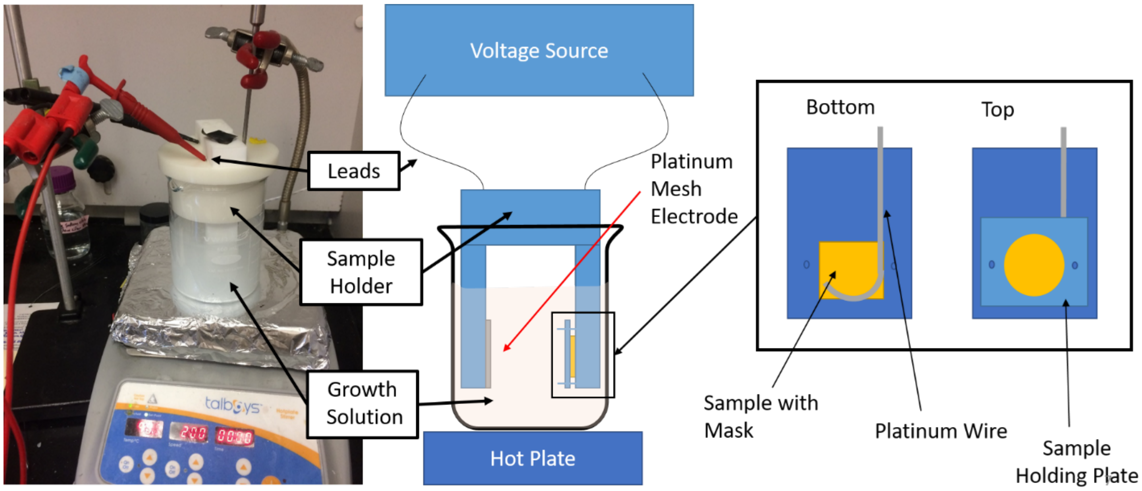

Figure D.1: **Hydrothermal Growth Apparatus.** Images and a corresponding schematic of the electrolysis cell during testing. Expanded view of the of the custom set-up for holding the chip and providing electrical contact during growth.

D.2 Nanowire Tilt Angles

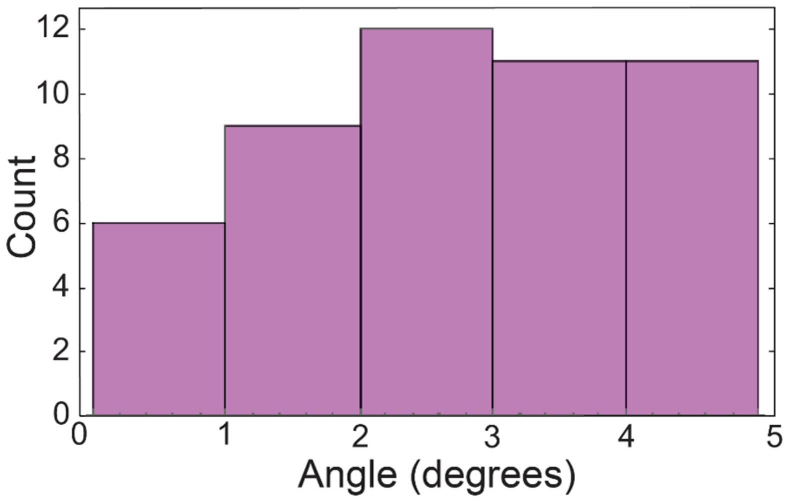

Figure D.2: **Nanowire Tilt Angles.** A histogram showing the relatively uniform distribution of tilt angles measured from as-fabricated bundle samples with a mean of 2.8 +/- 1.2°.

D.3 TEM Preparation of ZnO Nanowire Bundles

The top surface of the bundle is protected with a 100 nm thick layer of platinum (Pt) deposited via a Gas Injection System (GIS) using an electron beam in an FEI Versa DualBeam SEM followed by a 400 nm thick layer of Ga+ FIB-deposited Pt in the same chamber. Next, a Ga+ ion beam is used to carve out 5 µm x 3 µm trenches into the substrate forming a U-cut to free the silicon base from the rest of the substrate. Using a tungsten needle (EZlift program), the detached silicon base with the nanowire bundle on the top surface is transferred and glued via FIB-deposited Pt to a copper halfmoon grid with the long axis of the bundle parallel aligned with the grid post using the same GIS Pt deposition. After detaching the tungsten needle, a series of cuts are made with a decreasing Ga+ voltage/current (30 kV, 100 pA; 30 kV, 10 pA; 16 kV 23 pA) are used to progressively thin the cross-section of the bundle structure to <100 nm for TEM imaging.

BIBLIOGRAPHY

[1] J. Cui and U. J. Gibson. Enhanced nucleation, growth rate, and dopant incorporation in zno nanowires. *J. Phys. Chem. B*, 109:22074, 2005.

[2] Max L Lifson, Christopher G Levey, and Ursula J Gibson. Diameter and location control of zno nanowires using electrodeposition and sodium citrate. *Applied Physics A*, 113(1):243–247, 2013.

Appendix E

ADDITIONAL MECHANICAL ANALYSIS OF ZNO NANOWIRES

E.1 Impact of Tilt Angle and Flaw Size on Failure Stress

In evaluating the impact of angle on failure stress, we look at the relationship between flaw size at first failure, a, the stress at failure initiation, and the angle, θ, described in Equation 2.4 from Section 2.3 section through the following relationship:

$$a = \frac{K_{IC}^2 b^2 h^2}{12\,(\sigma A sin\theta)^2} - \frac{h^2}{3} \tag{E.1}$$

where b is the nanowire thickness for 300 nm, h is the interfacial thickness of 5 Å, K$_{IC}$ is the interfacial toughness of 0.58 MPa$\sqrt{m}$, and A is the area of the top surface of a 2 µm diameter bundle. If we assume the same flaw distribution in order to isolate the effect of simply the angle on failure stress, a will take on the same value in both bundles as they will both have the same largest critical flaw size for initiation of failure. Looking at a variation in of 1° in two bundles we show the maximum impact of the variation using a flaw size of 300 nm and tilt angles of 2° and 3°, Solving for stress we see that the stress of failure initiation is 1.3 GPa for the bundle with 2° tilt and 0.87 GPa for the bundle with 3° tilt. This represents an upper bound of a 0.43 GPa difference in initial failure stress.

For comparing the impact of flaw size on failure stress observed, we use the equation above but with a fixed failure stress and identify the crack length associated with a particular tilt angle. We determine that both a 217 nm defect with a tilt of 3° and a 163 nm with a tilt of 4° will initiate failure at 0.7 GPa.

E.2 Euler Buckling Calculations

Assuming a general column form with a hexagonal cross-section for the individual nanowires, the standard Euler Buckling relationship applies:

$$\sigma_{buckle} \geq \frac{\pi^2 E}{2k^2 \left(\frac{l}{r}\right)^2} \tag{E.2}$$

with l being the height, r being the radius, k being the end condition factor (i.e., friction condition), and E the elastic modulus in the direction of loading. The aspect ratio of the nanowires in this experiment lies between 26 and 27. We assume a fixed based condition due to surface bonding of the nanowires to the substrate. The interaction between the top

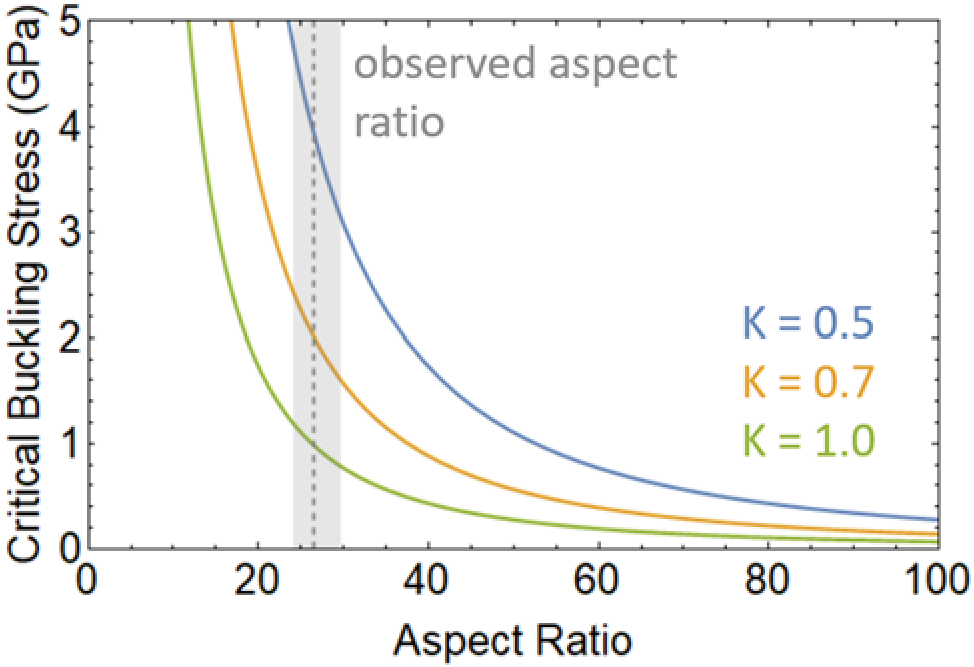

Figure E.1: **Critical Buckling Stress for an Unsupported Hexagonal ZnO Nanowire.** For a particular aspect ratio and given a fixed base and fixed (k = 0.5), pinned (k – 0.7), or free (k = 1.0) boundary condition, the critical stress required to initiate Euler buckling. Grey area reflects experimentally average +/- a standard deviation in observed dimensions of the nanowires.

surface of the nanowires and the indenter is best described by a free rotation condition (k = 0.7) based on SEM images during *in-situ* compression. Therefore, the critical Euler Buckling stress for these nanowires is 2 GPa. To highlight the range of values that could possibly be seen in our system, we include calculations for both fixed (k = 0.5) and free translation (k = 1.0) friction conditions at the indenter-nanowire interface as demonstrated in Figure E.1. The figure highlights the region of our observed nanowires as well as the aspect ratios required for buckling to occur in the range of failure initiation stresses.

Table E.1 further identifies the specific aspect ratios required for critical buckling failure to occur at the stress values associated with our onset of nanowire interfacial splitting. Values bolded indicate conditions in which buckling would likely be a dominant mechanism in our system.

In order for buckling to explain the range of values seen during localized failure with the free translation condition, some nanowires would need to be either 10.4 µm taller than average (a 260% increase) or 134 nm thinner than average (a 44% decrease). For the free

Critical Stress (GPa)	Fixed (k = 0.5)	Free Rotation (k = 0.7)	Free Translation (k = 1)
0.3	96.0	68.6	48.0
1.0	52.6	37.4	**26.5**
1.3	46.1	33.0	**23.0**

Table E.1: **Critical Aspect Ratio for Euler Buckling.** Calculated critical aspect ratio for a given a applied stress for various boundary conditions of a hexagonal column.

rotation condition, nanowires with dimensions either 16.6 µm taller than average (a 415% increase) or 183.4 nm thinner than average (a 61% decrease) would need to be present. All these values are far outside the observed range of 301 +/- 31nm and 4.00 +/- 0.15 µm.

E.3 Derivation of Probability Function for Failure

Probability that an element of the bundle can survive is $\tilde{f}$. The initiation rate of a particular failure can be described as the fractional reduction rate of intact elements within the next time interval.

$$\dot{n}_i = -\frac{1}{\tilde{f}_i}\frac{d\tilde{f}_i}{dt} \tag{E.3}$$

looking along a common strain path,

$$ln\left(\tilde{f}_i\right) = -\int \frac{\dot{n}_i}{\dot{\varepsilon}} dL \tag{E.4}$$

which is equivalent to

$$ln\left(\tilde{f}\right) = -\int \frac{\sum \dot{n}_i}{\dot{\varepsilon}} dL \tag{E.5}$$

The initiation rate can also be defined by the probability of a particular element reaching the failure strain of the material or failure mechanism

$$\dot{n}_i = \nu \; dN_i \; exp\left[-\left(\frac{\varepsilon_c}{\varepsilon}\right)^m\right] \tag{E.6}$$

with ε_c being equal to the critical failure strain as a function of ε being the current strain. m is the Weibull exponent and relates to the failure prediction of the material or mechanism. ν is the attempt frequency. Combining this definition with the above equation for $\tilde{f}$ gives

$$ln\left(\tilde{f}\right) = -\nu \int\int \frac{1}{\dot{\varepsilon}} \; \exp\left[-\left(\frac{\varepsilon_c}{\varepsilon}\right)^m\right] \; dN \; d\varepsilon \tag{E.7}$$

The probability of failure can be defined as f=1-$\tilde{f}$ and thus

$$f = 1 - exp\left[-\nu \int\int \frac{1}{\dot{\varepsilon}} \; \exp\left[-\left(\frac{\varepsilon_c}{\varepsilon}\right)^m\right] \; dN \; d\varepsilon\right] \tag{E.8}$$

Further manipulation of this equation assuming linear elasticity gives rise to a solution assuming uniform strain in compression of the structure and assuming a constant strain rate.

$$f\left(\sigma\right) = 1 - exp\left[\frac{\nu N}{\dot{\sigma}}\int_0^{\sigma} \exp\left[-\left(\frac{\sigma_c}{\sigma^{\prime}}\right)^m\right]\, d\sigma^{\prime}\right] \tag{E.9}$$

with $\dot{\sigma}$ as the stress loading rate, ν as the attempt frequency for failure, N as the total number of nanowires, σ_c as the critical failure stress, and m as the Weibull exponent. The ratio ultimately determines the "stress step size" over which failure attempts occur.

Appendix F

PIEZOELECTRICITY

In cyrstalline materials, piezoelectricity describes a material with electromechanically coupling. The direct-piezoelectric effect is defined as the coupling of mechanical stimuli to an electrical response in a material. The inverse-piezoelectric effect is defined as the coupling of an electrical stimuli to a spontaneous mechanical deformation or stress in a material. The coupling occurs when a lattice of charged atoms is distorted to accommodate the applied mechanical stimuli or when an electric field shifts the equilibrium dipole displacement for atoms in the lattice (Figure F.1). Thus, the lattice must be non-centrosymmetric (i.e., have no inversion symmetry) in order to have piezoelectricity. It is also important to highlight the asymmetry or directionality of the response with regards to the lattice orientation. For ZnO as outlined in Figure F.1 in compression, a crystal with the [0001] direction in the positive z direction will have net negative charge on the top surface. However, if the crystal was pointing with the $[000\bar{1}]$ direction aligned to the positive z, this relationship would flip and the charge would be positive.

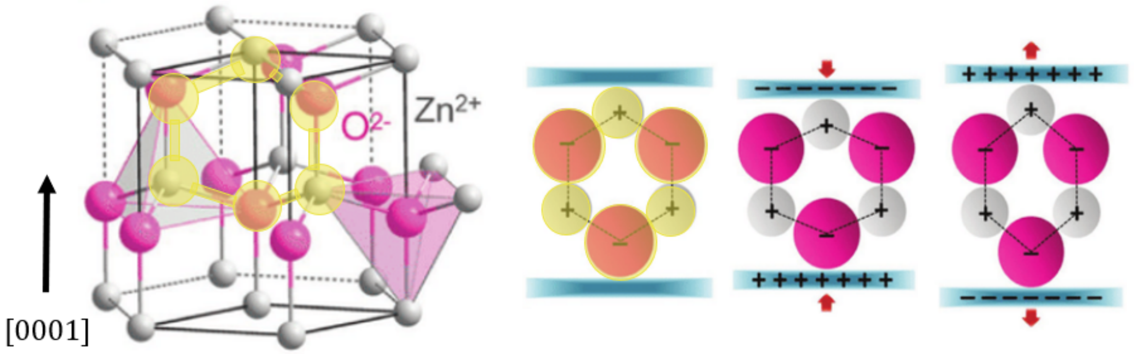

Figure F.1: **Piezoelectric Mechanism in ZnO.** Schematic figure of the wurtzite crystal structure of ZnO with the ring structure responsible for piezoelectric character highlighted. Corresponding 2D diagram shows how applied stress or electric field can result in directional electromechanical responses. Images adapted from Ref. [225] under a creative commons license.

This behavior is described through a direct-piezoelectric (or inverse-piezoelectric) tensor, where each entry is a specific piezoelectric coefficient describing the coupling between a mechanical stress in a particular direction to an electrical response in a particular direction. Below is an example equation showing the relationship of the direct-piezoelectric effect tensor to the constituent relationship for the coupling. Note that the subscripts use Voight notation.

$$\begin{pmatrix} D_1 \\ D_2 \\ D_3 \end{pmatrix} = \begin{pmatrix} d_{11} & d_{12} & d_{13} & d_{14} & d_{15} & d_{16} \\ d_{21} & d_{22} & d_{23} & d_{24} & d_{25} & d_{26} \\ d_{31} & d_{32} & d_{33} & d_{34} & d_{35} & d_{36} \end{pmatrix} \begin{pmatrix} \sigma_1 \\ \sigma_2 \\ \sigma_3 \\ \sigma_4 \\ \sigma_5 \\ \sigma_6 \end{pmatrix} + \begin{pmatrix} \varepsilon_{11} & \varepsilon_{12} & \varepsilon_{13} \\ \varepsilon_{21} & \varepsilon_{22} & \varepsilon_{23} \\ \varepsilon_{31} & \varepsilon_{32} & \varepsilon_{33} \end{pmatrix} \begin{pmatrix} E_1 \\ E_2 \\ E_3 \end{pmatrix} \tag{F.1}$$

Thermodynamically we can think of the piezoelectric coefficients as the function which describes the change in electrical response as a function of a mechanical behavior. Through Maxwell relations one can show equivalence between the direct-piezoelectric and inverse-piezoelectric relationships, thereby demonstrating interchangeability between the direct and inverse effects. Below Table F.1 outlines the four standard piezoelectric coefficients and the coupling they specifically describe for both the direct- and inverse-piezoelectric effects. In the work described in this thesis, the d$_{ij}$ and h$_{ij}$ coefficients are used.

Coefficient	Direct	Inverse
d$_{ij}$	$\left(\frac{\partial D_i}{\partial \sigma_j}\right)^E$	$\left(\frac{\partial \varepsilon_j}{\partial E_i}\right)^\sigma$
e$_{ij}$	$\left(\frac{\partial D_i}{\partial \varepsilon_j}\right)^E$	$-\left(\frac{\partial \sigma_j}{\partial E_i}\right)^\varepsilon$
g$_{ij}$	$-\left(\frac{\partial E_i}{\partial \sigma_j}\right)^D$	$\left(\frac{\partial \varepsilon_j}{\partial D_i}\right)^\sigma$
h$_{ij}$	$-\left(\frac{\partial E_i}{\partial \varepsilon_j}\right)^D$	$\left(\frac{\partial \sigma_j}{\partial D_i}\right)^\varepsilon$

Table F.1: **Definition of Piezoelectric Coefficients.**

Appendix G

NCZNO SAMPLE FABRICATION AND CHARACTERIZATION

G.1 Photopolymer Complex Synthesis — Resin Formulation

The resin used for printing samples in Chapter 3 and 4 is formed in two parts, polymer constituent solution (part A) and a photoinitiator solution (part B). Part A consists of 1 ml of a 5 g/ml aqueous solution of $Zn(NO_3)_2{\cdot}6H_2O$ and 2.67 ml of polyethylene diacrylate (PEGda) with a molecular weight of 525. Part B is composed of 6.2 mg of 7-diethylamino-3-thenoylcoumarin (DETC), the photoinitator, in 500 ml dimethyl sulfoxide (DMSO), which acts as its solvent. This forms a 12.4 mg/ml concentration of photoinitator solution. 50 ml of part B are mixed with 500 ml of part B to form the resin.

G.2 TEM Sample Preparation of nc-ZnO

The top surface of the bundle is protected with a 100 nm thick layer of platinum (Pt) deposited via a Gas Injection System (GIS) using an electron beam in an FEI Versa DualBeam SEM followed by a 400 nm thick layer of Ga+ FIB-deposited Pt in the same chamber. Next, a Ga+ ion beam is used to carve out 5 x 3 µm trenches into the substrate forming a U-cut to free the silicon base from the rest of the substrate. Using a tungsten needle (EZlift program), the detached silicon base with the nc-ZnO pillar on the top surface is transferred and glued via FIB-deposited Pt to a copper halfmoon grid with the long axis of the pillar parallel aligned with the grid post using the same GIS Pt deposition. After detaching the tungsten needle, a series of cuts are made with a decreasing Ga+ voltage/current (30 kV, 100 pA; 30 kV, 10 pA; 16 kV 23 pA) are used to progressively thin the cross-section of the bundle structure to <100 nm for TEM imaging.

G.3 Grain Size Analysis nc-ZnO

All grain size analysis was carried out in ImageJ software. The TEM dark field images were converted to binary black and white images from greyscale with the automatic thresholding from the ImageJ software program. After setting the scale bar appropriately, the particle analysis feature from ImageJ can be used to identify grains that are illuminated under the dark field condition. Note that a minimum feature size of at least 5 Åwas set as this is approximately the amorphous limit of the material.

Appendix H

DERIVATION FOR THE THEORETICAL STANDARD DEVIATION OF THE MEASURED ELECTROMECHANICAL RESPONSE OF A RANDOMLY ORIENTED MICROSTRUCTURE

We assume that the grain orientation will follow a uniform distribution as there is no external driving force influencing grain nucleation, and TEM diffraction investigations do not indicate any preferred orientation. For ZnO, the electromechanical response is described by the primary piezoelectric coefficient, h33, which indicates the generated electric field along the c-axis per unit of deformation along the c-axis. Thus all rotations of a grain about the c-axis are symmetrically equivalent.

In the proposed measurement model, we only apply mechanical stimuli and measure electromechanical behavior in the z direction. Thus, the problem can be simplified to a 2D construction as all rotations about the z direction will produce symmetric results given the piezoelectric behavior of ZnO as described above. Each grain will contribute some piezoelectric behavior between -h_{33} and h_{33}. This behavior is directly proportional to the orientation of the crystal's c-axis relative to the direction of measurement, as we can only probe the resulting z component of the piezoelectric response. As the grains are randomly oriented in a uniform distribution, the values of the piezoelectric contribution in the z direction will also follow a uniform distribution ranging from -h_{33} to h_{33}. The standard deviation of this distribution is:

$$\sigma_{sample} = \frac{b - a}{s\sqrt{3}} \tag{H.1}$$

where b is the largest value the distribution can take and a is the smallest value the distribution can take. Therefore the expected standard deviation in a given pillar's response from fluctuation in microstructure is:

$$\sigma_{sample} = \frac{h_{33} - (-h_{33})}{2\sqrt{3}} = h_{33}\sqrt{3} \tag{H.2}$$

During measurement we are sampling from a normal distribution by selecting a random sample to test. This is a valid assumption as all samples are independent (the microstructure of one does not influence the microstructure of another). Thus the standard deviation of the measured response will be:

$$\sigma_{measured} = \frac{\sigma_{P} sample}{\sqrt{2N}} = h_{33}/\sqrt{6N} \tag{H.3}$$

For extension of this model to other materials with more complex piezoelectric tensors, the effective contribution of each grain in the direction of electrical measurement as a function of the applied stress would need to be determined. Once the cumulative distribution function (CDF) for this relationship between piezoelectric contribution and grain orientation can be generated, the standard deviation can be calculated which will replace Eq. H.1. The normal distribution sampling treatment will remain the same.

Appendix I

SHEAR BAND NUCLEATION ENERGY DERIVATION

It is proposed that the formation and subsequent propagation of a shear band occurs when the stored elastic strain energy in the material is greater than the shear band nucleation energy. Stored elastic strain energy, U_{el}, can be defined as:

$$U_{el} = \frac{\sigma^2 V}{2E} \tag{I.1}$$

With E as the elastic modulus of the material, σ as the true stress, and V as the volume of material being deformed. The shear band nucleation energy, U_{shear}, can be defined as:

$$U_{shear} = \frac{\Gamma A}{cos\,(\theta)} \tag{I.2}$$

where A is the cross-sectional area of the structure relative to the loading direction and θ is the angle the shear band will form and travel along relative to the cross-sectional area. Γ is the shear band energy per unit area.

The critical stress for shear band mediated mechanical deformation, c, occurs when Eq. I.1 is equal to Eq. I.2.

$$U_{el} = U_{shear} \tag{I.3}$$

$$\frac{\sigma_c^2 V}{2E} = \frac{\Gamma A}{cos\,(\theta)} \tag{I.4}$$

As our material is a cylindrical pillar and it undergoes uniaxial compression we know the plane of highest shear will be along 45° relative to the loading direction (θ = 45°). We can further simplify the equation as our pillars are elastically loaded until the onset of shear bands and hold a 1:3 aspect ratio:

$$\frac{\sigma_c^2 3\pi r^3 L}{2E} = \sqrt{2}\Gamma\pi r^2 \tag{I.5}$$

Solving for the critical stress, the equation takes the form of:

$$\sigma_c = \sqrt{\frac{2^{1.5}E}{3r}} \tag{I.6}$$

For stresses greater than σ_c, shear band deformation is an accessible mechanism in the material. For stresses below this value, the material cannot deform via shear banding and must rely on other deformation mechanisms.

Appendix J

HYDROGEL INFUSION PROCESSING

J.1 Organogel Resin Formulation

28 mL N,N-dimethylformamide (DMF; Sigma Aldrich, >99.9%) is mixed with 35 mL poly(ethylene glycol diacrylate) Mn = 575 (PEGda; Sigma-Aldrich). Separately, 347 mg 2-dimethylamino-2-(4-methyl-benzyl)-1-(4-morpholin-4-yl-phenyl)-butan-1-one (Irgacure 379; iGM Resins), 229 mg bis[4-(dimethylamino)phenyl]methanone (Michler's ketone; Sigma-Aldrich) and 10.3 mg 1-(phenyldiazenyl)naphthalen-2-ol (Sudan I; Sigma-Aldrich) is stirred into 7mL of DMF. This solution is then added to the DMF/PEGda mixture and swirled until completely homogenous.

J.2 Solvent Exchange

Organogel structure is soaked in DMF for 1 hr on a hot plate at 70 °C. After the first DMF rinse, the DMF is decanted, and organogel is soaked again in fresh DMF for 1 hr at 70 °C. Subsequently, each organogel structure is soaked in deionized (DI) water for 1 hr at 70 °C, followed by a second soak in fresh DI water for 1 hr at 70 °C to convert the structures from organogel lattices to hydrogel lattices. It should be noted that residual DMF in the structure can lead to formation of porosity in the final structure and cause precipitation of the metal salt during the swelling process, which leads to an inhomogeneous distribution of the metal precursors.

Appendix K

ADDITIONAL INVERSE-POLE FIGURES FOR HI METALS

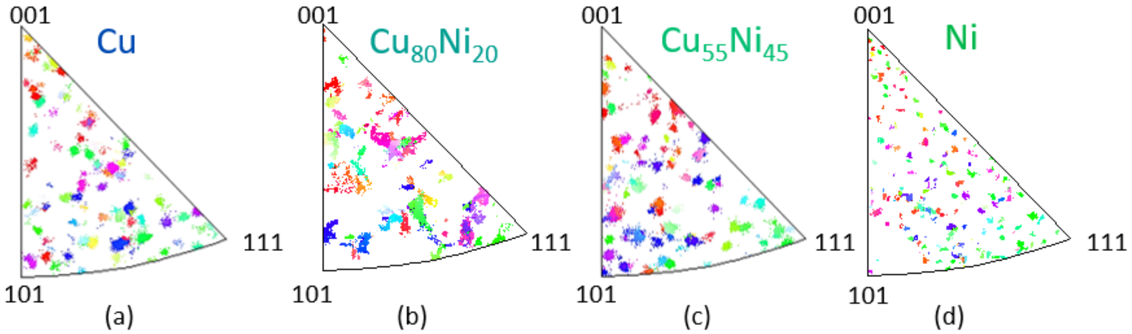

Figure K.1: **Additional Inverse Pole Figures for HI Metals.** Inverse pole figures for (a) Cu, (b) $Cu_{80}Ni_{20}$, (c) $Cu_{55}Ni_{45}$, and (d) Ni along the y axis show no texturing and even distribution of grain orientations for the in-plane direction.

Figure K.1 further supports the observation in Section 5.2 as it shows no clustering of either {100}, {110}, or {111} along any structural direction.

Appendix L

CURPONICKEL SOLID-SOLUTION HARDENING COMPARISON

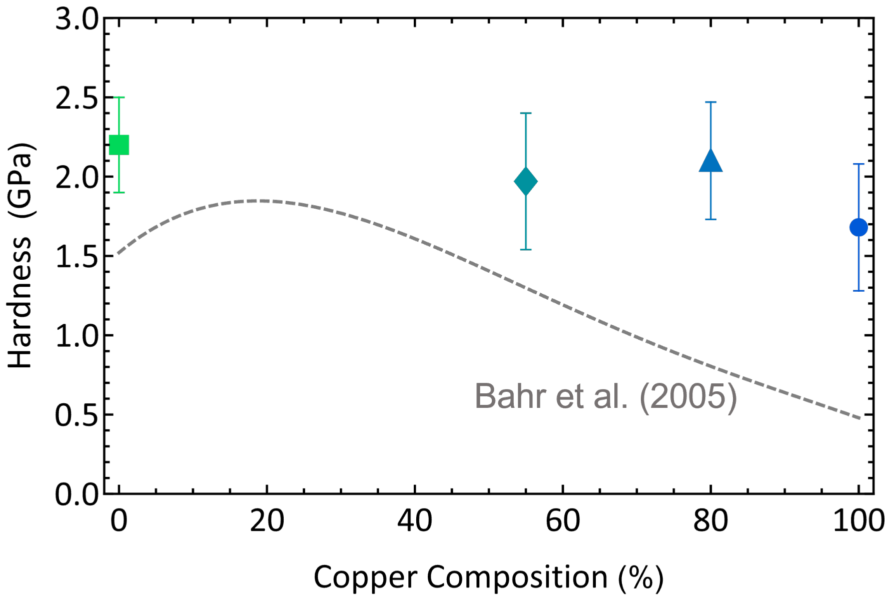

Figure L.1: **Comparing Hydrogel Infusion Cupronickel Alloys to Solid-Solution Hardening Behavior.** The average hardness of samples produced through Hydrogel Infusion for various compositions and the standard error of the hardness are plotted in color. The predicted solid-solution hardening behavior from Ref. [1] is prepresented by the dashed grey line.

As mentioned in the main text, the reference from Bahr *et al.* [1] measures hardness for alloys with a grain size of 50 µm and is therefore not a direct quantitative comparison to the measured hardness in cupronickel alloys. However as a single source of reported solid-solution hardening in cupronickel alloys, this source shows a systematic measurement of hardness by nanoindentation across various alloys compositions for a diffusion-based alloying process. This process is a fairly comparable mechanism of alloying when comparing to HI alloys and thus gives intuition around the general expected behavior for solid-solution hardening in the curponickel alloy.

It is important to note that another sources, Chang & Chang [2], shows higher hardness vales for Cu (1.1-1.3 GPa) in a similar grain size regime. These samples include bulk and electroplated Cu but do not have any insights on how these particular forms of processing may impact hardness in the cupronickel alloy system or the detailed microstructure of the reported Cu. As no other systematic alloying studies have been found by the author, Bahr & Vasquez serves as the main point of comparison for the solid-solution hardening effect. Remainder of the discussion on the observed behavior in curponickel alloys continues in Section 6.3.

BIBLIOGRAPHY

[1] DF Bahr and G Vasquez. Effect of solid solution impurities on dislocation nucleation during nanoindentation. *Journal of materials research*, 20(8):1947–1951, 2005. URL `https://doi.org/10.1557/JMR.2005.0244`.

[2] Shou-Yi Chang and Ting-Kui Chang. Grain size effect on nanomechanical properties and deformation behavior of copper under nanoindentation test. *Journal of applied physics*, 101(3):033507, 2007.

Appendix M

ELECTRON BACKSCATTER DETECTION

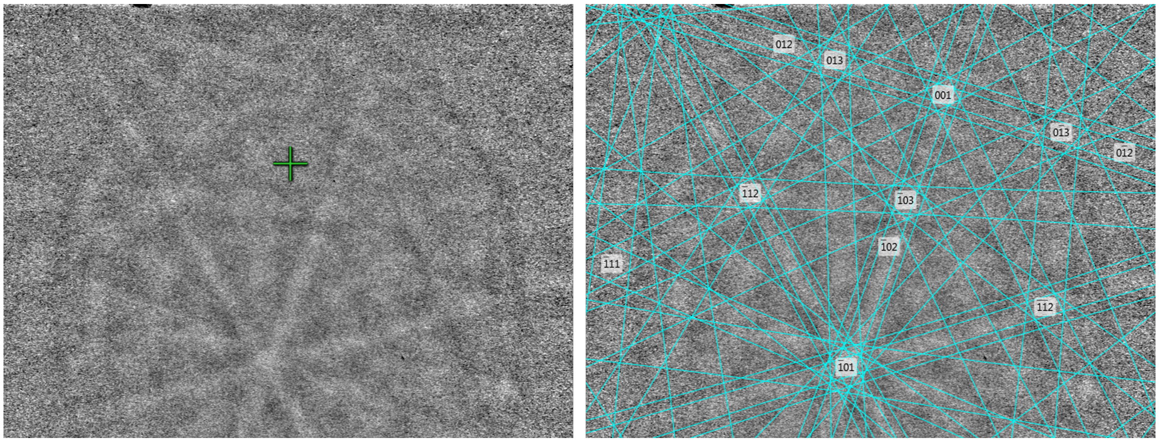

Figure M.1: **Kikuchi Band Patterns Collected through Electron Backscatter Detection.** (a) A raw image from the scatter pattern and (b) the detected lines which are used to determine crystal phase and orientation in EBSD.

Maps are colored based on the orientation taken from a Kikuchi band pattern (see Figure M.1) generated by diffuse electron scattering. These patterns are directly related to the structure and orientation of a crystal. Thus EBSD allows the mapping of highly localized orientations and phases through identification of Kikuchi band patterns at individual points and outputting a map from those results. Orientation maps follow a standard coloring scheme (Figure M.2) where the points of high symmetry follow a red-green-blue scheme and other orientations are the RGB coloring associated with relative "mixing" or pathlength to those points of symmetry. For example, cyan blue is a <121> direction as it is perfectly along the edge between <111> and <101>.

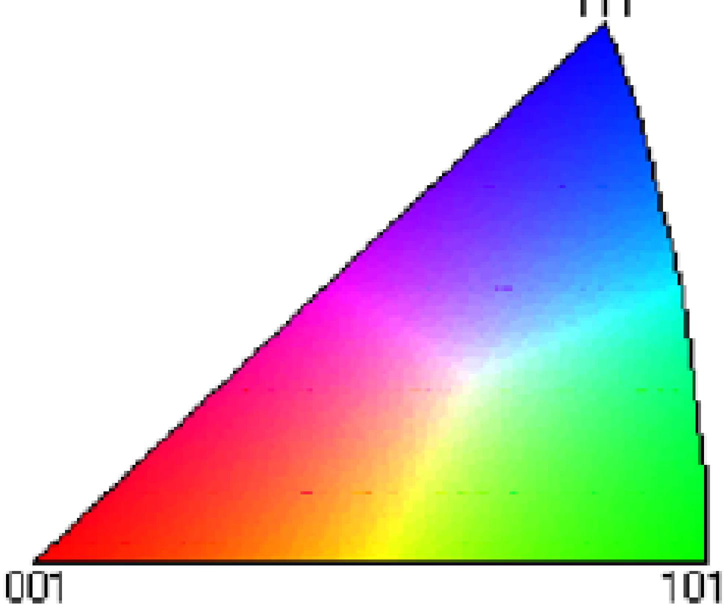

Figure M.2: **Inverse Pole Coloration Key.** The above image is the standard key for coloring orientations of crystals with red as <001>, green as <101> and blue as <111> and gradation of color mixing to represent angles in between.